MEASUREMENT OF REACTOR ANTINEUTRINO OSCILLATION WITH SNO+

Anthony Zummo

A DISSERTATION

in

Physics and Astronomy

Presented to the Faculties of the University of Pennsylvania

in

Partial Fulfillment of the Requirements for the

Degree of Doctor of Philosophy

2024

Supervisor of Dissertation

Joshua Klein, Professor of Physics and Astronomy

Graduate Group Chairperson

Christopher Mauger, Associate Professor of Physics and Astronomy

Dissertation Committee

Joseph Kroll, Professor of Physics and Astronomy
Adam Lidz, Associate Professor of Physics and Astronomy
Marija Drndic, Professor of Physics and Astronomy

To my family.

ACKNOWLEDGEMENT

My work as a graduate student was only possible with the support of many people who have helped me improve as a student, researcher, and person. First, I would like to thank my advisor, Josh Klein, who has been an exceptional source of guidance and whose persistence and creativity in problem solving have been an inspiration to me as a scientist. Josh has given me the freedom to work on the tasks I found most worthwhile, and has created an excellent work environment and research group where collaboration between members makes everyone better.

I would like to thank the many postdocs and graduate students in the Penn neutrino group who have helped me throughout my graduate career, including Nuno Barros, Tereza Kroupová, Amanda Bacon, and Sam Naugle. In particular, I am thankful for Tanner Kaptanoglu and Eric Marzec who taught me basically everything I know about the SNO+ electronics, and Logan Lebanowski who has provided advice on a range of topics including the reactor antineutrino analysis. I would especially like to thank my fellow graduate students David Last and Meng Luo. Our late night homework sessions, board game nights, and many games of pool after group meetings (before the table was tragically removed from the grad student lounge) were essential to my survival through grad school. I am extremely grateful to have been able to learn from such an amazing group of people with such a broad range of expertise, often without having to leave the comfort of my own desk. I will always remember the discussions, long drives to Sudbury, and burritos from MexiCali we have had together.

The SNO+ experiment has allowed me to work on a range of interesting projects with feedback from many excellent collaborators from across the world. I would like to thank Matt Depatie and Mark Ward for their guidance during my trips to SNOLAB for electronics work and for keeping the detector running during the pandemic when travel to Sudbury wasn't possible. I would also like to thank Valentina Lozza whose expertise in backgrounds and impressive knowledge of all things SNO+ was an immense resource for nearly everything I worked on.

Finally, none of this would be possible without my family who has always supported me in everything I have done. My parents, Chris and Steve, and brothers, Tommy and Angelo, have always believed in me and set me up for success in life and I will never be able to thank them enough. Last, I would like to thank Kim, who has made every moment better and whose love and support have gotten me through the most challenging times.

ABSTRACT

MEASUREMENT OF REACTOR ANTINEUTRINO OSCILLATION WITH SNO+

Anthony Zummo

Joshua Klein

This thesis presents a few topics all related to the SNO+ experiment: improvements to the trigger system, measurements of backgrounds to a potential neutrinoless double beta decay ($0\nu\beta\beta$) signal, and a measurement of neutrino oscillation parameters using reactor antineutrinos.

Two background analyses performed during the water and partial scintillator phases of SNO+ are presented. The first analysis measures the radioactive backgrounds from the external components of the detector in the SNO+ water phase. The second analysis investigates all backgrounds to a potential neutrinoless double beta decay signal in the SNO+ partial scintillator fill phase. Both analyses find backgrounds consistent with expectation. These background analyses also motivated improvements to the SNO+ trigger system. This includes additional trigger functionality and improvements minimizing the deadtime in the SNO+ trigger system.

Finally, an analysis of reactor antineutrinos detected in 134.4 days of SNO+ data is presented. A fit of reactor antineutrino event candidates provides a measurement of $\Delta m^2_{21} = 7.96^{+0.48}_{-0.41} \times 10^{-5}$ eV^2 with local minima above and below the best fit value at $< 2\sigma$ significance. Combining this result with the existing global constraint from KamLAND gives a new value of $\Delta m^2_{21} = 7.59^{+0.18}_{-0.17} \times 10^{-5}$ eV^2, slightly higher than the previous best fit. In addition, the flux of geoneutrinos is measured to be 64 ± 44 TNU, consistent with expectation. The future sensitivities of these measurements with additional data are also presented. It is concluded that SNO+ expects to reach the current sensitivity in its measurement of Δm^2_{21} with ~4-5 years of livetime.

TABLE OF CONTENTS

LIST OF TABLES

LIST OF ILLUSTRATIONS

Chapter 1

INTRODUCTION

This thesis presents a few topics all related to the SNO+ experiment: improvements to the trigger system, measurements of backgrounds to a potential neutrinoless double beta decay signal, and a measurement of neutrino oscillation parameters using reactor antineutrinos.

Chapter 2 begins with a brief history of the neutrino, focused on the aspects most relevant to this thesis, and a brief description of the neutrino's place in the Standard Model of particle physics. The physics of neutrino oscillation and massive neutrinos are then presented with additional comments on neutrinoless double beta decay ($0\nu\beta\beta$), the primary focus of SNO+. The existing methods used to measure the parameters describing neutrino oscillation are then described with a focus on those most relevant to the SNO+ measurement using reactor antineutrinos. The slight tension between measurements of Δm^2_{21} using solar neutrinos and reactor antineutrinos is then highlighted as the SNO+ experiment is capable of making an additional measurement of this parameter.

Chapter 3 then gives a detailed description of the SNO+ experiment. A special focus is given to the trigger system, which determines when to save the data, and several improvements made to this system. A description of new auxiliary triggers is given showing improvements in the ability to trigger on specific event signatures relevant to SNO+. In addition, a detailed study of the time between events in which data is lost is presented with improvements minimizing this time.

The simulation and analysis tools of SNO+ are then discussed in Chapter 4. This includes a description of the `RAT` software package and the reconstruction methods used to infer the properties of events in the detector. The many steps taken to calibrate the SNO+ detector are then detailed, including an energy calibration performed using intrinsic radioactivity. This calibration was also used to estimate the systematic uncertainties most relevant to the following analysis of reactor antineutrinos.

Chapter 5 then describes the SNO+ $0\nu\beta\beta$ background model, along with two analyses performed measuring these backgrounds in SNO+ prior to deployment of the $0\nu\beta\beta$ isotope. The first of these analyses uses data taken during the SNO+ water phase to measure the radioactive backgrounds from the external components of the detector. The second of these analyses uses data taken during the SNO+ partial scintillator fill phase to investigate all potential backgrounds to a potential $0\nu\beta\beta$ signal. A comparison of both results to the nominal predicted background rates used in SNO+ sensitivity projections is presented.

Finally, Chapters 6-9 present an analysis of reactor antineutrinos detected in 134.4 days of SNO+ data. These chapters include a detailed description of all the factors that determine the rate of reactor antineutrino interactions in the SNO+ detector as well as the expected rate of background events that can mimic the antineutrino signal. A likelihood based method used to select these events and its efficiency is then described. An extended maximum likelihood fit is then applied to determine the best fit values for the neutrino oscillation parameters Δm^2_{21} and θ_{12}. This result is compared to the existing measurements of these oscillation parameters and additional results with constraints from these existing measurements are also presented. In addition, comments are given on the flux of geoneutrinos, which is treated as a nuisance parameter in the fit, but is also an interesting signal. This thesis concludes by giving potential improvements for this analysis and sensitivity estimates for the oscillation parameters and geoneutrino flux as a function of livetime as the SNO+ experiment continues to take more data.

Chapter 2

NEUTRINO PHYSICS

2.1 Neutrino History

The neutrino was originally hypothesized in 1930 by Pauli to explain the measured energy spectrum of electrons emitted in β decay [1]. These measurements found that the electrons were emitted with a continuous energy spectrum. Pauli proposed a neutral, weakly interacting particle that was not detected in order to maintain conservation of energy in the decay. When Fermi produced a more detailed theory of β decay a few years later [2], he proposed that the particles were created during the decay: $n \rightarrow p + e^- + \nu$, proposing a 4 point interaction vertex whose strength was characterized by what we now call the Fermi constant G_F. He named the new particle produced in this decay the "neutrino".

The inverse beta decay process: $\nu + p \rightarrow n + e^+$ was proposed by Bethe and Peierls in 1934 [3]. At the time, the predicted cross-section was far too small to allow detection of the neutrino. However, with the development of nuclear reactors, which produce an enormous flux of neutrinos, and liquid scintillator, which allowed the creation of large detector volumes, the neutrino was first detected in 1956 by Cowan and Reines [4]. Their experiment used a Cd doped water target placed between two liquid scintillator detectors just outside of a nuclear reactor core to detect the coincidence of the produced positron and the γ emitted in the capture of the produced neutron. In principle, this method is not so different from those used by several modern neutrino experiments, including SNO+. The existence of the two additional flavors of neutrinos (ν_μ and ν_τ) would later be first demonstrated by Lederman, Schwartz, and Steinberger [5] in 1962 and by the DONUT experiment [6] in 2000 respectively.

The first proposal of neutrino oscillation was made in 1957. Motivated by the discovery of oscillation in Kaons ($K^0 \leftrightarrow \bar{K}^0$), Pontecorvo proposed similar oscillation between neutrinos and antineutrinos [7] before it was known that there were multiple flavors of neutrino. His work was later developed into a more detailed theory of neutrino flavor oscillation by Maki, Nakagawa, and Sakawa [8]. The first evidence for this oscillation was produced when measurements of solar neutrinos in the 1960s made by the Homestake experiment [9] showed fewer detected neutrinos than expected by the solar models created by Bahcall [10] [11].

It was not until ~2000 that the SNO [12] and Super-Kamiokande [13] experiments definitively solved the solar neutrino problem and observed neutrino oscillation. The use of heavy water allowed SNO to detect all three neutrino types from the Sun, demonstrating that the total neutrino flux was consistent with expectation and that ν_e had oscillated to the previously undetectable flavors ν_μ and ν_τ. Super-K used atmospheric neutrinos to demonstrate that the observed flux of ν_μ was dependent on their energy and distance traveled to reach the detector due to oscillation. These experiments firmly established neutrino oscillation as a reality and began an era of measurements of the parameters describing this phenomenon.

In addition, in 1937 Majorana proposed a modification to Fermi's theory in which the neutrino and antineutrino are equivalent [14]. A few years later, it was proposed that under these conditions, the known rare double beta decay ($2\nu\beta\beta$) could occur without the emission of two neutrinos [15]. At the time, it was believed that this neutrinoless double beta decay ($0\nu\beta\beta$) could actually be much more common than $2\nu\beta\beta$. In fact, in 1949, experimental evidence potentially supporting this claim was produced [16]. With additional knowledge of the neutrino's coupling to the W boson, it is now known that if neutrinos are Majorana, $0\nu\beta\beta$ is expected to be much more rare than $2\nu\beta\beta$.

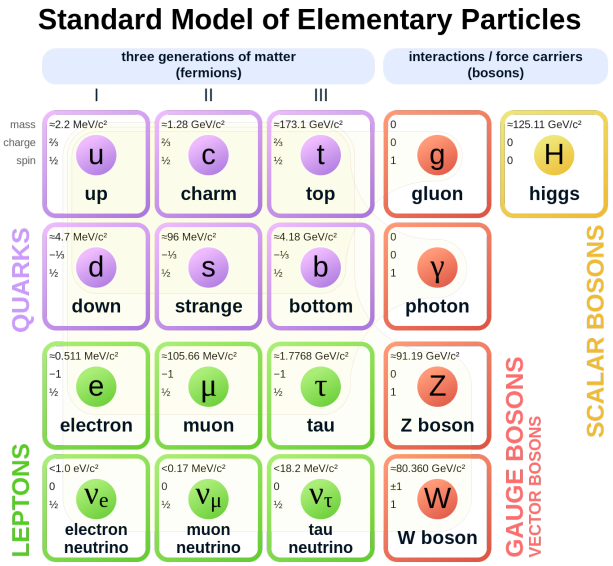

Figure 2.1: Diagram of the fundamental particles in the Standard Model [17].

Furthermore, no experiment has replicated the short double beta decay half-life claimed in 1949.

More than 80 years after Majorana's original proposal, the question of whether the neutrino is its own antiparticle has still not been answered. In addition, the most promising method of proving this fact is still through the detection of $0\nu\beta\beta$. A large number of experiments, including the focus of this thesis, SNO+, are using a variety of detector technologies and isotopes to search for this rare decay.

2.2 Neutrinos in the Standard Model

The Standard Model of particle physics was developed in the 1960s and 70s to classify all known subatomic particles and describe their interactions. It unites three of the four known fundamental forces of nature: electromagnetism, the strong force, and the weak force. In addition, it succeeds in categorizing the known fundamental particles according to the spin statistics that they obey and the forces by which they interact. A diagram of all the fundamental particles described by the Standard Model is shown in Figure 2.1. An enormous number of measurements have been performed testing the accuracy of the Standard Model, nearly all of which have been found to agree with its predictions to high precision. However, there are still a few observations that cannot be explained by the Standard Model.

In the Standard Model, neutrinos are uncharged leptons with three different flavor states $(\nu_e, \nu_\mu, \nu_\tau)$ which only interact via the weak force and gravity. As a result, neutrino cross-sections are small and their interactions are rare. This makes the detection and study of neutrinos difficult, leaving many open questions about their properties. For example, neutrinos produced as one flavor can later be detected as another flavor. This phenomenon is referred to as neutrino oscillation and implies that neutrinos have mass, a feature not included in the Standard Model. This mass has been determined to be too small to measure by current experiments and the ordering of the three neutrino masses is still unknown. In addition, the mechanism by which neutrinos obtain their mass is also still unknown. The following sections discuss these properties of the neutrino in more detail.

2.3 Neutrino Oscillation

2.3.1 Oscillation in Vacuum

Neutrinos are produced in interactions as one of three flavor eigenstates $|\nu_{e,\mu,\tau}\rangle$, however, they propagate according to their three mass eigenstates $|\nu_{1,2,3}\rangle$. The relationship between these eigenstates can be described by:

$$|\nu_\alpha\rangle = \sum_{i=1}^{3} U^*_{\alpha i} |\nu_i\rangle \,, \quad \alpha = e, \mu, \tau \tag{2.1}$$

where $U_{\alpha,i}$ are the elements of a 3×3 unitary matrix referred to as the Pontecorvo-Maki-Nakagawa-Sakata (PMNS) matrix. The PMNS matrix is typically parameterized by three mixing angles θ_{12}, θ_{13}, and θ_{23} as well as a CP violating phase δ_{CP} as follows:

$$U = \begin{pmatrix} c_{12}c_{13} & s_{12}c_{13} & s_{13}e^{-i\delta_{CP}} \\ -s_{12}c_{23} - c_{12}s_{23}s_{13}e^{i\delta_{CP}} & c_{12}c_{23} - s_{12}s_{23}s_{13}e^{i\delta_{CP}} & s_{23}c_{13} \\ s_{12}s_{23} - c_{12}c_{23}s_{13}e^{i\delta_{CP}} & -c_{12}s_{23} - s_{12}c_{23}s_{13}e^{i\delta_{CP}} & c_{23}c_{13} \end{pmatrix} \tag{2.2}$$

where $c_{ij} = \cos\theta_{ij}$ and $s_{ij} = \sin\theta_{ij}$. It can be seen that if U was diagonal (i.e. $\theta_{12} = \theta_{13} = \theta_{23} = 0$), the flavor eigenstates would map directly to the mass eigenstates. The PMNS matrix can also be decomposed into three components involving only one mixing angle θ_{ij} each:

$$U = \begin{pmatrix} 1 & 0 & 0 \\ 0 & c_{23} & s_{23} \\ 0 & -s_{23} & c_{23} \end{pmatrix} \begin{pmatrix} c_{13} & 0 & s_{13}e^{-i\delta_{CP}} \\ 0 & 1 & 0 \\ -s_{13}e^{-i\delta_{CP}} & 0 & c_{13} \end{pmatrix} \begin{pmatrix} c_{12} & s_{12} & 0 \\ -s_{12} & c_{12} & 0 \\ 0 & 0 & 1 \end{pmatrix} \tag{2.3}$$

Propagation of a neutrino is then governed by the Schrödinger equation:

$$i\frac{d}{dt}\left|\nu_i(t)\right\rangle = \mathcal{H}\left|\nu_i(t)\right\rangle \tag{2.4}$$

which can be solved to obtain:

$$\left|\nu_i(t)\right\rangle = e^{-iE_x t}\left|\nu_i\right\rangle \tag{2.5}$$

A neutrino created as a flavor eigenstate can then be decomposed into the mass eigenstates and then its propagation is given by:

$$\left|\nu_\alpha(t)\right\rangle = \sum_i U^*_{\alpha i} U_{\beta j} e^{-iE_i t} \tag{2.6}$$

This neutrino which was produced in flavor eigenstate α can later interact as flavor eigenstate β with a probability given by:

$$P_{\nu_\alpha \to \nu_\beta}(t) = \left|\left\langle \nu_\beta | \nu_\alpha(t)\right\rangle\right|^2 = \sum_{i,j} U^*_{\alpha i} U_{\beta i} U_{\alpha j} U^*_{\beta j} e^{-i(E_i - E_j)t} \tag{2.7}$$

This probability being non-zero for $\alpha \neq \beta$ is referred to as neutrino oscillation. Equation 2.1 showed that if U was diagonal, the flavor and mass eigenstates would map to each other directly. Equation 2.7 then shows that under these circumstances $U^*_{\alpha i} U_{\beta i} U_{\alpha j} U^*_{\beta j} = 0,$ unless $\alpha = \beta = i = j$. Thus, $P_{\nu_\alpha \to \nu_\beta}(t) = 0$ for $\alpha \neq \beta$. It is therefore a necessity that the flavor and mass eigenstates differ for neutrino oscillation to occur. Now, a few approximations can be made assuming that the momentum of each mass state is nearly the same, the rest mass of the neutrino is small, and the momentum of the neutrino is nearly equal to its energy. The differences in energy can then be approximated as:

$$E_i - E_j = \sqrt{p_i^2 + m_i^2} - \sqrt{p_j^2 + m_j^2} \approx \frac{\Delta m_{ij}^2}{2E} \tag{2.8}$$

where the mass-squared differences are defined as $\Delta m_{ij}^2 = m_i^2 - m_j^2$. In addition, the neutrino can be approximated to be traveling at the speed of light allowing time to be converted to distance. This gives the probability:

$$P_{\nu_\alpha \to \nu_\beta}(L, E) = \sum_{i,j} U_{\alpha i}^* U_{\beta i} U_{\alpha j} U_{\beta j}^* \exp\left(- i \frac{\Delta m_{ij}^2 L}{2E} \right) \tag{2.9}$$

It can now be seen that the magnitude of the transition probability depends entirely on the elements of U, while the phase depends on the mass-squared differences, Δm_{ij}^2, the distance traveled by the neutrino, L, and the energy of the neutrino, E. Separating the real and imaginary parts of Equation 2.9 gives:

$$P_{\nu_\alpha \to \nu_\beta}(L, E) = \delta_{\alpha,\beta} - 4 \sum_{i<j} \mathrm{Re}[U_{\alpha i} U_{\beta i}^* U_{\alpha j}^* U_{\beta j}] \sin^2\left(\frac{\Delta m_{ij}^2 L}{4E} \right) \tag{2.10}$$

$$+ 2 \sum_{i<j} \mathrm{Im}[U_{\alpha i} U_{\beta i}^* U_{\alpha j}^* U_{\beta j}] \sin\left(\frac{\Delta m_{ij}^2 L}{2E} \right) \tag{2.11}$$

For massless neutrinos, $\Delta m_{ij}^2 = 0$ and the sin terms in Equation 2.10 are zero. Thus, oscillation requires massive neutrinos. Another notable fact is that the oscillation probability depends only on the squared differences of the neutrino masses. As a result, despite requiring massive neutrinos, oscillation can not be used to determine the absolute neutrino masses.

For antineutrinos, the same derivation can be performed but with the relationship between the flavor and mass eigenstates defined by the complex conjugate of U. Equation 2.2 shows that the only way to obtain a non-zero imaginary component for any $U_{\alpha i}$ is through a non-zero value for δ_{CP}. The difference between U and U^*, and therefore the difference between neutrino and antineutrino oscillation (in vacuum), is thus determined by δ_{CP}.

The two-neutrino case is shown here as an example to allow comparison to the more complicated result accounting for matter effects. The mixing matrix in this case is given by:

$$U = \begin{pmatrix} \cos(\theta) & \sin(\theta) \\ -\sin(\theta) & \cos(\theta) \end{pmatrix} \tag{2.12}$$

and the oscillation probability is given by:

$$P_{\nu_e \rightarrow \nu_\mu}(L, E) = \sin^2(2\theta) \sin^2\left(\frac{\Delta m^2 L}{2E}\right) \tag{2.13}$$

2.3.2 Oscillation in Matter

Neutrinos propagating through matter undergo neutral and charged current interactions with electrons, protons, and neutrons as they travel. The neutral current interactions affect all three neutrino flavors equally and thus do not contribute to oscillation. The charged current interactions, however, only occur between ν_e and electrons. This produces an asymmetry in how the different flavors interact, affecting the oscillation probability.

The effective potential from the charged current interactions of ν_e is given by:

$$V_{CC} = \pm\sqrt{2} G_F n_e \tag{2.14}$$

where G_F is the Fermi constant and n_e is the number density of electrons in the medium. The value is positive for neutrinos and negative for antineutrinos. Inclusion of this term in the Hamiltonian gives:

$$\mathcal{H} = \frac{1}{2E}(UM^2U^\dagger + A) \tag{2.15}$$

where

$$M = \begin{pmatrix} 0 & 0 & 0 \\ 0 & \Delta m^2_{21} & 0 \\ 0 & 0 & \Delta m^2_{31} \end{pmatrix} \quad \text{and} \quad A = \begin{pmatrix} A_{CC} & 0 & 0 \\ 0 & 0 & 0 \\ 0 & 0 & 0 \end{pmatrix} \tag{2.16}$$

with $A_{CC} = 2EV_{CC}$. For simplicity, the case of an electron neutrino in two neutrino oscillation is considered to demonstrate important features of matter oscillation. In this scenario, the propagation of the neutrino is governed by the equation:

$$i\frac{d}{dt}\begin{pmatrix}\psi_{ee}\\ \psi_{e\mu}\end{pmatrix} = \frac{1}{4E}\begin{pmatrix}-\Delta m^2_{21}\cos(2\theta_{12}) + A_{CC} & \Delta m^2_{21}\sin(2\theta)\\ \Delta m^2_{21}\sin(2\theta) & \Delta m^2_{21}\cos(2\theta_{12}) - A_{CC}\end{pmatrix}\begin{pmatrix}\psi_{ee}\\ \psi_{e\mu}\end{pmatrix} \tag{2.17}$$

The Hamiltonian can then be diagonalized to obtain:

$$\mathcal{H} = \frac{1}{4E}\begin{pmatrix}-\Delta m^2_{\text{eff}} & 0\\ 0 & \Delta m^2_{\text{eff}}\end{pmatrix} \tag{2.18}$$

where $\Delta m^2_{\text{eff}} = \sqrt{(\Delta m^2\cos(2\theta) - A_{CC})^2 + (\Delta m^2\sin(2\theta))^2}$ is the effective squared mass difference. The unitary mixing matrix can then be written as:

$$U = \begin{pmatrix}\cos(\theta_{\text{eff}}) & \sin(\theta_{\text{eff}})\\ -\sin(\theta_{\text{eff}}) & \cos(\theta_{\text{eff}})\end{pmatrix} \tag{2.19}$$

where

$$\sin^2(2\theta_{\text{eff}}) = \frac{\sin^2(2\theta)}{(\cos 2\theta_{12} - A_{CC}/\Delta m^2)^2 + \sin^2(2\theta)} \tag{2.20}$$

The oscillation probability is then given by:

$$P_{\nu_e\to\nu_\mu}(L,E) = \sin^2(2\theta_{\text{eff}})\sin^2\left(\frac{\Delta m^2_{\text{eff}}L}{2E}\right) \tag{2.21}$$

This is the same as the two neutrino case in vacuum (Equation 2.13) but with the effective mixing angle and mass squared differences rather than the vacuum values. An analogous calculation can be performed for three neutrino oscillation resulting in a similar substitution of effective mixing angles and squared mass differences (e.g. as shown in [18]).

Another notable feature is that $\sin^2(2\theta_{\text{eff}}) = 1$ when $\cos 2\theta_{12} - A_{CC}/\Delta m^2 = 0$. Thus, maximal oscillation can occur even when the expected oscillation in vacuum (determined by $\sin^2(2\theta)$) is

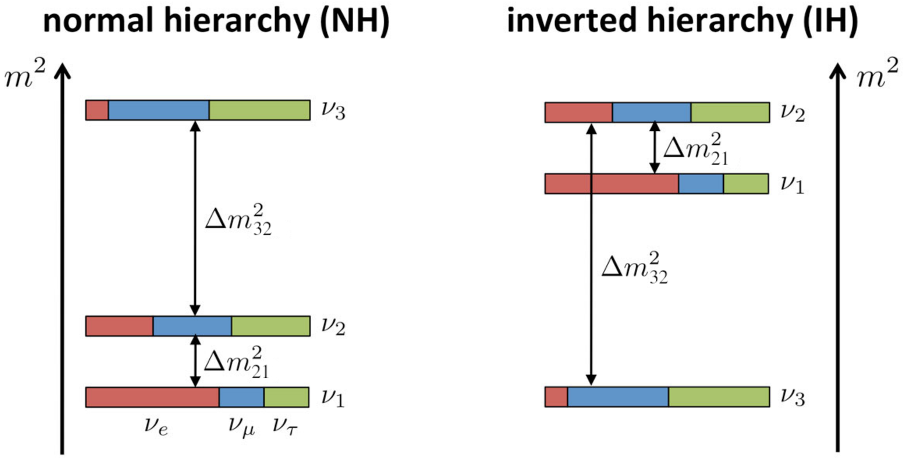

Figure 2.2: Diagrams of the normal and inverted hierarchies. The colors show the relationships between the flavor eigenstates and the mass eigenstates. Adapted from [19].

small. For, neutrinos this occurs at a specific electron density or neutrino energy:

$$n_e = \frac{\Delta m^2 \cos 2\theta}{2\sqrt{2}EG_F}, \text{ or } E = \frac{\Delta m^2 \cos 2\theta}{2\sqrt{2}n_e G_F} \tag{2.22}$$

This maximal mixing is referred to as the Mikheyev-Smirnov-Wolfenstein (MSW) effect and is particularly relevant for solar neutrinos.

2.4 Neutrino Mass

2.4.1 Neutrino Mass Hierarchy

In Section 2.3, it was shown that neutrino oscillation in vacuum depends only on the magnitude of the squared mass differences of the neutrino mass states, not the sign. Matter effects within the Sun have allowed solar neutrino experiments to determine that Δm^2_{21} is positive. The value of Δm^2_{32} has been measured to be significantly larger than Δm^2_{21}, however, the sign of Δm^2_{32} has not yet been determined. This means two possible mass orderings are allowed: $m_1 < m_2 << m_3$ or $m_3 << m_1 < m_2$. These "mass hierarchies" are referred to as the "Normal Hierarchy" and the "Inverted Hierarchy" and are depicted in Figure 2.2.

2.4.2 Neutrino Absolute Mass

In Section 2.3, it was also shown that neutrino oscillation depends only on the squared mass differences of the neutrino mass states and not the absolute masses. As a result, oscillation experiments give little information about the absolute masses of the neutrino mass states. Only lower limits can be set by assuming that the lightest state is massless.

The absolute neutrino masses have not yet been measured by any experiment. Several experiments currently attempt to measure the neutrino mass through precise measurements of the β decay energy spectrum. The KATRIN experiment currently holds the world leading upper limit on the neutrino mass for direct measurements at: $m_\nu < 0.8$ eV (90% CL) [20]. In addition, indirect constraints on the sum of the neutrino masses come from cosmological measurements. Several measurements place limits of $\sum_i m_i < \sim 0.1$ eV [21] [22] [23] but depend on cosmological models.

2.4.3 Neutrino Mass Mechanism

Neutrinos in the Standard Model are massless and thus have no prescribed way to include their mass. The most straightforward way to do this is to use the same method as all other fermions in the Standard Model, the Higgs mechanism. This is done by including a Dirac mass term in the Lagrangian:

$$\mathcal{L} = -m_D(\bar{\psi}_L \psi_R + \bar{\psi}_R \psi_L) \tag{2.23}$$

where ψ_R and ψ_L represent the left and right chiral states of the neutrino. The mass of the neutrino would then be given by:

$$m_D = \frac{y_i^\nu V}{\sqrt{2}} \tag{2.24}$$

where V is the Higgs vacuum expectation value and y_i^ν are the Yukawa couplings of the neutrino to the Higgs field. This method of generating the neutrino mass is valid but unsatisfying for two reasons.

First, Equation 2.23 implies that both neutrinos and antineutrinos have both left and right chiral states. However, only left-handed neutrinos and right-handed antineutrinos couple to the weak force and have been detected. This method would therefore require the existence of two additional "sterile" neutrinos which would only interact via gravity. These sterile neutrinos would likely be at a similar mass scale as the neutrinos and could affect oscillation probabilities. However, no definitive observations of these sterile neutrinos have yet been made.

Second, current limits on the neutrino mass are much smaller than the next lightest fermion. As a result, the Yukawa couplings for the neutrinos would have to be at least 5 orders of magnitude smaller than for other particles. The lack of a physical explanation for the large discrepancy in size makes this mass mechanism less appealing.

Because neutrinos are neutral, a different mechanism can be used to generate their masses. This results from Majorana's proposal that the neutrino could be its own antiparticle which would imply that $\psi^C = \psi$. Its mass term in the Lagrangian would then be:

$$\mathcal{L} = -m_L(\bar{\psi}_L^C \psi_L + \bar{\psi}_L \psi_L^C) \tag{2.25}$$

A Majorana mass term conveniently solves both of the previous unsatisfying aspects of the Dirac mass term. The existence of a Majorana mass term does not preclude a Dirac term and including both in the Lagrangian gives the mass terms:

$$\mathcal{L} = -m_L(\bar{\psi}_L^C \psi_L + \bar{\psi}_L \psi_L^C) - m_R(\bar{\psi}_R^C \psi_R + \bar{\psi}_R \psi_R^C) - m_D(\bar{\psi}_L \psi_R + \bar{\psi}_R \psi_L) \tag{2.26}$$

The mass eigenvalues can then be found. An interesting case where $m_L = 0$ and $m_R >> m_D$ is referred to as the see-saw mechanism. In this case the mass eigenvalues become:

$$m_{\text{light}} \approx \frac{m_D^2}{m_R}, \qquad m_{\text{heavy}} \approx m_R \tag{2.27}$$

Several different versions of this mechanism exist but the basic idea is the same. There exists a heavy right-handed neutrino with a mass at the scale of new physics not currently accessible by existing experiments and the mass of the light left-handed neutrino is driven to a low value despite having a similar Yukawa coupling as the other fermions. Thus, both the small neutrino masses and the lack of evidence for sterile neutrinos are explained naturally.

There are two additional notable consequences of Majorana neutrinos. First, as neutrinos have lepton number of 1 and antineutrinos have lepton number of -1, a Majorana neutrino where the two are one and the same would inherently violate lepton number conservation. Also, an additional term would be added to the PMNS matrix with two new Majorana phases. There are several equivalent ways of parameterizing this matrix including:

$$P_M = \begin{pmatrix} e^{i\alpha_1} & 0 & 0 \\ 0 & e^{i\alpha_2} & 0 \\ 0 & 0 & 1 \end{pmatrix} \tag{2.28}$$

which would be multiplied on the right side of the PMNS matrix in Equations 2.2 and 2.3. This term would not affect the observed oscillation probabilities and would only enter in lepton number violating processes. Searching for these lepton number violating processes is then a test of the Majorana nature of neutrinos.

Neutrinoless Double Beta Decay

The most sensitive experimental method to determine if neutrinos are Majorana is through searching for a lepton number violating decay: neutrinoless double beta decay ($0\nu\beta\beta$). Beta decay is energetically forbidden (or strongly suppressed) for certain isotopes. However, in some of these isotopes, a double beta decay ($(Z, A) \rightarrow (Z+2, A) + 2e^- + 2\bar{\nu}_e$) may still be allowed. In double beta decay, two neutrons simultaneously undergo beta decay resulting in the production of two protons, two electrons, and two antineutrinos. The total kinetic energy released in the decay is referred to as the "Q value". This decay requires two weak interactions as can be seen in its Feynman diagram shown in Figure 2.3. As a result, it has an extremely long half-life $\sim\mathcal{O}(10^{21})$ years which can vary by a few orders of magnitude depending on the isotope.

A similar process may occur but without the emission of two antineutrinos. This process is called neutrinoless double beta decay ($0\nu\beta\beta$) and its Feynman diagram is also shown in Figure

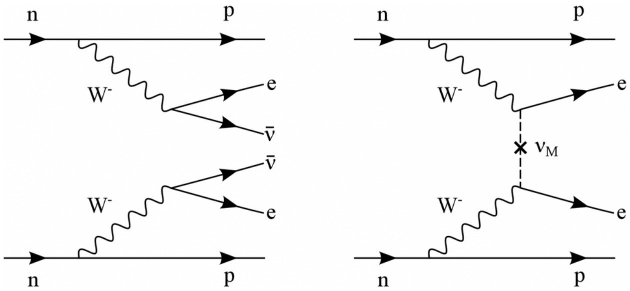

Figure 2.3: Feynman diagrams for double beta decay (left) and neutrinoless double beta decay (right).

2.3. In the simplest version of this decay, a neutrino is exchanged by the W bosons in the decay. However, this can only occur if neutrinos are Majorana. The half-life of this decay is given by:

$$(T^{0\nu}_{1/2})^{-1} = G^{0\nu}|M^{0\nu}|^2\left(\frac{m_{\beta\beta}}{m_e}\right)^2 \tag{2.29}$$

where $T^{0\nu}_{1/2}$ is the half-life of the given isotope, $G^{0\nu}$ is a phase space factor, $M^{0\nu}$ is the nuclear matrix element of the given isotope, and $m_{\beta\beta}$ is the effective Majorana mass defined by:

$$m_{\beta\beta} = \left|\sum_i m_i U^2_{ei}\right| \tag{2.30}$$

where the sum i is over the mass states, m_i are the mass eigenvalues, and U is the PMNS matrix. It is this effective Majorana mass that $0\nu\beta\beta$ is sensitive to.

Because no neutrinos are emitted in $0\nu\beta\beta$, all of the kinetic energy of the decay is transferred to the two electrons. As a result, the two electrons will have a total energy equal to the Q value of the decay. In $2\nu\beta\beta$, the electrons are emitted with a broad energy spectrum (just as in regular beta decay) because some of the energy is carried by the neutrinos. Thus the experimental signature for this decay is a peak in the energy spectrum at the Q value of the decay as shown in Figure 2.4.

A large number of experiments are searching for this signature using a variety of different techniques and isotopes. Figure 2.4 shows the current limits on this decay plotted as a function of $m_{\beta\beta}$ vs. m_{lightest} (the lightest neutrino mass eigenstate). The shaded regions show the allowed values of the phase space for the Normal and Inverted Hierarchies. The KamLAND-Zen experiment

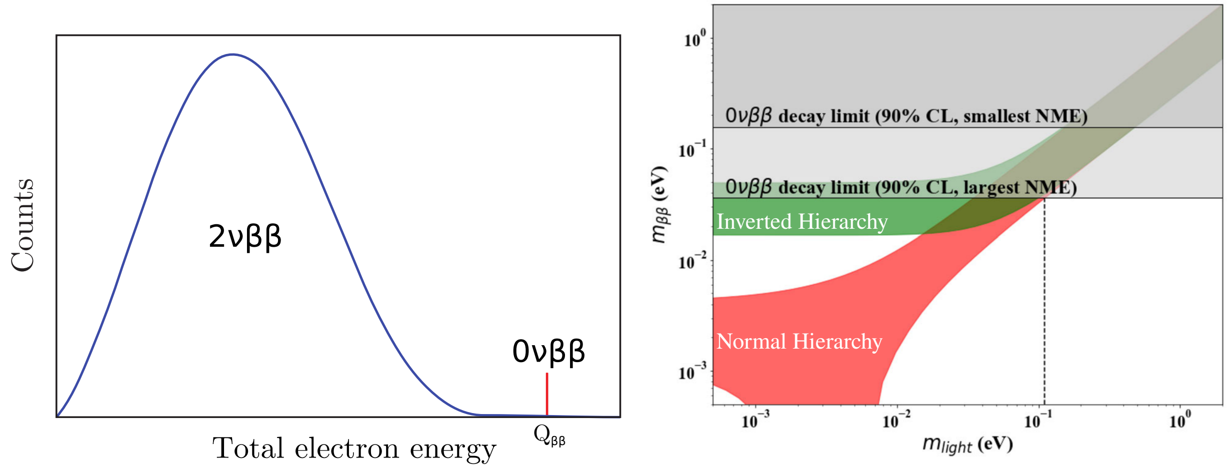

Figure 2.4: (Left) The expected energy distributions of $2\nu\beta\beta$ and $0\nu\beta\beta$ decays. Figure from [25]. (Right) Effective Majorana mass as a function of the lightest neutrino mass. The green and red bands show the allowed values in the Inverted and Normal Hierarchies. The regions excluded by the current best upper limit for the largest and smallest nuclear matrix elements ($M^{0\nu}$) [24] are shaded in gray. Figure from [26].

Oscillation Parameter	Value
Δm^2_{21}	$7.53 \pm 0.18 \times 10^{-5}$ eV^2
Δm^2_{32}	$2.453 \pm 0.0033 \times 10^{-3}$ eV^2
$\sin^2\theta_{12}$	$0.307^{+0.013}_{-0.012}$
$\sin^2\theta_{23}$	0.546 ± 0.021
$\sin^2\theta_{13}$	0.0220 ± 0.0007
δ_{CP}	$1.23 \pm 0.21 \times \pi$ rad

Table 2.1: PDG 2021 [27] best fit oscillation parameters.

provides the current leading limit on $m_{\beta\beta}$, finding $m_{\beta\beta} <$ 36-156 meV (90% CL) [24] where the range is due to uncertainties in the calculation of the nuclear matrix element $M^{0\nu}$.

2.5 Neutrino Sources and Experiments

The six parameters that govern neutrino oscillation are the three mixing angles (θ_{12}, θ_{13}, and θ_{23}), the two independent mass squared differences (typically Δm^2_{21} and Δm^2_{32} are chosen), and the CP violating phase (δ_{CP}). All six parameters have now been measured experimentally with δ_{CP} being the least well constrained ($\delta_{CP} = 0$ has not yet been excluded at 5σ). Table 2.1 shows the current status of measurements and Figure 2.5 shows the precision of measurements over time for the neutrino oscillation parameters.

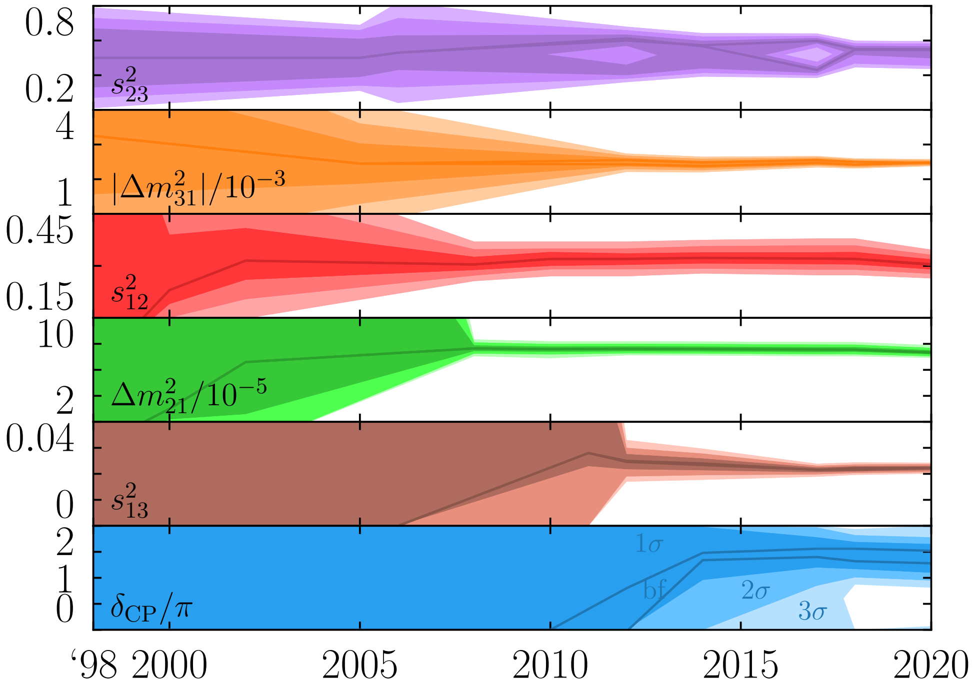

Figure 2.5: The six oscillation parameters and the precision of their measurement over time. From [28].

While many sources and experiments have contributed to our understanding of neutrinos and neutrino oscillation, this section gives an overview of those most relevant to the study of reactor antineutrinos. This includes solar and reactor neutrinos which have been used to measure the oscillation parameters θ_{12}, θ_{13}, Δm_{21}^2, and Δm_{32}^2. In addition, geoneutrinos, an interesting neutrino signal and a background to reactor antineutrinos are also discussed.

2.5.1 Reactor Neutrinos

The source of neutrinos used both for their initial discovery and for the main analysis of this thesis is nuclear reactors. Nuclear reactors produce enormous fluxes of $\bar{\nu}_e$ with energies of up to $\sim$10 MeV which can then be detected through the inverse beta decay (IBD) interaction $\bar{\nu}_e + p \rightarrow e^+ + n$. The energy spectrum of reactor antineutrinos as well as their product with the IBD cross-section are shown in Figure 2.6. Only $\bar{\nu}_e$ can undergo the IBD interaction at these energies and so reactor neutrino experiments typically search for the disappearance of $\bar{\nu}_e$ to probe the neutrino oscillation parameters.

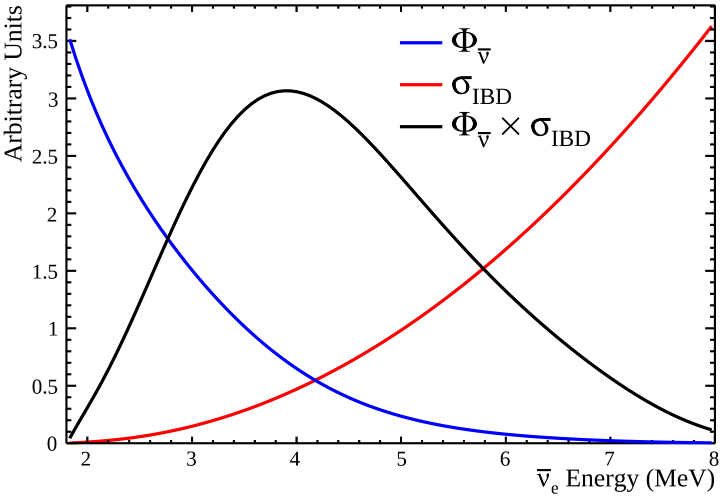

Figure 2.6: The energy spectrum of reactor antineutrinos before and after accounting for the IBD cross-section.

Using Equation 2.10, the oscillation probability, $P_{\bar{\nu}_e \to \bar{\nu}_e}$, is given by:

$$\begin{aligned} P_{\bar{\nu}_e \to \bar{\nu}_e}(L, E) = 1 - & \cos^4(\theta_{13}) \sin^2(2\theta_{12}) \sin^2\left(\frac{\Delta m^2_{21} L}{4E}\right) \\ & - \sin^2(2\theta_{13}) \Bigg(\cos^2(\theta_{12}) \sin^2\left(\frac{\Delta m^2_{31} L}{4E}\right) + \sin^2(\theta_{12}) \sin^2\left(\frac{\Delta m^2_{32} L}{4E}\right)\Bigg) \end{aligned} \tag{2.31}$$

This value is referred to as the "survival probability" and the terms dependent on L/E are often rewritten in the units typically used by these experiments:

$$\frac{\Delta m^2_{ij} L}{4E} = 1.27 \frac{\Delta m^2_{ij}[\text{eV}^2] L[\text{m}]}{E[\text{MeV}]} \tag{2.32}$$

The distances between the reactors and the experiments (L) are known and the energy of the incident neutrinos (E) can be measured, isolating the effect of the oscillation parameters. Figure 2.7 shows the survival probability averaged over the energy spectrum of reactor neutrinos as a function of L. A small decrease in the survival probability can be seen at $L \approx 2$km. This decrease is primarily due to the third and final term in Equation 2.31 whose maximum amplitude depends on $\sin^2(2\theta_{13})$. This length scale is referred to as "short baseline" and is optimal for measurements of θ_{13} and Δm^2_{32}.

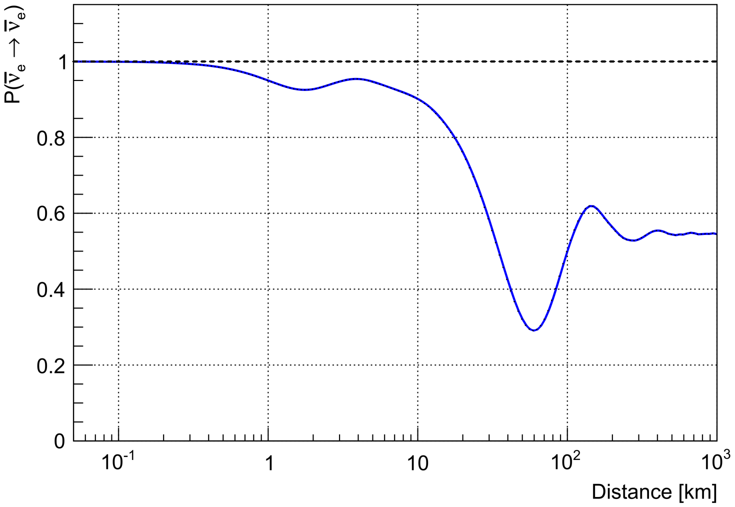

Figure 2.7: Survival probability averaged over the energy spectrum of reactor antineutrinos as a function of distance (L). Adapted from [29].

A large decrease in the survival probability can be seen at ∼60 km. This decrease is primarily due to the second term in Equation 2.31. At this length scale, the term $\sin^2(\frac{\Delta m^2_{21} L}{4E})$ can undergo a few oscillations across the range of neutrino energies provided by nuclear reactors. This length scale is referred to as "medium baseline" and is optimal for measurements of θ_{12} and Δm^2_{21}.

Short Baseline Reactor Neutrino Experiments

At short baselines, the survival probability can be approximated as:

$$P_{\bar{\nu}_e \rightarrow \bar{\nu}_e}(L, E) \approx 1 - \sin^2(2\theta_{13}) \Bigg(\cos^2(\theta_{12}) \sin^2\left(\frac{\Delta m^2_{31} L}{4E}\right) + \sin^2(\theta_{12}) \sin^2\left(\frac{\Delta m^2_{32} L}{4E}\right)\Bigg) \tag{2.33}$$

Initial measurements of θ_{13} from short baseline experiments found no evidence of neutrino oscillation [30] [31]. This inspired several theoretical models with θ_{13} equal to or near 0. Three short baseline reactor antineutrino experiments were then designed with the goal of precisely measuring θ_{13}: Double Chooz in France, RENO in South Korea, and Daya Bay in China.

The detectors used by these experiments were quite similar. All three detectors consisted of a liquid scintillator target with photomultiplier tubes (PMTs) to detect the light produced in the IBD interactions. The scintillator was doped with gadolinium to improve their sensitivity to the

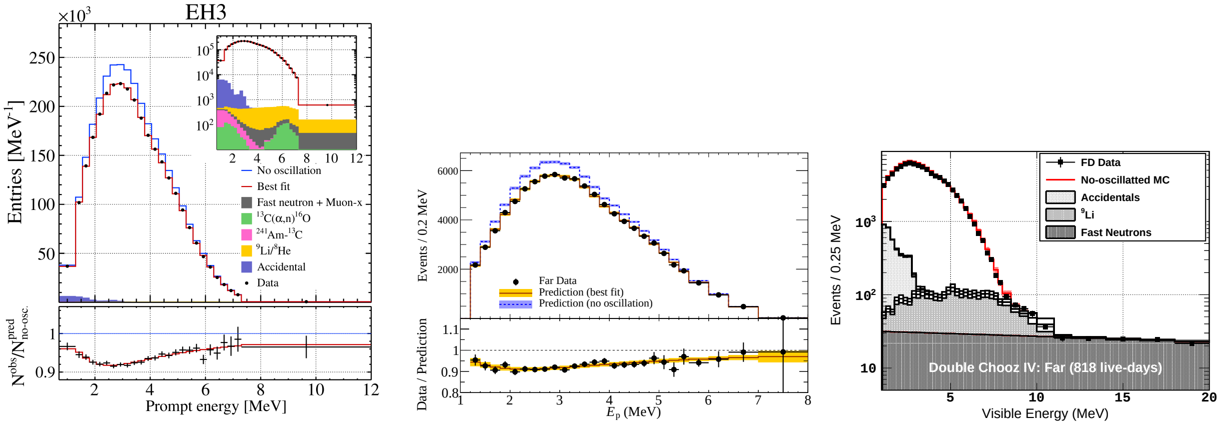

Figure 2.8: Measured energy spectra at the Daya Bay [32] (left), RENO [33] (middle), and Double Chooz [34] (right) far detectors. All three experiments see $\bar{\nu}_e$ disappearance consistent with $\theta_{13} \approx 8^\circ$ and $|\Delta m^2_{32}| \approx 2.5 \times 10^{-3}$ eV^2.

neutron capture signal used to identify the IBD interactions. All three experiments used multiple detectors, with at least one "near" detector placed closer to the reactor to measure the antineutrino flux and at least one "far" detector placed $\sim$1 km from the reactor to observe the disappearance.

Each experiment uses the same technique to measure both θ_{13} and Δm^2_{32}. The flux measured at the near detector is used to predict the expected flux at the far detector independent of the modeling of the reactor. A deficit of detected neutrinos at the far detector allows measurement of the disappearance probability of the neutrinos. The amplitude of this disappearance is determined by θ_{13} while the energy dependence of this disappearance is determined by Δm^2_{31} and Δm^2_{32}.

The three experiments have found consistent results which were reported for $\sin^2(2\theta_{13})$: 0.0851 ± 0.0024 for Daya Bay [32], $0.0896 \pm 0.0048(\text{stat}) \pm 0.0047(\text{syst})$ for RENO [33], and 0.105 ± 0.014 for Double Chooz [34]. These results correspond to $\theta_{13} \approx 8^\circ$ and the detected energy spectrum for each experiment is shown in Figure 2.8. It is known that $\Delta m^2_{21} << \Delta m^2_{32} \approx \Delta m^2_{31}$ and Equation 2.33 shows that these experiments are only sensitive to the magnitude of Δm^2_{32} so these experiments often report their measurement as $|\Delta m^2_{32}|$ or report two different values dependent on the mass hierarchy. These experiments find that $|\Delta m^2_{32}| \approx 2.5 \times 10^{-3}$ eV^2.

In addition to their oscillation measurements, these experiments have also published detailed

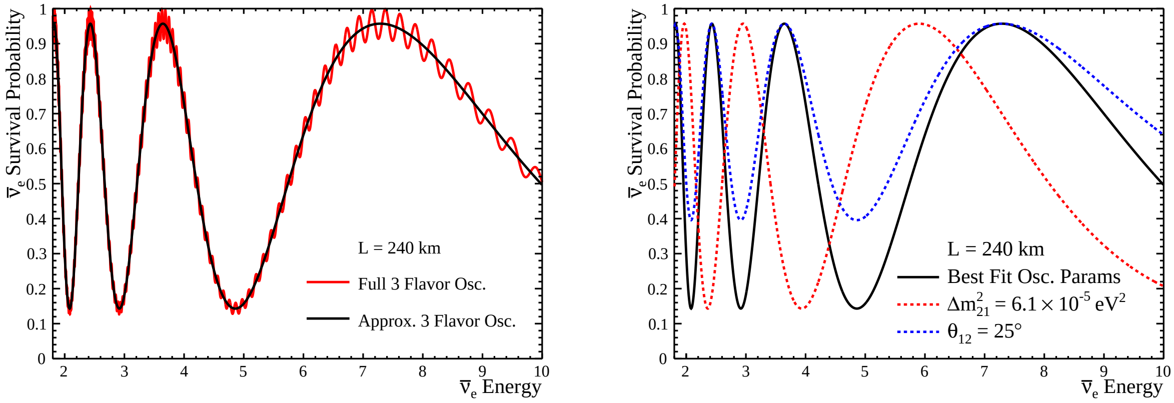

Figure 2.9: (Left) Survival probability for L = 240 km using both the full 3 flavor oscillation and the approximation averaging over the high frequency oscillation. (Right) The approximated survival probability with the current best fit oscillation parameters compared with different values of Δm^2_{21} and θ_{12}.

measurements of the reactor antineutrino flux which will be used for the prediction and uncertainties of the reactor antineutrino signal in Chapter 6.

Medium Baseline Reactor Neutrino Experiments

Figure 2.9 shows the oscillation probability at $L = 240$ km as a function of energy across the reactor antineutrino energy range. This is chosen because the dominant source of neutrinos reaching SNO+ (the Bruce Nuclear Generating Station) is a distance of 240 km away from the detector.

The high-frequency oscillation is due to the third term in Equation 2.31. These terms can be averaged over to approximate the survival probability as:

$$P_{\bar{\nu}_e \rightarrow \bar{\nu}_e}(L, E) \approx 1 - \frac{1}{2}\sin^2(2\theta_{13}) - \cos^4(\theta_{13})\sin^2(2\theta_{12})\sin^2\left(\frac{\Delta m^2_{21} L}{4E}\right) \tag{2.34}$$

Figure 2.9 also shows this approximate survival probability plotted for two different values of Δm^2_{21} and two different values of θ_{12}. The difference in the oscillation probabilities for different values of Δm^2_{21} and θ_{12} is what allows its measurement in reactor antineutrino experiments. It can also be seen from Figure 2.9 that the value of θ_{12} affects the amplitude of the oscillation and Δm^2_{21} affects the frequency.

Currently, the only experiment to measure reactor antineutrinos at a medium baseline is KamLAND. The result from SNO+ will be just the second measurement of its type. The KamLAND and SNO+ experiments are fairly similar in principle. Both contain ∼1 kiloton of liquid scintillator surrounded by many PMTs to detect the light produced by interactions within the detector. A more detailed description of SNO+ is given in Chapter 3.

The KamLAND detector consists of a 13 meter diameter balloon filled with 1 kiloton of liquid scintillator. It is surrounded by mineral oil which provides shielding to the detector and is viewed by 1300 PMTs at ∼9 m radius which provide ∼34% photocoverage of the detector. A diagram of the KamLAND detector is shown in Figure 2.10.

The KamLAND detector is located ∼1 km underground in the Kamioka Observatory in Kamioka, Japan which results in a cosmic muon rate of ∼0.3 Hz. It is surrounded by ∼50 nearby Japanese reactors with a flux-weighted average baseline (L_0) of 180 km. These reactors provide a rate of ∼1-2 reactor antineutrino interactions per day in KamLAND.

KamLAND took data for ∼7 years, and the results across its three data taking periods are shown in Figure 2.10. This figure also shows the survival probability plotted as a function of L_0/E for the data after subtraction of backgrounds. KamLAND found the best fit values for the oscillation parameters $\Delta m^2_{21} = 7.53 \pm 0.18 \times 10^{-5}$ eV^2 and $\tan^2(\theta_{12}) = 0.436^{+0.029}_{-0.025}$ [36]. This result is the current most precise measurement of Δm^2_{21}.

Compared to SNO+, KamLAND has a slightly larger detector (13 m radius vs. 12 m radius) and is located much closer to the surface resulting in a higher cosmic muon rate (∼0.3 Hz vs. ∼3/hour). SNO+ has more PMTs and slightly more photocoverage but the experiments have comparable energy resolution.

For this measurement, the most significant difference between KamLAND and SNO+ is the distribution of reactors around the detector. Maps of nearby reactors are shown in Figure 2.11, drawn approximately to scale. There are many more reactors near the KamLAND detector than the SNO+ detector. This results in a ∼4× larger flux of reactor antineutrinos in KamLAND. However,

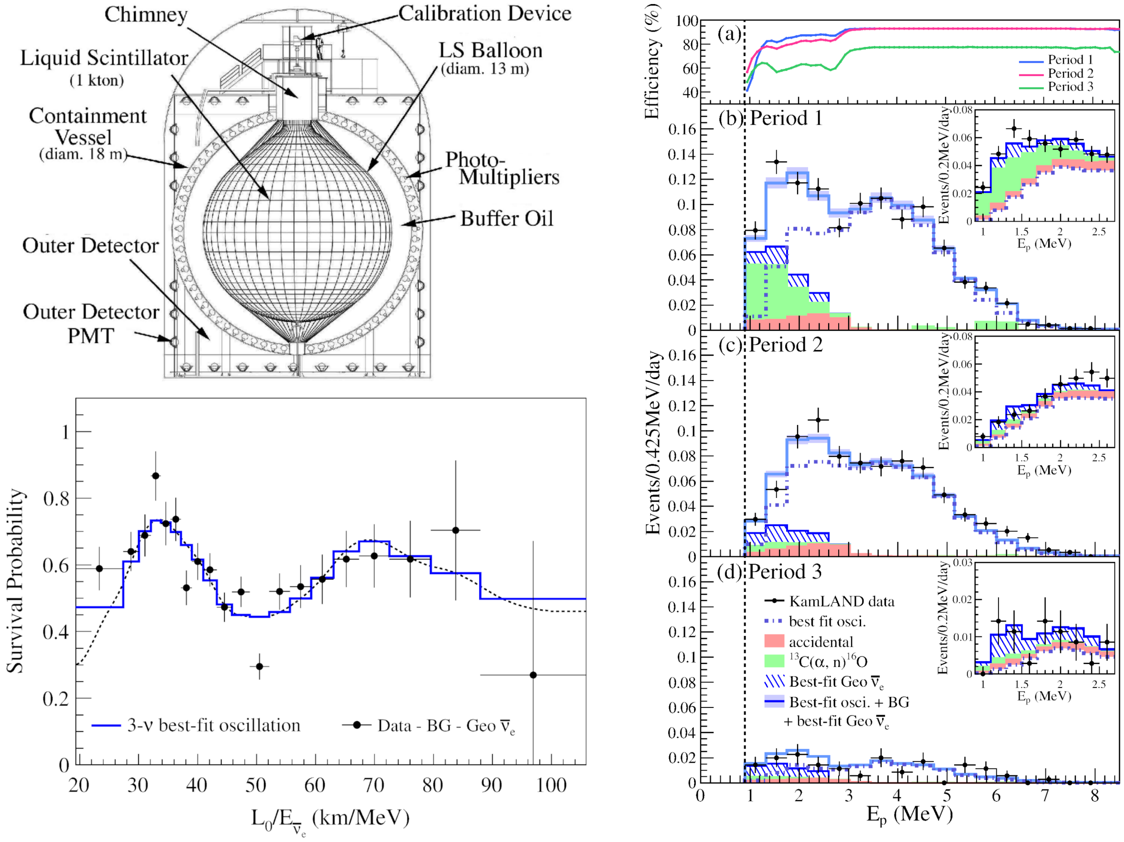

Figure 2.10: A diagram of the KamLAND detector (top left) [35] and the most recent result from KamLAND. The right figure shows the observed energy spectrum of reactor antineutrinos over three periods while the bottom left figure shows the background subtracted survival probability as a function of $L_0/E_{\bar{\nu}_e}$ [36].

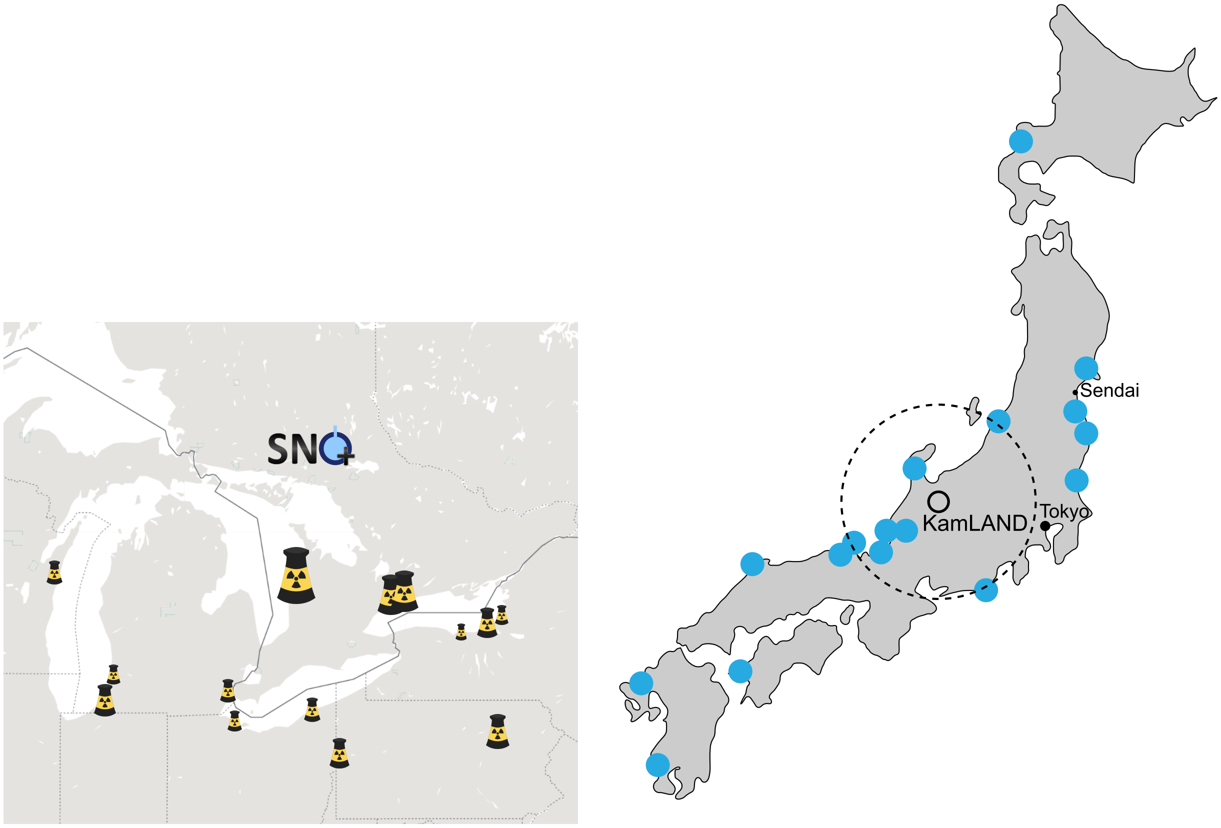

Figure 2.11: Maps of nearby reactors for the SNO+ experiment (left) and the KamLAND experiment (right) [37]. Maps are drawn approximately to scale. Reactor sizes are scaled to their design power for the SNO+ map.

the many reactors all sit at various locations with different baselines (L). Because the oscillation probability depends on the combination of $(\Delta m^2_{21} \times L)/E$, accounting for multiple baselines (L) reduces the sensitivity to Δm^2_{21}.

In SNO+, ~60% of the reactor antineutrino flux comes from just three Canadian reactor complexes at $L = 240$ km, 340 km, and 350 km. The closest complex, Bruce, is the second largest nuclear reactor complex in the world and it alone produces ~40% of the flux at SNO+. As a result, the features in the energy spectrum due to oscillation are more well preserved in comparison to KamLAND. It is this advantage of SNO+ that results in a better expected sensitivity to Δm^2_{21} than KamLAND for the same amount of livetime.

This then leads to a question of what the optimal baseline would be to measure oscillation

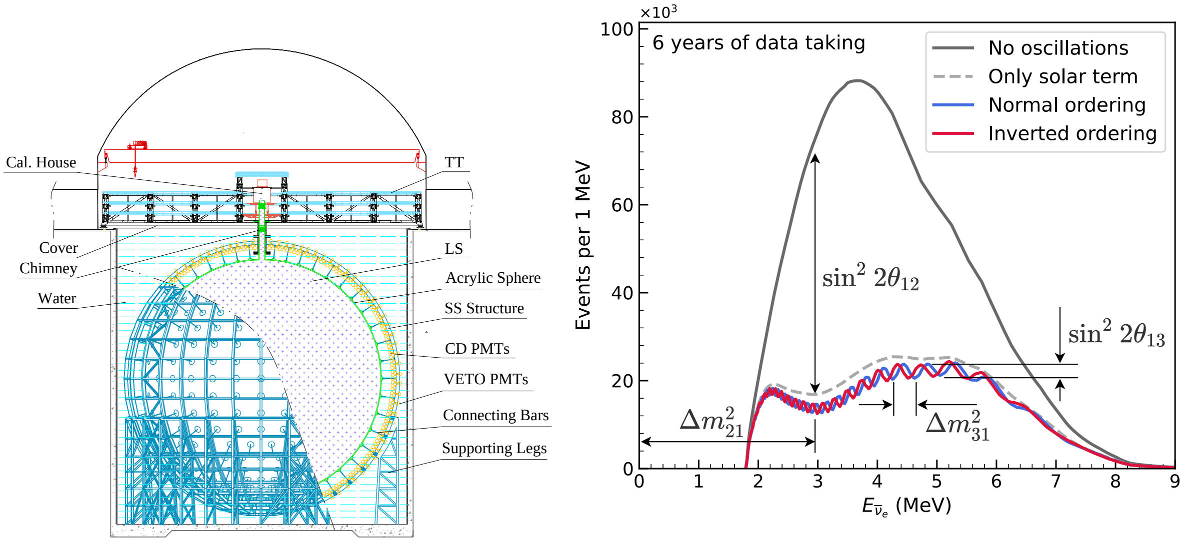

Figure 2.12: (Left) A diagram of the JUNO detector. (Right) The expected energy spectrum of reactor antineutrinos arriving at JUNO annotated to show which features are affected by each oscillation parameter [38].

parameters using reactor antineutrinos. The Jiangmen Underground Neutrino Observatory (JUNO) experiment is currently in construction and aims to measure 4 neutrino oscillation parameters including 3 at sub-percent precision [38]. This measurement will require a huge number of detected reactor antineutrinos and an unprecedented 3% energy resolution at 1 MeV. Its design is in principle the same as SNO+ and KamLAND however it is much larger and has taken advantage of the current knowledge of the oscillation parameters to place itself at the optimal location for this measurement.

JUNO is designed to be a 35 m diameter, 20 kiloton liquid scintillator detector with ∼18000 large 20-inch PMTs and ∼26000 small 3-inch PMTs yielding ∼78% photocoverage. A diagram of the JUNO detector is shown in Figure 2.12.

JUNO is being constructed in an underground laboratory with 650 m rock overburden located at Kaiping, Jiangmen in Southern China. This location was chosen to provide a baseline of ∼50 km to two nuclear power plants with the third closest ∼300 km away. As a result, JUNO expects ∼50 reactor IBD interactions per day with >90% of coming from a baseline L of 52-53 km. The expected energy spectrum of reactor antineutrinos arriving at JUNO is shown in Figure 2.12. This plot also shows the features of the energy spectrum which allow measurement of the oscillation

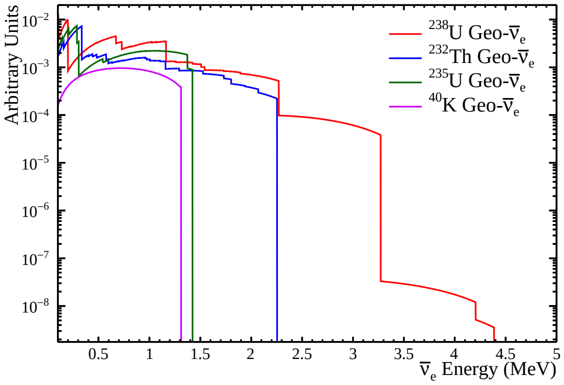

Figure 2.13: Energy spectra of the various processes within the Earth that produce geoneutrinos.

parameters as well as the difference expected between the normal and inverted hierarchies.

2.5.2 Geoneutrinos

β decays of radioactive isotopes within the crust and mantle of the Earth produce an observable flux of antineutrinos at the surface of the Earth. These geoneutrinos come from many different baselines and are produced with energies up to $\sim$3 MeV. Figure 2.13 shows the energies of the various processes which produce geoneutrinos. Much like reactor antineutrinos, geoneutrinos are detected through inverse beta decay. In fact, geoneutrinos are a background to the analysis of reactor antineutrinos and vice versa.

However, geoneutrinos are on average less energetic than reactor antineutrinos, and only neutrinos with energy > 1.8 MeV can interact via IBD. Also, because of the large variation in baselines, the energy dependence in their survival probability averages out. This survival probability is:

$$P_{\bar{\nu}_e \to \bar{\nu}_e}(L, E) \approx \cos^4(\theta_{13})\left(1 - \frac{1}{2}\sin^2(2\theta_{12})\right) + \sin^4(\theta_{13}) \approx 0.55 \tag{2.35}$$

In addition, the oscillation parameters are better understood than the flux of geoneutrinos. As a result, rather than using geoneutrinos to measure oscillation parameters, the known oscillation parameters are used to convert a measured oscillated flux of geoneutrinos to a flux produced by the Earth. Because Earth models provide a range of predictions of the geoneutrino flux, sufficiently accurate measurements of the flux can actually constrain these models. Measurement of geoneutrinos can provide insight into the radiogenic heat production in the Earth and the abundance of radioactive isotopes at depths that cannot be accessed by geological surveys.

The predictions from geological models and measurements of geoneutrino fluxes are typically reported in Terrestrial Neutrino Units (TNU) which correspond to the number of antineutrino IBD interactions per year for a target with 10^{32} free protons. Geoneutrino models provide a range of expectations from ~35-60 TNU for the location of SNO+, however, the crustal contribution of the geoneutrino flux varies resulting in different predictions at different locations.

Geoneutrino Experiments

Two experiments have measured the geoneutrino flux: KamLAND in Japan and Borexino in Italy. SNO+ aims to be the third experiment to report a measurement of geoneutrinos and the first in North America. The principle of Borexino is again the same as that of KamLAND and SNO+: a large liquid scintillator detector viewed by PMTs.

Borexino is smaller than SNO+ and KamLAND, containing only ~300 tons of liquid scintillator within an 8.5 m diameter inner balloon. However, Borexino has achieved the lowest intrinsic radioactivity of any comparable experiment and also has fewer nearby reactors than SNO+ or KamLAND, significantly reducing backgrounds. KamLAND also has several years of data taken with a much reduced flux of reactor antineutrinos due to an extended shutdown of Japanese nuclear reactors.

Both experiments have measured the flux of geoneutrinos using the observed energy spectrum of IBD events. The measured energy spectra (with backgrounds subtracted from the plot for KamLAND) are shown in Figure 2.14. Borexino obtained a result of $47.0^{+8.4}_{-7.7}(\text{stat})^{+2.4}_{-1.8}(\text{syst})$ TNU [39] while KamLAND obtained a result of $28.6^{+5.1}_{-4.8}$ TNU [40]. The values of these results may appear to be in slight tension with each other but the differences in the local geology may be the cause. This makes additional measurements at different locations such as SNO+ especially interesting.

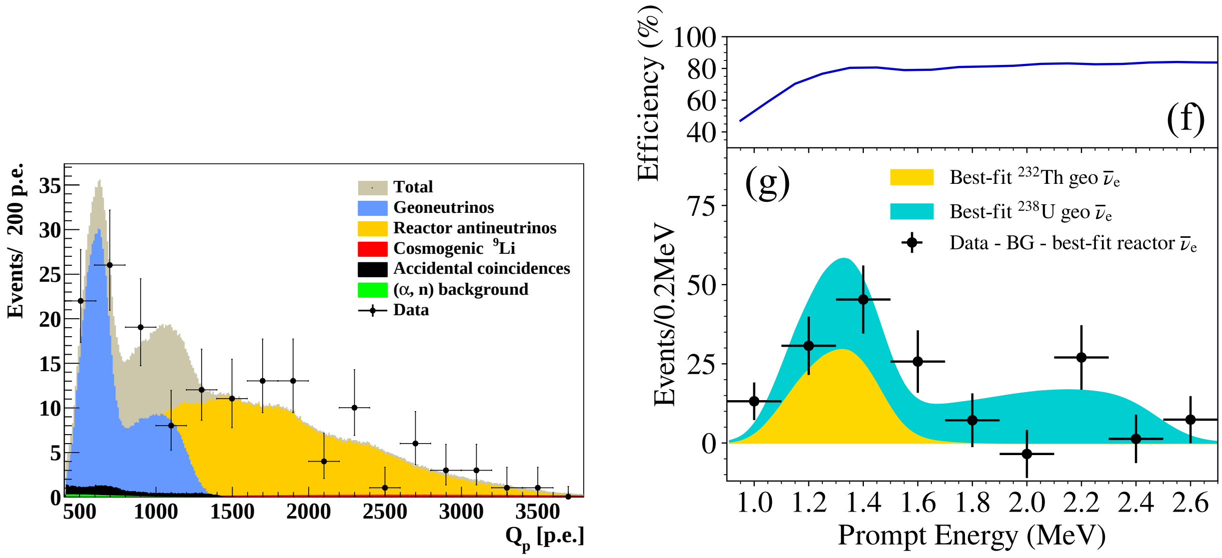

Figure 2.14: The measured energy spectra of the geoneutrino signals in Borexino (left) [39] and KamLAND (right) [40]. The KamLAND result has backgrounds subtracted from the plot.

2.5.3 Solar Neutrinos

The Sun produces an enormous flux of neutrinos through nuclear fusion reactions within its core. Two separate chains of nuclear reactions produce neutrinos with energies up to ∼10-20 MeV. These chains produce neutrinos in 8 separate processes each with their own characteristic energy spectrum and expected flux. Figure 2.15 shows the energy spectra of the neutrinos emitted in these nuclear processes.

Solar neutrinos are unique because they travel through large distances of highly dense matter that are not achievable on Earth. As a result, they can experience significant matter effects as described in Section 2.3.2. In fact, the condition for the MSW resonance can be achieved for neutrinos above 5 MeV at the densities within the Sun. In addition, the sign of this effect depends on the sign of Δm^2_{21}.

Also, the electron densities within the Earth are sufficient to provide non-negligible matter effects at large enough distances. During the day, solar neutrinos only pass through the atmosphere and the relatively small overburden of the underground experiments, however, at night, solar neutrinos must travel large distances through the Earth and arrive in a matter enhanced state. This

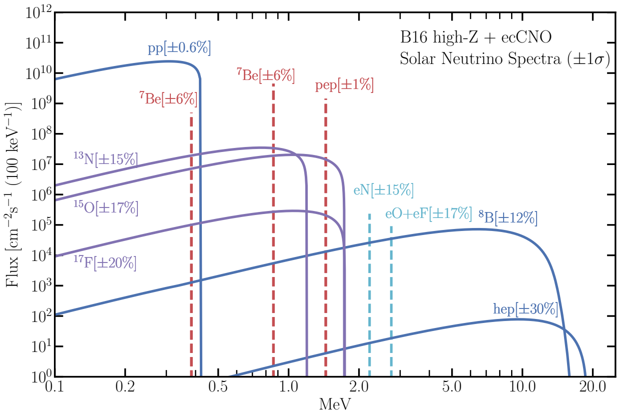

Figure 2.15: Energy spectra of neutrinos emitted in the various nuclear processes within the Sun. From [41].

"day-night" effect is dependent on Δm^2_{21} and provides a second (less sensitive) method of measuring this oscillation parameter.

Solar Neutrino Experiments

There is a long history of experiments studying solar neutrinos, however, the sensitivity to oscillation parameters comes primarily from two experiments, SNO and Super-Kamiokande (Super-K). The SNO experiment was the predecessor to SNO+ and used nearly the same detector. The primary difference is that SNO used a heavy water (D_2O) target. This allowed the detection of all three neutrino flavors through three separate interaction channels:

$$\text{Charged Current: } \nu_e + d \rightarrow e^- + p + p \tag{2.36}$$

$$\text{Neutral Current: } \nu_x + d \rightarrow \nu_x + n + p \tag{2.37}$$

$$\text{Elastic Scattering: } \nu_x + e^- \rightarrow \nu_x + e^- \tag{2.38}$$

Where most experiments only have access to the elastic scattering channel.

Super-K uses a 33 kton ultra-pure water target and is located 1 km underground in Kamioka, Japan (in the same laboratory as KamLAND). Interactions in both the heavy and light water targets of SNO and Super-K produce Cherenkov light which is their method of detection. Compared to scintillation light, much less Cherenkov light is produced by a particle of the same energy, however, the light is emitted in the direction of travel of the particle. Comparison of this direction to the expected direction of solar neutrinos provides a large reduction in backgrounds.

Super-K and SNO have taken many years of data providing a huge amount of statistics for the study of solar neutrinos. The most recent result was obtained by Super-K performing a combined fit using all available solar neutrino data. This result gives best fit oscillation parameters of $\sin^2\theta_{12} = 0.307^{+0.013}_{-0.012}$ and $\Delta m^2_{21} = 4.8^{+1.3}_{-0.6} \times 10^{-5}$ eV^2 [42]. The sensitivity to Δm^2_{21} comes primarily from the Day-Night effect. Figure 2.16 shows the observed Day-Night effect in Super-K.

While Borexino has detected geoneutrinos, its primary goal was the study of low energy solar neutrinos. Borexino's unprecedented radiopurity and low background levels along with its much improved energy resolution in comparison to SNO and Super-K allow the experiment to perform detailed studies of solar neutrinos using the detected energy spectrum of events in the detector. While SNO and Super-K have provided precise measurements of the flux of neutrinos created in ^{8}B decays within the Sun, Borexino has measured the fluxes of the lower energy solar neutrinos created in the pp, ^{7}Be, and pep reactions. These measured fluxes can be used to determine the survival probability of solar neutrinos as a function of energy. Figure 2.16 shows the measured survival probabilities for the different solar neutrinos as a function of energy. It can be seen that the survival probability changes as a function of energy. This is due to the matter effects within the Sun and the decrease as a function of energy implies that Δm^2_{21} is positive.

2.6 Measurements of Δm^2_{21} and θ_{12}

There are two existing methods used to measure Δm^2_{21}. The most precise measurement, and the only current measurement using reactor antineutrinos, comes from KamLAND: $7.53^{+0.18}_{-0.17} \times 10^{-5}$ eV^2 [36] and was described in Section 2.5.1. An additional measurement using solar neutrinos comes from a combined analysis of all available solar neutrino data performed by Super-K: $\Delta m^2_{21} = 4.8^{+1.3}_{-0.6} \times 10^{-5}$ eV^2 [42][1] which was described in Section 2.5.3. This result is less sensitive than the KamLAND measurement and is also in slight tension with the result at $\sim 2\sigma$. A contour

---

[1] At the time of writing this thesis, a preprint of an updated combined solar result from Super-K has been posted at [43]. This new result of $\Delta m^2_{21} = 6.10^{+0.95}_{-0.81} \times 10^{-5}$ eV^2 slightly reduces the tension between the solar and reactor measurements, however, all conclusions drawn in this thesis remain the same regardless of which result is considered.

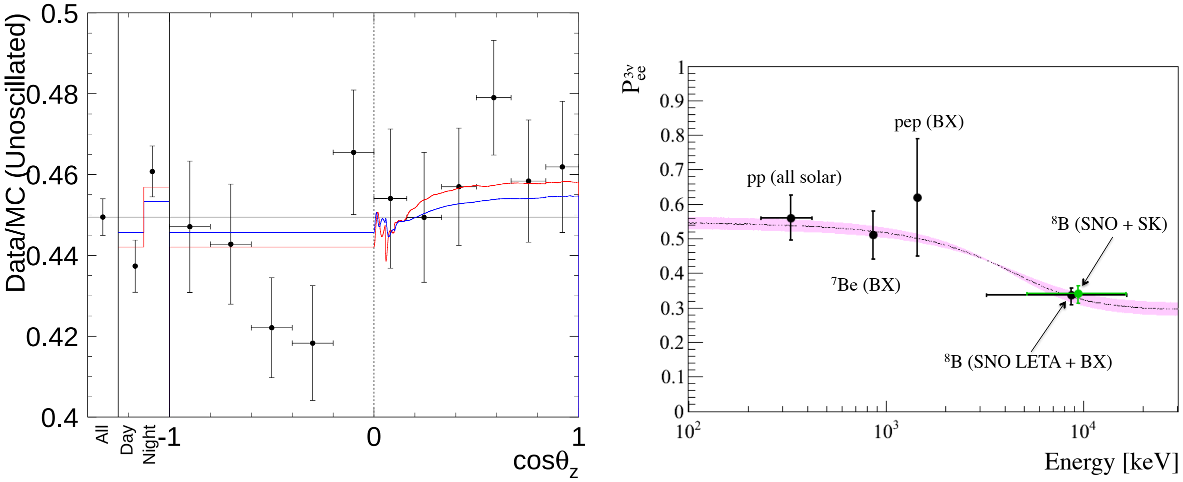

Figure 2.16: (Left) Super-K ratio of observed to expected solar neutrinos as a function of $\cos(\theta_\mathrm{z})$. θ_z is the angle between the z direction (upwards in the Super-K detector) and the direction of the incident neutrino. The red line shows the best fit result from solar neutrinos while the blue line shows the expected result for the value of Δm^2_{21} measured by KamLAND. (Right) Measured survival probabilities using several different sources of solar neutrinos. The decrease in survival probability as a function of energy implies that Δm^2_{21} is positive.

plot overlaying these two results is shown in Figure 2.17. This thesis will present the second ever measurement of Δm^2_{21} using reactor antineutrinos and provide a comparison to the two existing measurements.

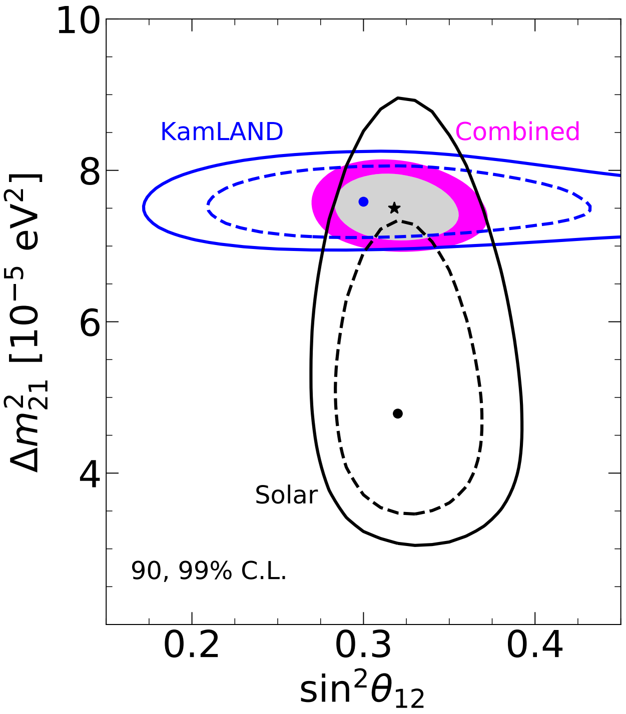

Figure 2.17: 2D contours in Δm^2_{21} vs $\sin^2\theta_{12}$ for the KamLAND result [36], the combined solar result [42], and the combination of both results. Plot from [44].

Chapter 3

THE SNO+ EXPERIMENT

The SNO+ experiment is a large liquid scintillator neutrino experiment located 2 km underground in Sudbury, Ontario, Canada [45]. This chapter describes the detector, the phases of data taking, and the goals of the experiment. Particular attention is given to the electronics and DAQ system with several improvements made to the trigger system described in the final sections of the chapter.

3.1 The SNO+ Detector

The SNO+ experiment reuses much of the infrastructure from the SNO experiment described in detail here [46]. The SNO+ detector is shown in Figure 3.1 and consists of a 5 cm thick Acrylic Vessel (AV) with a radius of 6 m, surrounded by a PMT support structure (PSUP) with a radius of 9 m. The AV holds the target volume of 900 t ultrapure water (UPW) or 780 t of liquid scintillator and is surrounded by 1.7 kt of water shielding within the PSUP.

The AV is held in place by sets of tensylon "hold-up" and "hold-down" ropes which counteract gravity and buoyant forces due to the difference in density between scintillator and UPW. The hold-up ropes are secured to the top of the cavity and to the AV at the "belly plates": regions of the AV where the acrylic is twice as thick. The hold-down ropes are secured at the bottom of the cavity and wrap around the top of the AV. At the top of the AV is the "neck", a 7 m tall cylindrical

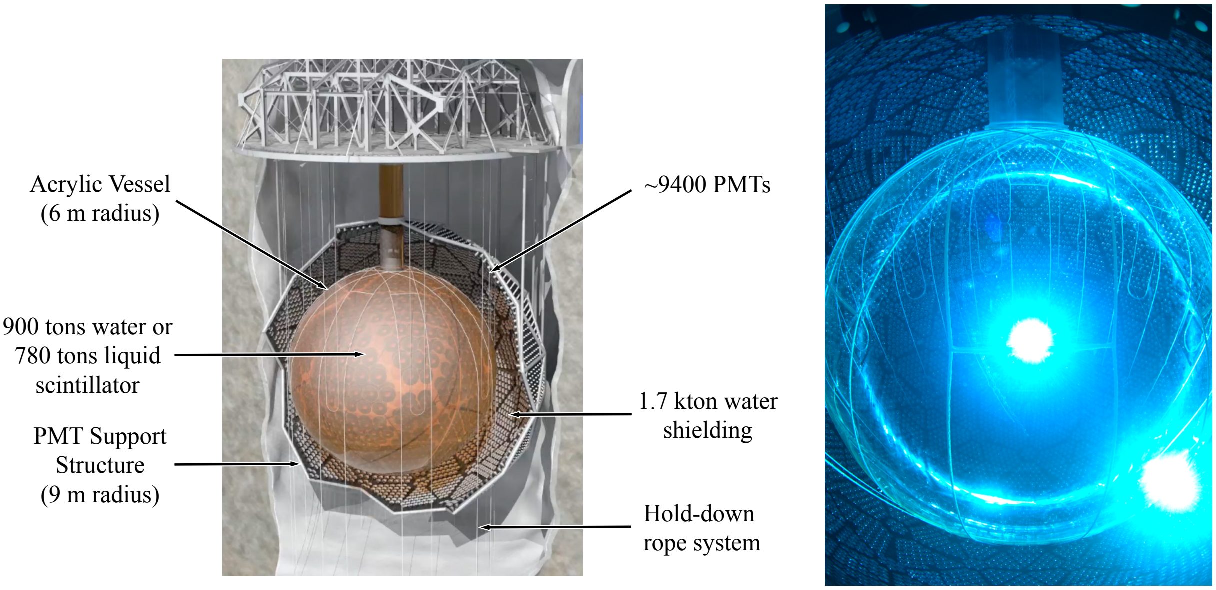

Figure 3.1: (Left) A diagram of the SNO+ detector modified from [45]. (Right) A photograph of the SNO+ detector.

structure extending upwards to the deck above, allowing access to the inner AV volume.

The PSUP is a stainless steel structure housing the ∼9400 photomultiplier tubes (PMTs) facing inward towards the AV as well as ∼90 outward-looking (OWL) PMTs. The entire structure is located in a cavity filled with UPW to further shield from backgrounds. Above this cavity is the deck, which contains the electronics and calibration systems for the experiment. An interface allowing access to the detector volume for calibration sources exists in a clean room located on the deck. A sealed cover gas system is used to protect the detector from radon ingress through this interface.

Also underground are several plants used for the purification, deployment, and recirculation of the media filling the SNO+ detector. The water plant was inherited from SNO, while the scintillator and tellurium plants were newly built for SNO+. The scintillator plant has been commissioned and used to fill the detector while commissioning of the tellurium plant is ongoing at the time of writing.

The detector is located in SNOLAB, a class 2000 clean room, 2 km underground in Creighton

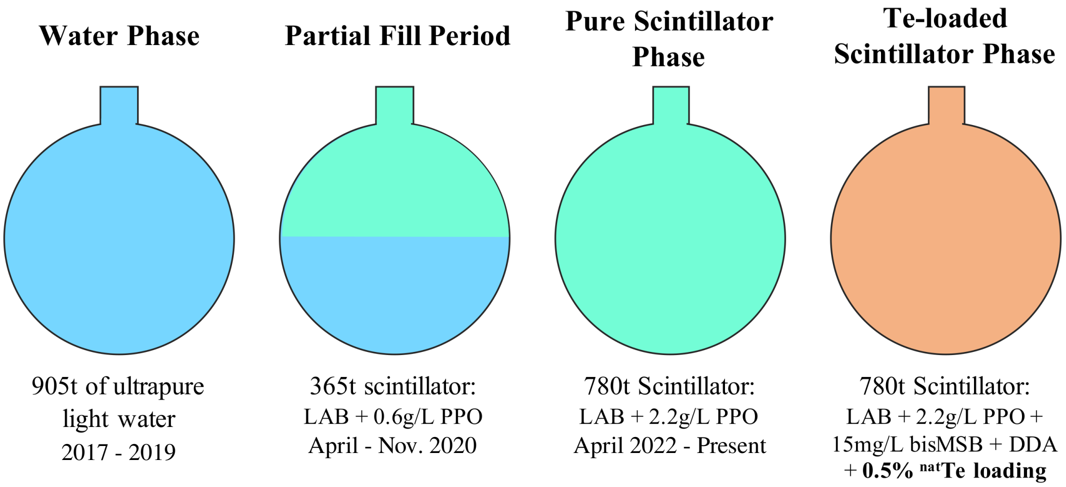

Figure 3.2: Summary and timeline of the phases of SNO+. Figure provided by A.S. Inácio [48].

Mine in Sudbury, Ontario. The location has a rock overburden of 5890 meters water equivalent (mwe) resulting in a very low muon flux of 0.27 muons/m^2/day [47] which corresponds to $\sim$3 muons per hour in the detector volume. This combination of a clean environment and low flux of cosmic rays make SNOLAB an excellent location for low background experiments like SNO+.

3.2 Phases of SNO+

The SNO+ experiment uses a phased approach, taking data with different target materials in the AV. The detection methods and goals of each phase are described here. A diagram and timeline of the phases in SNO+ is shown in Figure 3.2.

3.2.1 Water Phase

The first phase of the SNO+ experiment was the water phase. In this phase, the AV was filled with 905 t of UPW and data was taken from May 2017 - June 2019. The primary goals of the water phase were to commission the electronics and DAQ, perform calibrations, and measure backgrounds. In addition, several physics analyses were performed during the SNO+ water phase.

In the water phase, interactions were detected using the Cherenkov radiation produced by charged particles. Cherenkov radiation is produced when a charged particle travels through a medium with index of refraction n at a speed faster than the speed of light in that medium $\frac{c}{n}$.

For electrons in water, this corresponds to an energy threshold of 265 keV. SNO+ leverages several useful properties of Cherenkov light to reconstruct the position, direction, and energy of charged particles in the detector. First, the Cherenkov light is emitted at the location of the particle and the majority travels directly to the PMTs. The timing of the light reaching the PMTs can then be used to determine the position of the event. Second, the Cherenkov light is emitted at the Cherenkov angle $\cos\theta_c = \frac{1}{n\beta}$ producing a cone of light at $\theta_c \approx 41^\circ$ in water. This is used to reconstruct the direction of travel of the particle. Finally, the amount of Cherenkov photons produced scales approximately linearly with energy, causing the number of detected photons to be approximately proportional to energy. In this phase, roughly 7 photons are detected per MeV of deposited energy.

During the water phase, several calibration sources were deployed. These sources include an ^{16}N source, which provides a tagged 6 MeV γ, an AmBe source, which produces 4.4 MeV γs and neutrons, and several LED/laser calibration sources with the intensity controlled by operators. A laser calibration source was used to calibrate the water attenuation, the effective attenuation of the acrylic vessel, and the angular response of the PMTs, across different wavelengths [49]. The energy, position, and direction reconstruction was calibrated for physics analyses using the ^{16}N source [50]. In addition, the AmBe source was used to measure the neutron capture cross section and neutron detection efficiency in the detector [51].

In addition to these calibration efforts, the radioactive backgrounds from external sources were measured in water phase. Section 5.2 describes a measurement of external backgrounds performed during the water phase. This analysis used the directionality of Cherenkov light to distinguish between the sources of external radioactivity and measure the contributions from each source. The results of this analysis showed background levels consistent with the expectations used in sensitivity estimates for future phases and were used as inputs to the search for invisible nucleon decay [50].

Finally, SNO+ published several physics results using the water phase data set. This included a search for invisible nucleon decay which set world leading limits on several decay channels [50] [52], a measurement of the ^{8}B solar neutrino flux [53] [54], and the first ever detection of reactor antineutrinos in a water Cherenkov detector [55] [56].

3.2.2 Scintillator Phase

In the next phase of the SNO+ experiment, the 905 t UPW target was replaced with 780 t of liquid scintillator. Scintillator filling began in late 2019 and continued until the detector was fully filled in 2021. After completion of filling, additional compounds have been added to the scintillator cocktail to increase the amount of light detected.

Partial Scintillator Fill Phase

Limited access to SNOLAB due to the COVID-19 pandemic forced a temporary pause in filling operations with 365 t of scintillator in the detector. This period provided several months of stable data from March 2020 - November 2020 and allowed analysis and measurements of many backgrounds relevant to both the pure scintillator and Te-loaded phases of SNO+. An analysis of backgrounds to the future search for $0\nu\beta\beta$ during this phase is presented in Section 5.3. In addition, a measurement of Δm^2_{21} with limited sensitivity was performed in this phase [57] [58].

Liquid Scintillator

In scintillator phase, interactions are detected using scintillation light produced by charged particles. Scintillation light is emitted due to excitation of the molecules in the scintillator by ionizing radiation. Upon de-excitation to the ground state, the molecule fluoresces, emitting a relatively large number of photons. The wavelength distribution of the emitted photons is determined by the chemical structure of the chosen scintillator. Often, the primary solvent requires additional chemicals to shift this distribution to wavelengths more optimal for detection.

The amount of scintillation photons emitted per unit of energy absorbed by the scintillator is given by an empirical formula called Birks' law:

$$\frac{dL}{dx} = S\frac{\frac{dE}{dx}}{1 + k_B\frac{dE}{dx}} \tag{3.1}$$

where L is the total number of produced photons, S is the scintillation efficiency (in units of photons per unit energy), and k_B is Birks' constant which depends on the scintillating material.

The amount of scintillation light produced by an event in scintillator is much larger than the amount of Cherenkov light, with ∼50× more detected photons / MeV. In addition, the time profile of the light emission is on the order of tens to hundreds of nanoseconds, significantly longer than Cherenkov light which is on the order of picoseconds.

Several different particles are detected in SNO+, most commonly βs, γs, αs, and protons. However, different particles of the same energy produce a different amount of photons, a phenomenon referred to as quenching. Notably, α particles produce ∼10× fewer photons than βs of the same energy. In addition, for different particles that produce the same amount of light, the time profile of the emitted light differs. For example, the time profile for α events tends to be broader than the time profile for β events. This allows particle identification through the use of the detected time profile.

The SNO+ Scintillator Cocktail

The primary solvent in the SNO+ scintillator cocktail is linear alkylbenzene (LAB). LAB was chosen primarily due to its high light yield and radiopurity, its compatibility with the SNO+ acrylic, and its reasonable cost. Chemically, LAB consists of a benzene ring connected to a long hydrocarbon chain and has a chemical composition of $C_6H_5C_nH_{2n+1}$ where n ranges from 9 to 13.

2,5-Diphenyloxazole (PPO) is used as the primary fluor and has a chemical composition of $C_{15}H_{11}NO$. PPO was loaded into the scintillator to reach a final concentration of 2.2 g/L in April 2022, greatly increasing the scintillation light yield.

1,4-bis(2-methylstyryl)benzene (bisMSB) is used as a secondary fluor to shift the wavelength of the scintillation light, improving detection efficiency and thus further improving the light yield. Addition of bisMSB in the detector is ongoing at the time of writing and has been shown to increase the light yield by ∼50%.

Some of the most important properties of the SNO+ scintillator cocktail include the light yield, time emission profile, and optical properties, which have been measured by SNO+ collaborators. In the full fill scintillator phase, with 2.2 g/L PPO and before addition of bisMSB the light yield was measured to be ~275 PMT Hits / MeV, and the calibration of the timing profile and optical properties are described in Section 4.3. These are the conditions of the scintillator for the data used in the analysis of reactor antineutrinos presented in Chapters 6-9.

Scintillator Phase Goals

Many of the goals in scintillator phase are similar to those in water phase, including further commissioning of the electronics and DAQ, performing calibrations, and measuring backgrounds. The liquid scintillator greatly increases the light yield and thus the data rate that must be handled by the electronics and DAQ. Calibrations of the detector in scintillator phase are described in more detail in Section 4.3. In addition, all backgrounds not associated with loading Te can be measured and studied to ensure they are within expectation.

Furthermore, several physics analyses can be performed in this phase. First, SNO+ has reported the first demonstration of event-by-event direction reconstruction in a large-scale liquid scintillator experiment [59]. Also, solar neutrinos can be used to probe oscillation parameters as well as the solar neutrino fluxes [60]. In addition, several analyses searching for exotic physics such as extraterrestrial antineutrinos [61], high-mass dark matter, and fermionic dark matter are ongoing. Finally, Chapters 6-9 describe a measurement of Δm^2_{21} using reactor antineutrinos performed in this phase. Additional comments on the measurement of geoneutrinos using the same analysis are also presented.

3.2.3 Tellurium Phase

In the final phase of SNO+, the 780 t liquid scintillator target will be loaded with 1.3 t of ^{130}Te. The primary goal of this phase is to search for neutrinoless double beta decay ($0\nu\beta\beta$) in ^{130}Te. The Q value of ^{130}Te is 2.5 MeV and Figure 3.3 shows the expected energy distribution of a $0\nu\beta\beta$ signal with the expected backgrounds in SNO+. Several of these backgrounds are either well-understood or have been measured in the water or scintillator phases. Two analyses of these backgrounds are described in Chapter 5. SNO+ aims to reach a sensitivity to the ^{130}Te $0\nu\beta\beta$ half-life of 2×10^{26} years in 3 years of data taking.

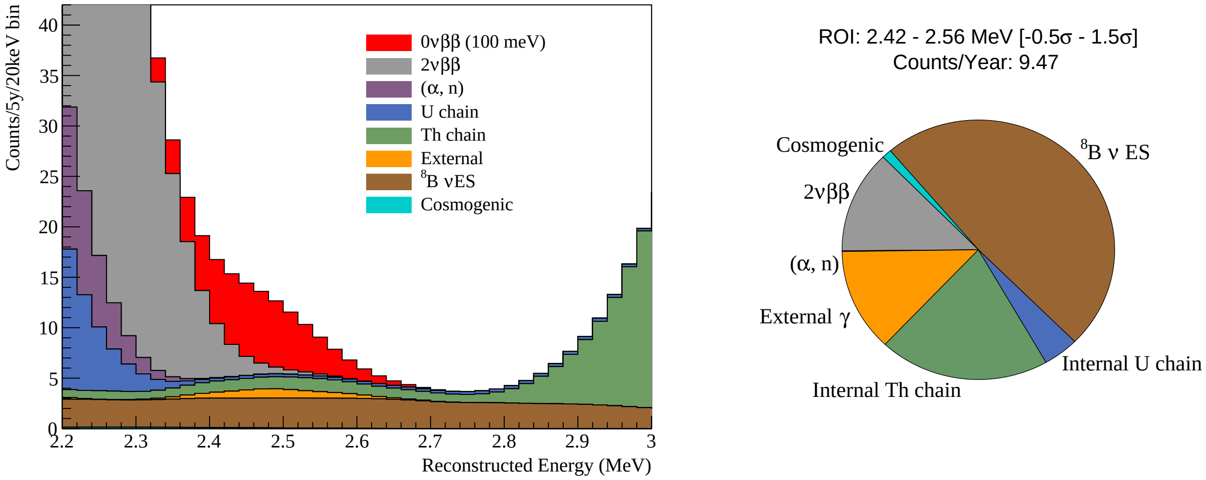

Figure 3.3: Expected reconstructed energy distribution of the $0\nu\beta\beta$ signal and backgrounds, as well as a pie chart showing the breakdown of backgrounds in the region of interest (2.42-2.56) MeV.

3.3 PMTs, Electronics, and DAQ

Interactions within the SNO+ detector produce photons. While the mechanisms of photon production change between phases, the methods of photon detection do not. Detection of the produced photons by the PMTs allows information about the processes that produced the light to be inferred. A chain of custom electronics boards is then used to digitize and read out the information obtained from the PMTs. This process is described in the following section.

3.3.1 PMTs

Photomultiplier tubes (PMTs) are used to detect photons produced in the SNO+ detector. PMTs consist of a glass tube coated with a metallic film called a photocathode. When a photon reaches the photocathode, it may produce a photoelectron (p.e.) via the photoelectric effect. A voltage of ~2000V is applied across the PMT, which accelerates the p.e. to several layers of dynodes which when struck, emit more electrons. This process amplifies the signal from the initial photon to a detectable current of electrons often referred to as a "hit".

The SNO+ detector reuses the 8" R1408 Hamamatsu PMTs originally used in the SNO experiment. During the upgrade from SNO to SNO+, ~75% of the ~800 PMTs that had failed

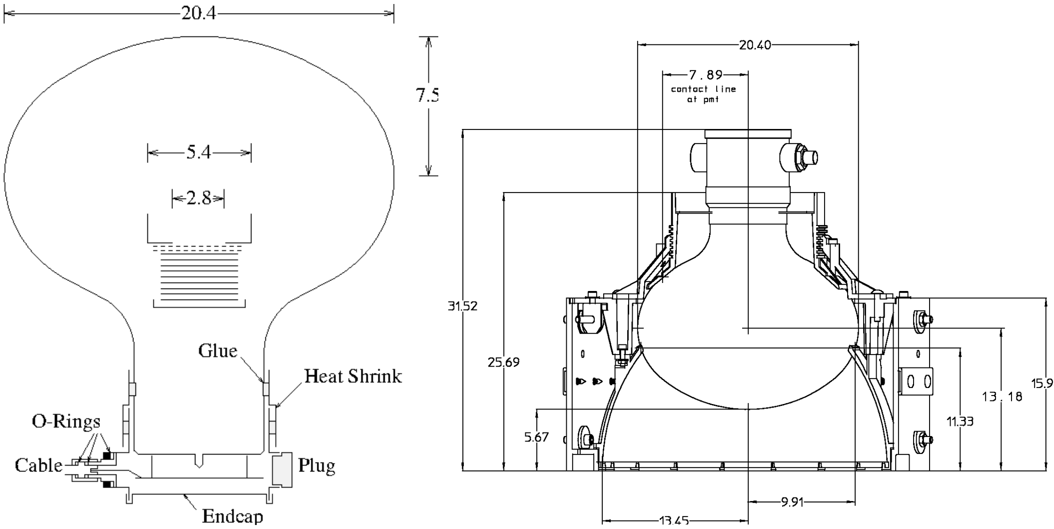

Figure 3.4: Diagrams of a SNO+ PMT including its waterproof housing (left) and the hexcell which holds the PMTs and their concentrators in the PSUP (right) [46].

throughout the running of the SNO experiment were repaired and re-installed for SNO+. A diagram of a SNO+ PMT and its housing is shown in Figure 3.4.

Each PMT is placed within a waterproof housing, and surrounded by a 27 cm diameter light concentrator. This concentrator consists of an array of reflective petals arranged in a Winston cone designed to reflect light toward the photocathode. Taking into account the angular acceptance and reflectivity of the concentrators, the effective coverage of the SNO+ PMT array is ~50%.

Accurate measurement of the properties of PMT hits is necessary to reconstruct information about events. PMTs must efficiently detect when a photon reaches the photocathode, and accurately measure the time the hit occurred and the charge deposited. The SNO+ PMTs have timing resolution of ~1.5 ns and a dark noise rate of ~500 Hz. The detection efficiency as a function of wavelength, single photoelectron charge resolution, and time resolution are shown in Figure 3.5.

3.3.2 SNO+ Electronics and DAQ Chain

After a photon produces a signal on a PMT, the signal is converted to usable data via the SNO+ electronics and data acquisition system (DAQ). The SNO+ experiment uses a chain of mostly custom built electronics to do this conversion and decide what data is worthy of being saved.

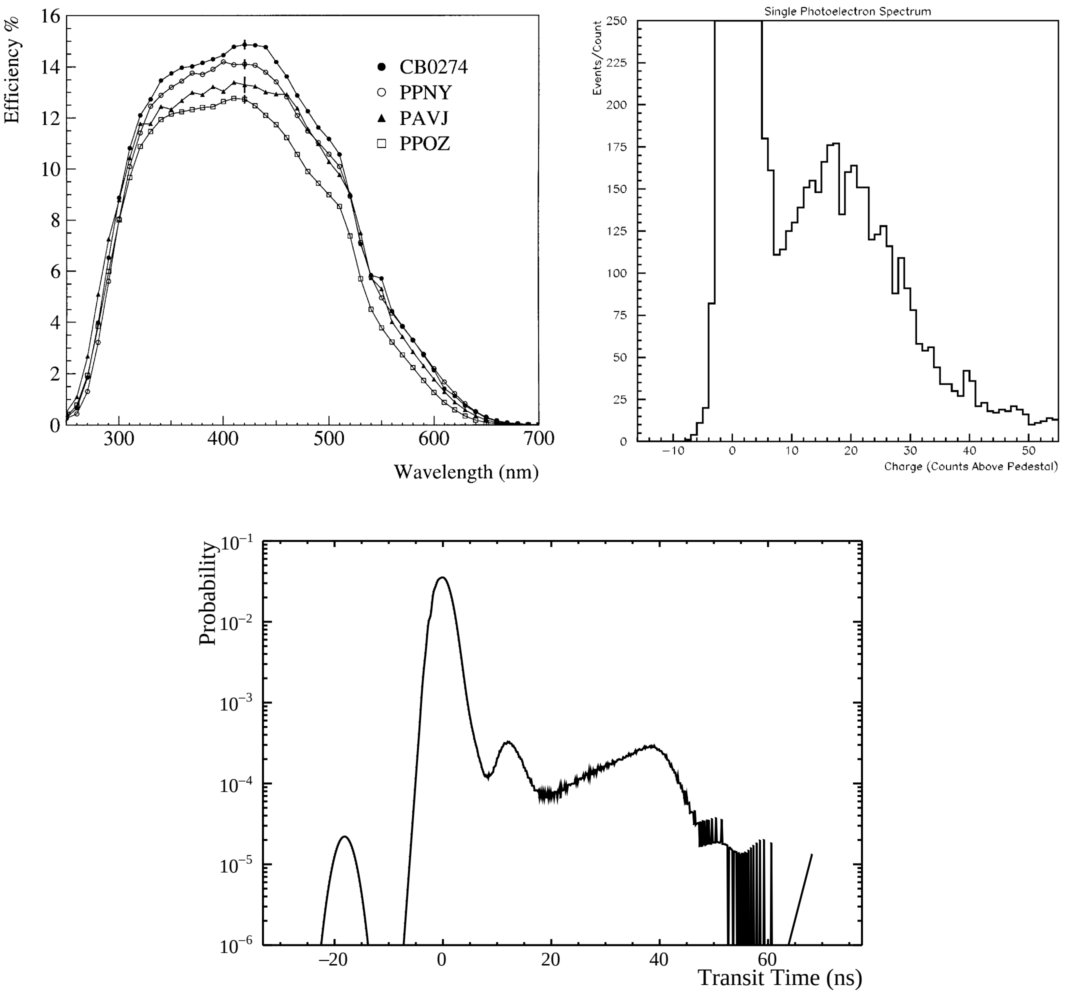

Figure 3.5: Measured properties of the SNO+ PMTs. The top left figure shows the measured efficiency of several R1408 PMTs as a function of wavelength [62]. The top right figure shows the measured single photoelectron charge spectrum [45]. The bottom figure shows the transit time probability for the PMTs as modeled in simulation.

Figure 3.6: Images of a SNO+ rack holding two crates (left) and the central electronics rack (right).

A significant portion of this hardware was inherited from the SNO experiment, however, several upgrades were necessary to handle the higher rates associated with the increased light yield from the liquid scintillator target. These electronics measure the time and charge of each PMT that detects a photon and packages them into "events" of all hits that occurred in a ∼420 ns window.

The SNO+ electronics system consists of 19 crates, each servicing 512 PMTs. Each crate consists of 16 PMT interface cards (PMTICs), 16 Front End Cards (FECs), 1 Crate Trigger Card (CTC), and 1 XL3, as well as high and low voltage backplanes. High and low voltage power supplies provide the necessary voltages for the PMTs and electronics in each crate. All of the crates are held in electronics racks on the deck above the detector with most racks housing two crates. An image of a rack holding two crates is shown in Figure 3.6. In addition, a central electronics rack reads out global event information and takes inputs from each crate to determine when the data should be saved. This central rack consists of 7 Analog Master Trigger Cards (MTC/A+), 1 Digital Master Trigger Card (MTC/D), 1 Trigger Latch board, 2 Trigger Utility Boards (TUB and TUBii), and 1 CAEN v1720 digitizer. An image of this central rack is shown in Figure 3.6 and a schematic of the full system is shown in Figure 3.7.

High voltage supplies reside in each crate to provide about 60 mA of current at the voltage (∼2000V) necessary for the operation of the 512 PMTs. The voltage is sent from the power supplies,

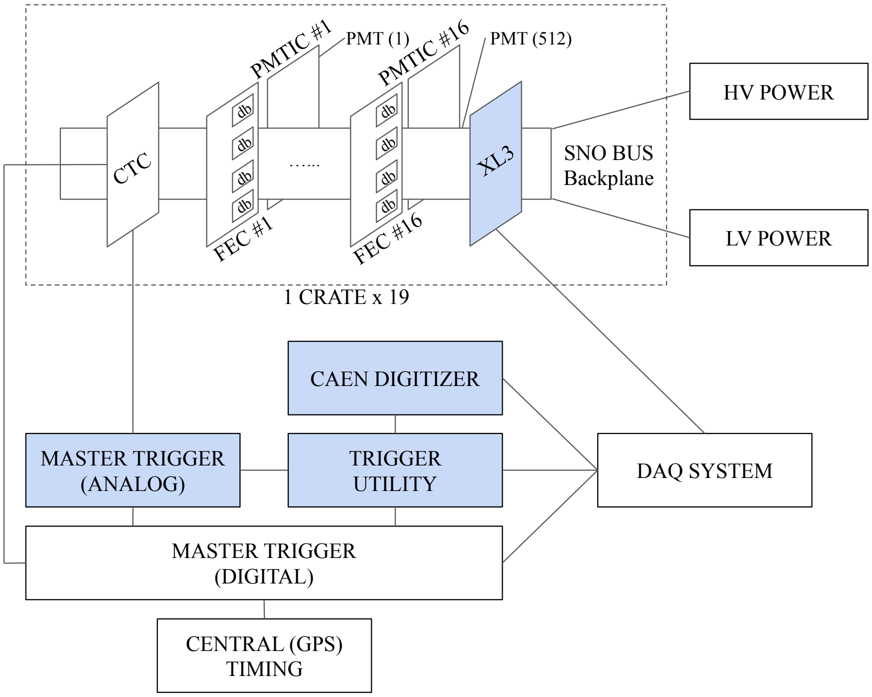

Figure 3.7: A schematic of the SNO+ electronics with new and updated components highlighted in blue.

across the high voltage backplane before reaching the PMTICs. Every PMTIC provides fanout of the HV to 32 PMT channels and contains 4 relays, each capable of disconnecting the HV from 8 channels. An array of feed-through resistors on the PMTIC allows slight adjustments to the voltage provided to each PMT. These resistor values are tuned to ensure a similar gain across all PMTs.

Waterproof coaxial cables carry both the HV and the PMT signals between the PMTIC and the PMTs. The PMTIC uses an HV-blocking capacitor to decouple the PMT signal from the supplied DC voltage. This signal is then sent directly to the FEC for use by the trigger system.

The FEC also services 32 channels and holds 4 daughter boards (DBs) which handle the PMT signals for 8 channels each. The DB contains several custom ASICs that convert the PMT signals to usable values and create the trigger signals used to determine when to save those values. The PMT signals are sent to a four channel custom "discriminator" chip. This chip compares a channel's incoming PMT signal to a programmable "channel threshold". When the PMT signal crosses this threshold it is referred to as a "hit" and several processes are initiated.

A custom "integrator" chip integrates the PMT signal to produce three measures of the charge of the hit. These charge values are a high-gain short-time integral (QHS), a high-gain long-time integral (QHL), and a low-gain short-time integral (QLX) where short is ~50 ns and long is ~400 ns. In addition, a linear voltage ramp begins on a custom "CMOS" chip to measure the time since the hit occurred (TAC). The CMOS chip also contains 16 analog memory cells for each measurement to store the values until they are read out. In addition to these four signals (QHL, QHS, QLX, and TAC), each channel will read out the crate, card, and channel number used to identify the location of the hit PMT as well as a global trigger ID number (GTID) used to compile the hit PMTs into events.

After a hit occurs, the CMOS chip will create two square current pulses (~35 mA) used for triggering, one ~100 ns in length (N100) and one ~20 ns in length (N20). In addition, the integrator shapes the input PMT signal and outputs high and low gain copies (ESUMH and ESUML) used in triggering. These trigger signals are sent from the DB to the FEC where the top and bottom 16 channels are summed and sent across the backplane, to the CTC. Each trigger signal for the entire crate is summed separately on the CTC. Each CTC then outputs the crate-wide sum of each signal: N100, N20, ESUMH, and ESUML. The trigger signals for the OWL PMTs are summed separately in the same manner and are also output by the three CTCs in crates with OWL PMTs. Only the N100, ESUMH, and ESUML versions are used and are typically labeled OWLN, OWLEHI, and OWLELO. These 7 summed trigger signals are then sent from the CTCs to the MTC/A+s.

There are 7 MTC/A+s in the SNO+ detector, one for each trigger signal. The MTC/A+ takes one trigger signal from each of the 19 CTCs and produces a detector-wide analog sum of the trigger signal. It creates three separate versions of this sum with separate gains where the highest gain has the best signal to noise ratio and the lowest has the largest dynamic range. For the N100/N20 trigger signals, the amplitude of this signal is roughly proportional to the number of PMTs hit in the previous 100/20 ns. This sum is then compared against a programmable "trigger threshold". The MTC/A+ will emit a "raw trigger", a 20 ns square pulse, that is sent to the MTC/D to indicate when the sum has crossed this threshold. The MTC/A+ also has a Complex Programmable Logic

Device (CPLD) which runs firmware allowing it to emit triggers when other conditions are met. More details about other features of the MTC/A+ will be discussed in Sections 3.3.3 and 3.5.2.

The MTC/D is the board ultimately responsible for triggering the detector by emitting a global trigger (GT). All of the raw-trigger signals from the MTC/A+s are sent to the MTC/D. The MTC/D also has several additional available trigger inputs that can be used to trigger the detector. When receiving a raw trigger from one of its inputs the MTC/D can choose to either emit a GT ("masking in" a trigger) or to do nothing ("masking out" a trigger). When the MTC/D emits a GT, it saves which trigger types caused the GT, the time of the GT, and an ID number (GTID) assigned to the event. The MTC/D also generates a signal called lockout (LO), a 420 ns long pulse during which the MTC/D will not emit another GT. The GT is then sent back to the crates to initiate readout of the PMT hit information in this 420 ns window.

The GT is sent from the MTC/D to the CTC, across the backplane, and to the FECs and DBs in each crate. Each channel automatically resets its TAC ramp and clears all data ∼400 ns after it is hit. Therefore, when the GT arrives, only channels hit within the last ∼400 ns will stop the TAC ramp and read out their data. All channels keep track of the GTID independently and a signal is sent every 2^{16} events to flag and correct the GTID for any channel that has fallen out of sync.

After the GT arrives, data from each channel is buffered into memory on the FEC and sent across the backplane to the XL3. The XL3 then asynchronously reads the data out over Ethernet to the DAQ computers. In addition to the measured values already mentioned, digitized versions of the N100, N20, and ESUMH trigger signals are saved. The MTC/A+ has an analog output of its trigger sum which is sent to the Trigger Utility Board II (TUBii), where the dynamic range of the signal is adjusted to the input range of the CAEN v1720 digitizer. The CAEN board digitizes the three trigger signals and reads them out along with the GTID necessary to associate the waveforms with events.

The DAQ computers run servers that interface with the hardware and read out the data.

The XL3 and both MTCs send and receive commands from the xl3-server and mtc-server on these DAQ computers. The data-server receives the PMT data from the XL3s, the trigger data from the MTC/D, and the digitized trigger signals from the CAEN and relays this data to any subscribed client.

The primary client of this server is the "Event Builder", often referred to as just the Builder. The Builder receives all data from the data-server and uses the GTID to associate hits with each other. Once the Builder has received all PMT information associated with a specific GTID, it packages the event into a data structure. This structure is then written to a file in a custom format. Data is typically broken into hour long periods called "runs". Each run is assigned a number, and information about each run such as the type (e.g. Physics, Maintenance, Calibration, etc.), and activity occurring during the run (e.g. water recirculation, people working on deck, etc.) is saved. Once a data file reaches 1GB in size, it is saved, closed, and moved to separate data storage computers to be processed and analyzed.

3.3.3 SNO+ Electronics Upgrades

Several upgrades were necessary to handle the higher rates associated with the increased light yield from the liquid scintillator target. More details about these upgrades are given here. Pictures of each of the new boards are shown in Figure 3.8.

XL3

In SNO, data was read out serially, one crate at a time, at a maximum rate of ∼250 kB/s using the XL1 and XL2. The XL3 replaces these boards with the primary purpose of increasing the maximum readout rate and providing an updated interface for control and readout of the electronics and high voltage supplies.

The XL3 hosts a Xilinx ML403 board [63] which contains a Xilinx Vertex-4 FPGA, a PowerPC processor, 64 MB of SDRAM, and a CompactFlash card. The CompactFlash card stores the firmware running on the Vertex-4 FPGA and C code which runs on the PowerPC processor. The firmware on the FPGA pulls the readout data from the FECs across the backplane while C code

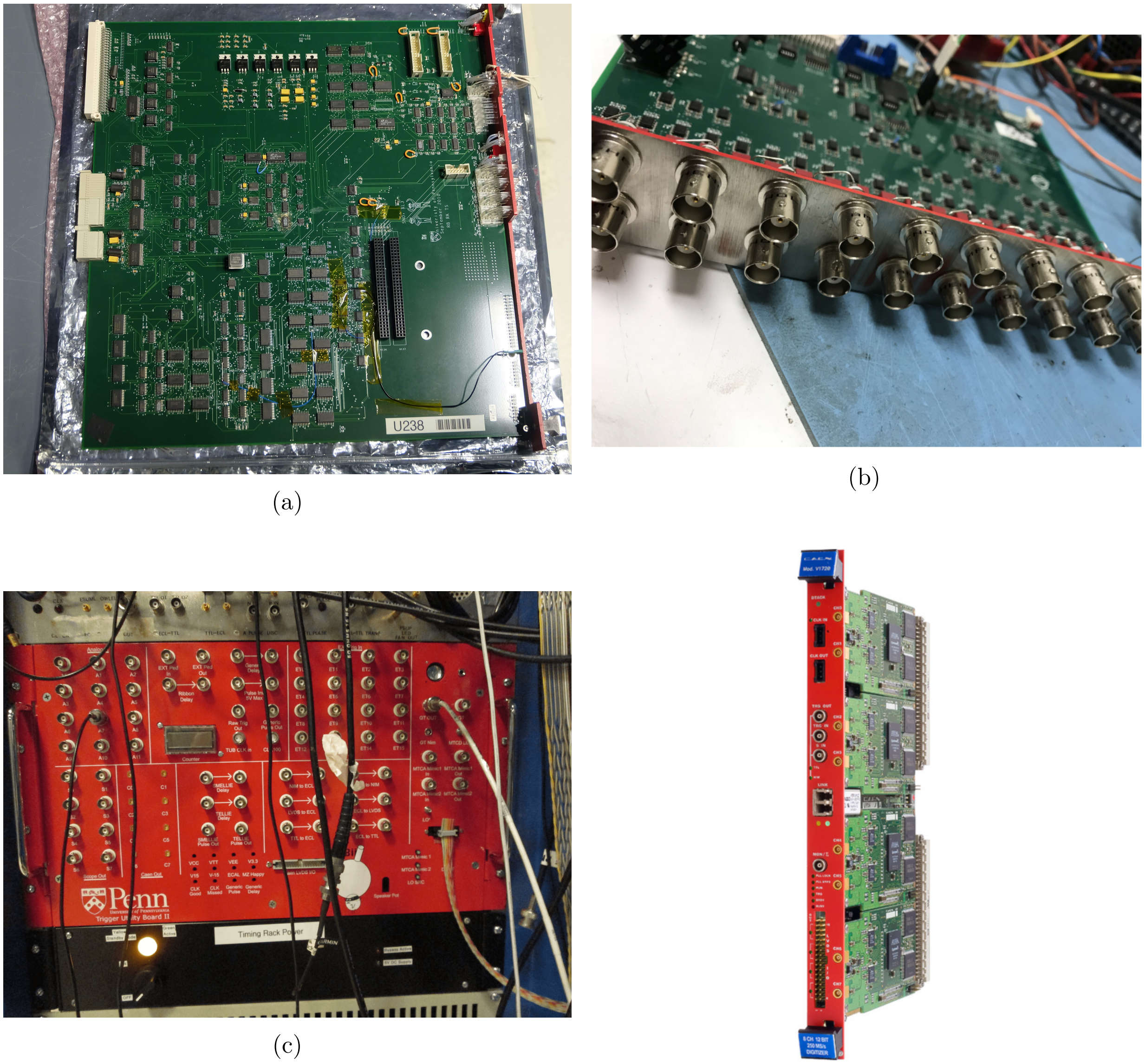

(a)

(b)

(c)

(d)

Figure 3.8: Pictures of new boards designed for the SNO+ electronics upgrade: (a) XL3, (b) MTC/A+, (c) TUBii, and (d) CAEN v1720.

running on the PowerPC processor buffers the data from the FPGA onto the local memory. The data is then sent to a central DAQ computer over Ethernet using TCP/IP protocols. This allows each XL3 to read out data at a maximum rate of ∼14 MB/s, giving a total rate of ∼250 MB/s, ∼1000× faster than the SNO readout.

MTC/A+

In SNO, the MTC/A summed the analog trigger signals from each of the CTCs and handled the triggering logic. The MTC/A+ replaces this MTC/A to handle the higher hit rates and thus higher currents. It also provides some additional trigger functionality and a baseline restoration function designed to improve stability.

The MTC/A+ has 20 inputs, enough for all 19 crates and one spare. Each crate's input is connected via a reed relay which provides the ability to disconnect the signal from the sum in the case of instability caused by a single crate. The signals are then sent through a series of analog summing stages using operational amplifiers. In these stages, the signals are summed and split into three separate gain paths providing different dynamic ranges for the same trigger signal. The output of the final summing stage for each of the three gains paths is sent to three places: the baseline restoration functionality, the analog output, and the triggering functionality.

The baseline restoration functionality uses an integrating amplifier with a long time constant to output the average voltage of the final summing stage. This signal is fed back to the non-inverting input of the final summing amplifier removing any long term DC shifts in the baseline of the signal. The time constant is of order seconds, much slower than that of the PMT signals but fast enough to quickly correct any significant shifts in the baseline during data taking. The voltage of this compensation is sent through TUBii to the MTC/D and read out to allow monitoring of the MTC/A+ baselines.

The analog output is simply a copy of the analog trigger sum. It is sent through TUBii, copied, and shaped to be sent to the CAEN digitizer which reads out the waveforms and to an oscilloscope underground for monitoring purposes.

The trigger functionality takes the outputs from the final stage summing amplifiers and inputs each into a comparator with a threshold controlled by a DAC on the MTC/A+. The signal from the comparator being high/low indicates whether the MTC/A+ is above/below the trigger threshold. The output of these three comparators, along with two additional signals (lockout and a delayed copy of the global trigger) are then sent to a Xilinx CoolRunner-II CPLD [64]. This allows customizable logic to be applied to the five input signals to determine when a trigger should be emitted. The CPLD has three trigger signal outputs, one for each gain path, which are sent to the MTC/D to trigger the detector. The standard trigger logic on the CPLD results in a raw trigger being emitted on the output of the corresponding gain path whenever the trigger signal crosses the comparator threshold for that gain path. Additional triggering logic implemented on the CPLD is discussed in Section 3.5.2.

TUBii

In SNO, the Trigger Utility Board (TUB) was used to provide a variety of useful functionality such as signal fan outs, a speaker, and signal conversions. The TUB is still used by SNO+, and its utility inspired the creation of a successor board, the Trigger Utility Board II (TUBii) to provide additional useful functionality to SNO+.

TUBii is a utility board with many different independent functions each with its own circuitry on the board. The board has ∼90 inputs and outputs, most of which use BNC ports on its front or back panel. TUBii hosts a Xilinx MicroZed [65] which contains a Zynq-7020 System on a Chip (SoC) consisting of an FPGA, and an ARM-based processor. The MicroZed also has a microSD card slot, an Ethernet port, and two 100-pin headers for input and output of signals. The firmware and software that control TUBii reside on the microSD card, and communication with TUBii is done via Ethernet. The TUBii server runs on the ARM-based processor and interprets commands, sending responses via Ethernet. Registers in the firmware control the digital outputs to the board and store the digital inputs from the board.

The most important functionality on TUBii includes:

- Clock Interface: TUBii has its own clock as well as a clock input. TUBii can select which clock is sent to the required 50 MHz clock input on the MTC/D. In addition, TUBii will automatically fall back to the other clock if it detects that the selected clock is not working.

- ELLIE Interface: TUBii provides an interface for the LED/laser calibration system. Pulsers with tunable frequencies are used by these systems to control the rate of light pulsing. In addition, TUBii controls the triggering for these calibration systems with a tunable delay and an interface to the asynchronous trigger functionality on the MTC/D.

- MTC/A+ & CAEN Interface: The analog trigger signals from the MTC/A+ are sent to TUBii which copies the signal. The -5V baseline is removed and one copy of the signal is sent out to be connected to a scope, while the other copy is shaped to the correct dynamic range before being sent to the CAEN digitizer. In addition, TUBii sends the GT and SYNC signals to the CAEN digitizer to read out the waveforms and ensure synchronization with the rest of the detector. It also sends a delayed copy of the global trigger (DGT) to the MTC/A+ to be used in its triggering logic and buffers the voltage of the baseline restoration on the MTC/A+ which is sent to the MTC/D and read out for monitoring purposes.

- TUBii Lockout: TUBii creates its own lockout signal with an adjustable length.

- Auxiliary Triggers: TUBii has 16 digital logic inputs on its front panel. These signals are sent to the FPGA on the MicroZed where customizable logic can be used to determine when to send a raw trigger to the MTC/D. TUBii also stores its own trigger word which is read out into the data.

- Pulsers, delays, and signal conversions: Several pulsers, delays, and signal conversions exist on TUBii which are most commonly used for debugging by experts.

Other Upgrades

The CAEN Digitizer: In SNO, the Analog Measurement Board (AMB) was used to measure the peak, integral, and derivative of the analog trigger sum from the MTC/A. In SNO+, the AMB has been replaced with a CAEN v1720 8 Channel 12bit 250 MS/s waveform digitizer [66]. The analog sums of the MTC/A+ are first shaped to the proper dynamic range by TUBii and then sent to the CAEN digitizer. TUBii also sends the GT and SYNC signals to the CAEN indicating when to read out the waveforms and ensuring synchronization with the rest of the detector. The 250 MS/s rate corresponds to 4 ns bins in the waveform. The CAEN digitizer reads out waveforms of the N100, N20, and ESUMH trigger signals during normal physics running. It has 8 inputs allowing additional signals to be connected and digitized. This functionality is used in some calibrations to readout an additional PMT signal that comes from the calibration system itself.

The Latch-Board: The MTC/D only records trigger signals occurring within ∼20 ns of the initial signal in the trigger word. If any triggers occur after this time but within the 420 ns trigger window, an additional bit called the "Missed trigger" bit is set high. The latch-board addresses this issue by splitting the most important trigger signals (i.e. the N100 and N20 trigger signals) before they reach the MTC/D and sending the additional copy to a modified FEC called the FEC/D. This modified FEC takes the digital inputs and reads them out as hits. The hits are then read out and can be used to infer the trigger word of an event regardless of whether the triggers occurred within the ∼20 ns trigger latch window on the MTC/D.

3.3.4 Electronics Calibration

There are two types of electronics calibrations performed in SNO+, referred to as ECALs and ECAs (both of which are short for electronics calibrations). The electronics contain two pieces of functionality to produce forced triggers essential for their calibration. The first is forced channel triggers referred to as "pedestal" signals. When a pedestal signal is sent to a channel, the channel will behave as if it received a hit despite the fact that no PMT pulse was present. The second is forced global triggers referred to as "pulseGT". The MTC/D can directly trigger the detector reading out all channels that were hit. The timing and delay between these two signals can be tuned to trigger the detector and readout all the channels the pedestal signal was sent to. These two signals allow user controlled triggering and readout to be used for calibration of the electronics.

The ECAL is responsible for setting and measuring several hardware settings on the FECs and DBs with the goal of minimizing the channel-to-channel variations across the detector. The following quantities are set and calibrated in the ECAL:

- Discriminator thresholds: The discriminator threshold is varied. The location of the baseline and the size of the noise is determined using the trigger rate at each discriminator threshold. The threshold is placed just above the noise level.

- Charge baselines: DACs on the FECs control the baseline of the charge readout. These DACs are varied to find a similar baseline for QHS/QHL/QLX across all channels in the detector.

- Charge integration times: DACs on the FECs control the slope of several voltage ramps which determine the length of the QHS and QHL charge integration windows. These DACs are varied to find integration windows of $\sim$50 and $\sim$400 ns for QHS and QHL respectively.

- Hit validity window: The length of time that a hit is valid for before being discarded is referred to as GTValid and is determined by the TAC ramp. The slope of the TAC ramp, and thus its length, is controlled by a DAC on the FEC. This DAC is varied to ensure that GTValid is shorter than Lockout (420 ns) for all channels. This is necessary to ensure that a single PMT hit cannot be read out in two different triggered events.

The ECA is then responsible for calibrating the baseline values of the measured charge (QHS/QHL/QLX) and the relationship between readout voltage (TAC) and time for each channel. This is done by first sending pedestals to each channel and measuring QHS/QHL/QLX. Because these hits are produced with no charge on the PMT, the charge readout is the baseline value.

Next, to calibrate the time readout, pedestals are sent with a known time delay between the pedestal signal and the global trigger signal. This time delay is varied, measuring the TAC value at each delay. The TAC ramp is approximately linear so a line is fit to the data for each channel to provide a conversion between TAC and hit time.

3.4 Auxiliary Triggers

As mentioned in the previous section, TUBii has digital logic inputs on its front panel which are sent to the FPGA on the MicroZed where customizable logic can be used to create auxiliary triggers. This section describes two auxiliary triggers that were designed and tested in the SNO+ detector. These triggers were motivated by the two background analyses described in Chapter 5.

3.4.1 Coincidence Trigger

The first auxiliary trigger is referred to as the "Coincidence Trigger". Typically the trigger threshold is set to the lowest value that allows stable running for extended periods of time. The goal of this trigger (as implied by the name) is to trigger on coincidence events where the delayed event produces a signal below this trigger threshold. A potential example of this is the coincidence of ^{214}BiPo decays. This coincidence consists of a ^{214}Bi β decay which produces up to $\sim$900 PMT Hits, followed by a ^{214}Po α decay which produces $\sim$250 PMT Hits and has a lifetime of 237 μs. The ^{214}Bi decay can mimic the $0\nu\beta\beta$ signal and thus, identification of the following ^{214}Po decay is critical to remove this background. In the data from the full fill scintillator phase used in this thesis, the trigger threshold was set to 25 PMT Hits, far below the $\sim$250 PMT hits produced by the ^{214}Po decay. SNO+ expects to always be 100% efficient for ^{214}Po decays, however, this trigger could potentially be used for other coincidences with low energy decays.

The trigger is implemented in firmware on the MicroZed using VHDL code. The implemented logic masks in the delayed trigger signal for a set period of time following the receipt of a prompt trigger. The prompt and delayed trigger signals are digital logic signals that are input to TUBii through one of the 16 auxiliary trigger inputs on its front panel. To allow flexibility in the trigger scheme, the prompt trigger signal, delayed trigger signal, and length of time the delayed trigger signal is masked in are set by the user. This functionality was first tested on the benchtop with a function generator used to produce the trigger inputs and in the detector. It was then tested in the detector with raw trigger signals from the MTC/A+ used as the trigger input. Both forced trigger signals and real physics data were used when testing the trigger logic in the detector. In the detector, the trigger output is sent to the MTC/D and a bit in the TUBii trigger word is assigned to this auxiliary trigger.

In the example of ^{214}BiPo, the prompt and delayed trigger signals would come from two of the gain paths on the MTC/A+. The prompt threshold could be set to $\sim$500 PMT hits, while the delayed threshold could be set to $\sim$100 PMT hits ensuring that both the ^{214}Bi and ^{214}Po events will cross their respective trigger thresholds. The time window could be set to $\sim$2 ms to ensure that $\sim$99.99% of decays fall within this window. This would ensure a high efficiency for triggering on these events even if the detector could not be run stably for extended periods of time at the lower trigger threshold.

3.4.2 Anti-Coincidence Trigger

The next auxiliary trigger is referred to as the "Anti-Coincidence" trigger. The motivation for this trigger is to preferentially trigger on events that occur in the external water at a range of PMT hits below the typical detector threshold. This would allow constant monitoring of the radioactive backgrounds in the external water, which have been observed to vary during the full fill scintillator phase.

The Anti-Coincidence trigger leverages the features of the SNO+ trigger system and the differences in the timing of Cherenkov and scintillation light to preferentially trigger on events in which only Cherenkov light is emitted. SNO+ has two main trigger signals described in the previous section: N100 and N20. The amplitude of these pulses corresponds roughly to the number of PMT hits in the previous 100/20 ns. In interactions in the SNO+ detector, the Cherenkov light is emitted on the picosecond timescale while the scintillation light is emitted over tens to hundreds of nanoseconds. As a result, the PMT hits have a broader time distribution for events in the scintillator where both scintillation and Cherenkov light is produced than for events in the water where only Cherenkov light is produced. Because nearly all of the Cherenkov light arrives within the first 20 ns, the maximum amplitude of the N100 and N20 trigger signals are similar for events occurring in the water. Conversely, because much of the scintillation light arrives after the first 20 ns, the maximum amplitude of the N100 trigger signal is typically much larger than that of the N20 trigger signal.

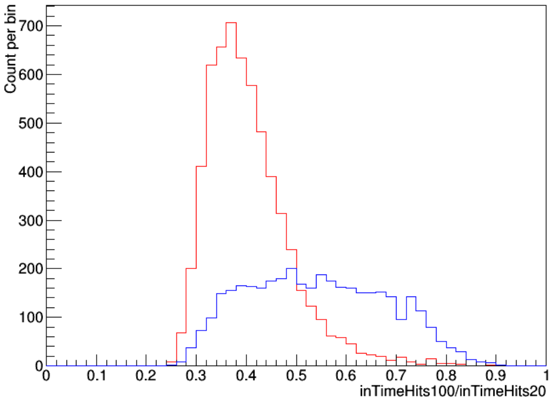

Figure 3.9: Ratio of estimates of the maximum amplitudes of the N100 and N20 trigger signals (inTimeHits100/inTimeHits20) for events simulated in the water (shown in blue) and events simulated in the scintillator (shown in red).

An estimate of the maximum amplitude of the N100 and N20 trigger signals (referred to as inTimeHits100 and inTimeHits20) is obtained for events in the water and events in the scintillator. The ratio of the maximum amplitudes is shown in Figure 3.9 where a clear separation can be seen.

The goal is then to trigger on events where the N100 and N20 trigger signals are approximately the same size. This is made slightly more challenging due to the fact that the only information readily available to be used for this trigger are the raw trigger outputs of the MTC/A+.

This trigger is also implemented in the firmware on the MicroZed using VHDL code. The implemented logic takes in two input trigger signals (one designated as prompt and one designated as delayed) as well as a short time window as inputs. When a prompt trigger is received, the logic waits for the specified time window. If no delayed trigger is received within the specified time window around the prompt trigger, a trigger is emitted. If a delayed trigger is received, no trigger is emitted. To allow flexibility in the trigger scheme, the prompt trigger signal, delayed trigger signal, and time window around the prompt trigger signal are set by the user.

In the example of preferentially triggering on a radioactive background event in the external water over one in the scintillator, the prompt and delayed trigger signals would come from the raw triggers of the N20 and N100 MTC/A+ respectively. The N20 threshold could be set to 15 PMT

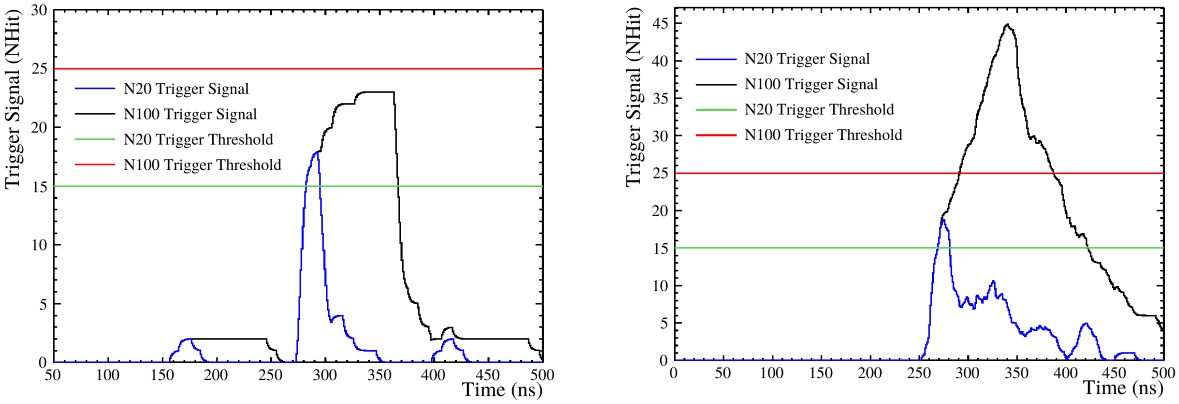

(a) Simulated background event in the external water (b) Simulated background event in the scintillator

Figure 3.10: Simulated trigger signals of a background event in the external water which would satisfy the trigger criteria described in Section 3.4.2 and of a background event in the scintillator which would fail these criteria.

hits and the N100 threshold to 25 PMT hits. The time window could then be set to an 80 ns window around the prompt trigger. Diagrams showing an example of a background event in the external water that would satisfy these trigger criteria and a background event in the scintillator that would fail these criteria are shown in Figure 3.10.

This functionality was tested both on the benchtop with a function generator used to produce the trigger inputs and in the detector with actual raw trigger signals from the MTC/A+ used as the trigger input. The trigger output is sent to the MTC/D and a bit in the TUBii trigger word is assigned to this auxiliary trigger.

Figure 3.11 shows the NHit distribution of the triggered anticoincidence events from a run in real data taken during the partial fill phase with the previously described settings. It can be seen that the trigger properly triggers on events in the correct NHit range. A peak at low NHit was observed and found to be due to noise on the N20 trigger signal causing N20 triggers without a corresponding N100 trigger. This satisfies the criteria of the trigger and thus is triggered on. Additional work was later done to reduce the probability of triggering on these noise induced triggers. The rate of triggered events that reconstruct in the water is higher than that of events that reconstruct in the scintillator. In addition, the rate of events in the water increases close to

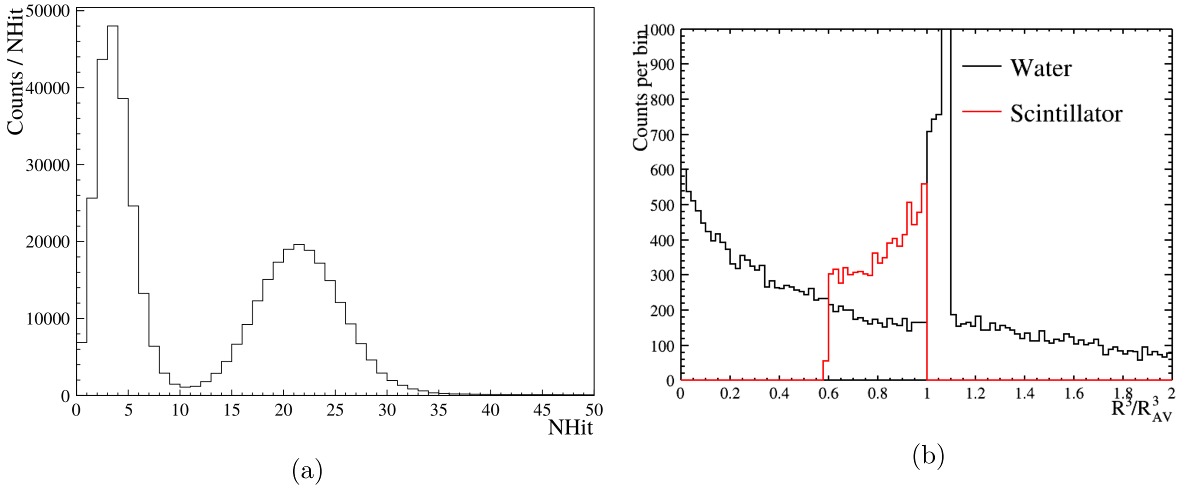

(a) (b)

Figure 3.11: NHit and reconstructed radial distribution of the triggered anticoincidence events from a run in real data taken during the partial fill phase. In (b), events reconstructed in the water are shown in black while events reconstructed in the scintillator are shown in red.

the center of the detector. This is potentially explained by the fact that the hit times of events closer to the edge of the detector are broader in time due to the variation in photon propagation time from the source of the light to each PMT.

During the partial and full scintillator phases, the trigger threshold was set to ∼25 PMT hits. As a result, this trigger was not used because study of the external backgrounds could potentially be performed with the existing trigger by looking at the small fraction of events above ∼25 PMT hits. After the recent addition of bisMSB and corresponding increase in light yield, the trigger threshold has been raised to ∼30 PMT hits further reducing the potential statistics with the existing trigger and increasing the potential utility of this trigger.

3.5 Deadtime and Retriggering

Certain radioactive backgrounds in the SNO+ experiment produce two time correlated events. The ^{214}BiPo decay mentioned in Section 3.4.1 is an example of this. Because the SNO+ trigger system saves data in 420 ns events, coincident radioactive decays with a short enough lifetime or a high enough rate can result in both events occurring within this time window. These events can be a background to the $0\nu\beta\beta$ signal and thus must be tagged and removed from the analysis to maximize

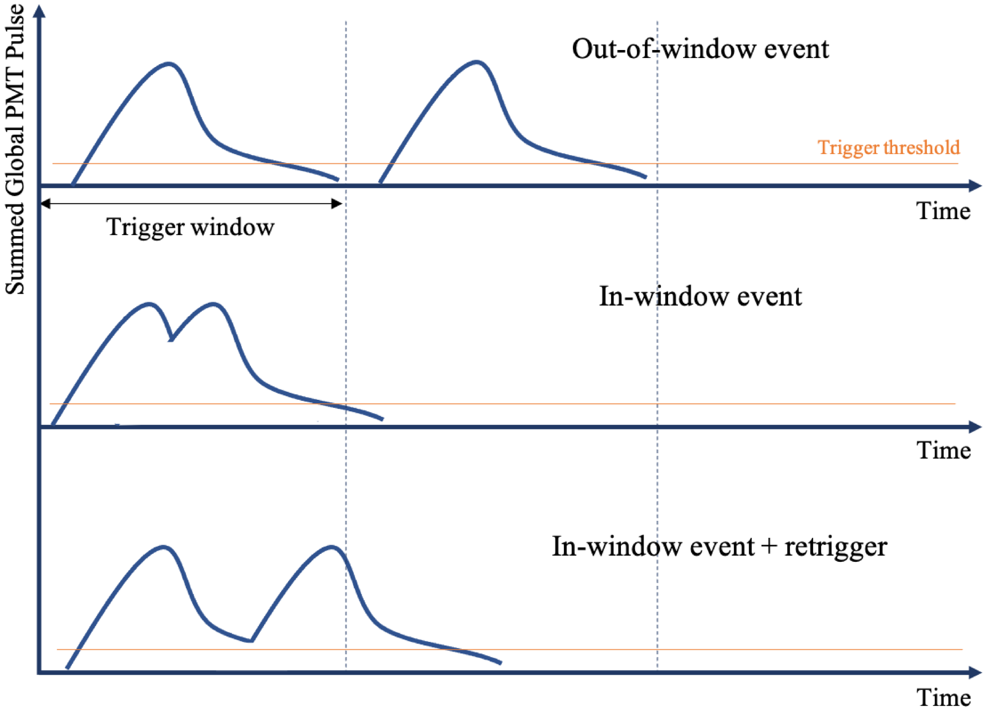

Figure 3.12: Diagram of three cases of triggers. The top shows the second event occurring outside the 420 ns trigger window. The middle shows the second event occurring early within the 420 ns trigger window, allowing most of the light to be captured in one trigger window. The bottom shows the second event occurring near the the end of the 420 ns trigger window, with much of the light occurring in the second trigger window. These diagrams show an idealized case with no deadtime between trigger windows. Figure provided by A.S. Inácio [48].

sensitivity. Reading out the PMT hits of both events is necessary to reject these events. Also, in the case that the delayed event falls just outside the 420 ns event window, a second GT is required to read out the PMT hits of the event. Figure 3.12 shows a diagram of coincident events in the SNO+ trigger. During the analysis of backgrounds to the future $0\nu\beta\beta$ signal search described in Chapter 5, it was determined that a detailed understanding of the deadtime between events was necessary to correctly estimate and maximize the rejection efficiency of these backgrounds. A detailed investigation of the deadtime is presented in this section.

3.5.1 Deadtime

The SNO+ detector typically saves 420 ns events at a rate of ~2kHz. This data then represents ~0.1% of the time the detector is running. However, due to the trigger system, information is still known about what occurred during the other ∼99.9% of the time because any event producing sufficient PMT hits would trigger the detector. Deadtime is defined as any time in which the detector is unable to save or readout events or hits resulting in the information of what occurred during that time period being lost. In the SNO+ trigger system there are generally two types of deadtime:

- Trigger Deadtime: A period of time that is not read out by the detector where a trigger signal is unable to cause a global trigger.
- Hit Deadtime: A period of time where a PMT can be hit but is unable to be read out as part of an event.

Trigger deadtime exists due to the way lockout (LO) is implemented on the MTC/D. In normal physics running, LO is set to 420 ns and no raw trigger signals can create a GT during this time. However, there is a ∼200 ns delay (primarily due to cable lengths) associated with sending the analog trigger signals from the crates to the MTC/A+, the triggering logic on the MTC/A+, and sending the GT back to the crates. This means the hits that cause a GT fall in the middle of the 420 ns trigger window with only ∼220 ns of data saved afterward. As a result, if an event occurs ∼300 ns after the initial event and produces enough hits to create a raw trigger, the event may not trigger the detector because LO has not yet ended. In addition, its hits will not be read out in the initial event. With no GT the information would then be completely lost with no indication that it even occurred.

Hit deadtime exists due to the way the readout on the DBs is implemented. When a PMT is hit, a signal called GTValid is set high and the TAC ramp begins. GTValid is the signal used to indicate that the PMT has a valid hit ready to be read out, while the TAC ramp is used to measure the time since the hit occurred. The length of the TAC ramp must be longer than GTValid to ensure a valid time can be read out for the event while the length of GTValid must be shorter than lockout to prevent the same hit from being read out into two events. As a result, there is a small deadtime between when GTValid ends and when the TAC ramp resets. In addition, GTValid

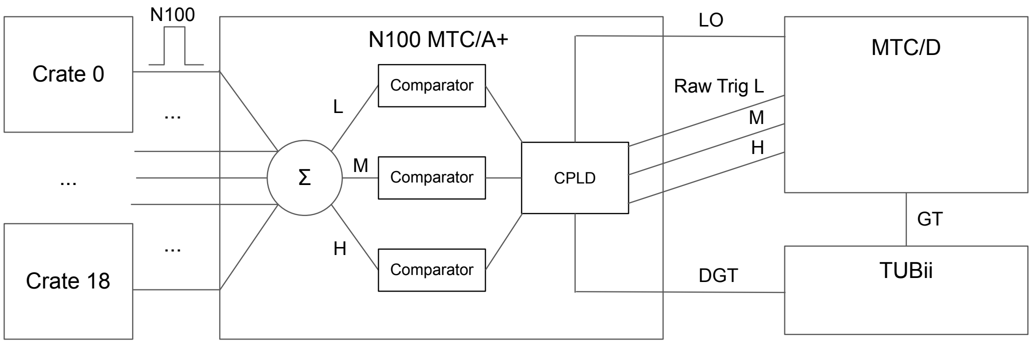

Figure 3.13: Diagram of the signals input to the triggering logic on the MTC/A+.

remains high for the full ∼400 ns after a hit occurs regardless of whether a GT arrives and the channel is read out. This means a channel that is read out $<$ 400 ns after a hit occurs, is dead for the remaining amount of the 400 ns.

The goal of the following tests and updates is to measure the deadtime from these sources, apply strategies to minimize this deadtime, and produce an accurate model of the trigger system and its deadtime in simulation.

3.5.2 Retriggering

The primary strategy used to mitigate deadtime is the use of additional triggering logic implemented on the CPLD on the MTC/A+. After the MTC/D emits a GT, LO prevents another GT from being emitted for 420 ns. The additional logic on the CPLD can be used to emit another trigger immediately at the end of LO based on the conditions during LO. This logic is referred to as "retriggering logic" and the triggers emitted due to this logic are referred to as retriggers.

As mentioned in Section 3.3.3, the CPLD on the MTC/A+ has access to five signals to determine when to trigger the detector: The output of the comparator for each gain path on the MTC/A+, lockout (LO) from the MTC/D or TUBii, and a delayed copy of the global trigger (DGT) produced by TUBii. A diagram of the system is shown in Figure 3.13.

In addition to the standard triggering logic, the retrigger logic was developed to emit retriggers under three conditions:

- Standard Triggers: On the rising edge of the comparator signal a raw trigger is emitted.
- LO Retriggers: If the comparator signal is high at the end of LO, a raw trigger is emitted at the end of LO (i.e. immediately).
- DGT Retriggers: If a rising edge of the comparator signal occurs during LO but after DGT, a raw trigger is emitted at the end of LO.
- Automatic Retriggers: When a raw trigger caused by any of the prior three conditions is emitted, emit another raw trigger at the end of LO.

Each trigger logic condition can be applied independently on each gain path. All three gain paths implement the first three conditions and the low gain path implements all four. This allows the low gain path to be set at a high threshold ensuring retriggers for all events above that threshold. The retriggering logic was designed to be as inclusive as reasonably possible to ensure no events are lost due to trigger deadtime.

The retriggering logic was written in VHDL and implemented in the firmware of the CPLD of the MTC/A+. The logic was then tested on the benchtop using a pulser as an input and in the detector using pedestals before deployment. The pedestal and TELLIE tests, described in Section 3.5.4, were designed to test the deadtime, but also show the expected behavior of the logic.

3.5.3 TUBii Lockout

As mentioned in Section 3.3.3, TUBii creates its own LO signal that can be used to account for the cable delays of the MTC/D LO signal. The length of this LO signal can be varied to ensure that a retrigger on the MTC/A+ arrives at the MTC/D as close to the end of LO as possible to minimize the hit deadtime between trigger and retrigger events. The length was varied and a length of 340 ns was found to produce the minimal deadtime with the retrigger events occurring 460 ns after the initial trigger. Shorter lengths were tested but resulted in unstable data taking.

3.5.4 Deadtime Tests

Two primary tests were performed to characterize the deadtime in the detector before and after applying the deadtime mitigation strategies. The first uses pedestals (the forced triggers described in Section 3.3.4) and the second uses TELLIE (the LED/laser calibration system which will be described in Section 4.3.1).

Pedestal Tests

The first test uses the pedestal signal to probe the deadtime region. TUBii was used to produce two pulses, with a tunable delay between the two. These pulses were sent to the pedestal input for ∼64 channels each on two separate crates. The first pulse causes hits in 64 channels, more than enough to produce a GT. The second pulse then produces 64 additional hits which occur after some delay. These 64 hits should always cause a raw trigger to be sent to the MTC/D but a GT will not be emitted if LO is still active. The delay is then varied and the data is analyzed to determine at what time delays the second set of PMT hits causes a trigger and at what time delays the second set of PMT hits is read out into an event.

Figure 3.14 shows the results of the pedestal test without any of the deadtime mitigation strategies implemented. The pedestal pulses are sent at a rate of 100 Hz and the trigger rate as a function of the delay is shown. A second trigger is not received until the delay reaches 440 ns. This shows significant trigger deadtime. Analysis of the events showed that hits with a delay of ∼225 ns - 440 ns would not get built into an event and are lost indicating ∼200 ns of hit deadtime.

Figure 3.14 also shows the results of the pedestal test with all of the deadtime mitigation strategies implemented. In these tests, the low gain threshold was set to 50 hits and pedestals were sent at 100 Hz. As a result, every event has an automatic retrigger. When the delay is >250 ns an additional trigger occurs due to the DGT triggering logic. This shows that after the implementation of the deadtime mitigation strategies, no trigger deadtime remains. Analysis of the events now shows that the hit deadtime has been reduced to ∼80 ns.

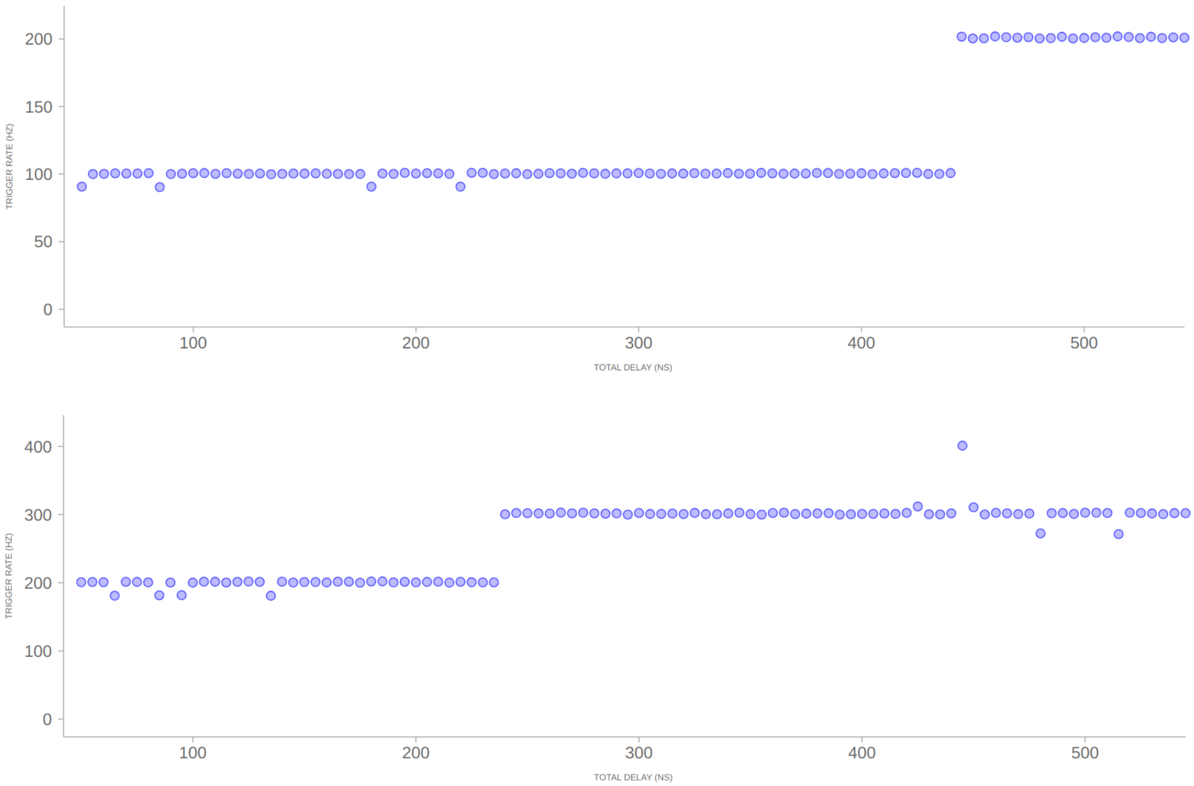

Figure 3.14: Results of the pedestal test with (top) and without (bottom) the deadtime mitigation strategies implemented. Two pedestals are sent at 100 Hz. Prior to the implementation, trigger deadtime and a large hit deadtime were observed. After the implementation, no trigger deadtime and a significant reduction in the hit deadtime was observed.

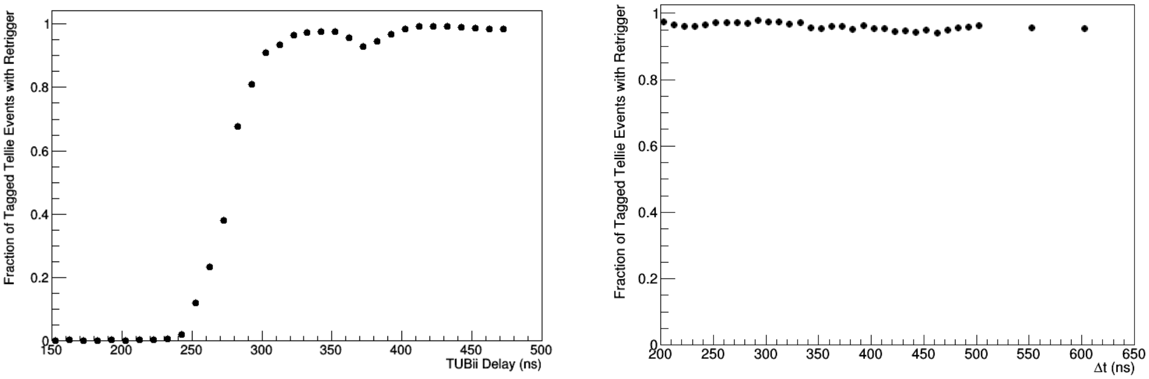

Figure 3.15: Fraction of TELLIE events with a retrigger as a function of delay between pulses. Left shows the initial tests and right shows the tests after the implementation of the deadtime mitigation strategies.

TELLIE Tests

The second test uses light from the LED calibration system to probe the deadtime region. The general strategy is the same as that of the pedestal test except this test uses light produced by TELLIE to create the two sets of PMT hits. In this test, TUBii is again used to produce two pulses with a tunable delay between the two. The pulses are then sent to the LED calibration system producing two pulses of light in the detector which more accurately mimic the expected signals from physics events. This test was also run before and after the implementation of the deadtime mitigation strategies.

The fraction of double pulses that produce two triggers as a function of the delay between pulses is shown in Figure 3.15. Analysis of the initial run showed a slight decrease in deadtime compared to the pedestal test explained by triggers caused by the short timescale variation of the falling edge of the analog trigger signal. Retriggers begin occurring with a delay of 250 ns, and the hit deadtime was observed to be ∼160 ns. Analysis of the final run showed the automatic retriggers occurring at all delays for nearly all events. In addition, the hit deadtime was observed to be reduced to ∼80 ns.

In addition, after all mitigation strategies were applied, the test was run twice with the same delay, first, using LO from the MTC/D, then, using LO from TUBii. Figure 3.17 shows the hit

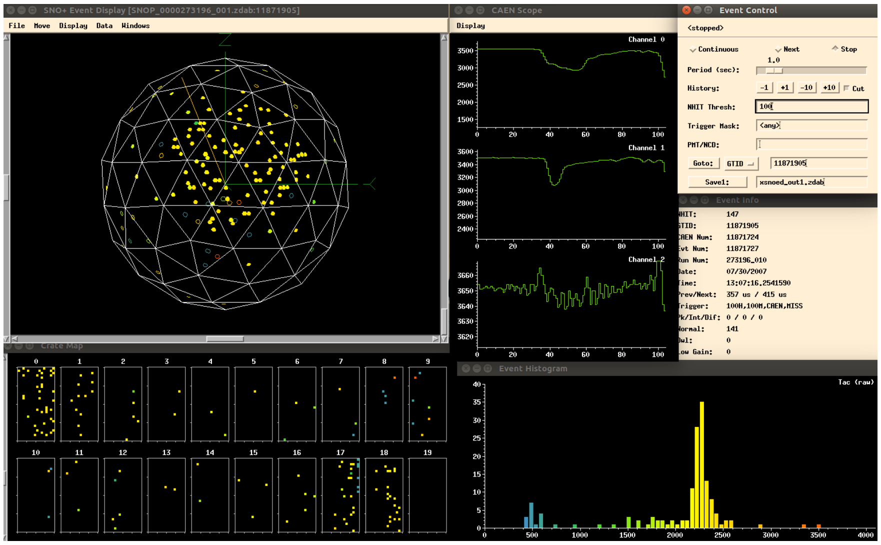

<stopped>

1.0

NHIT Thresh: 100

Trigger Mask: <any>

PMT/NCD:

Goto: GTID 11871905

Save1: xsnoed_out1.zdab

NHIT: 147
GTID: 11871905
CAEN Num: 11871724
vt Num: 11871727
un Num: 273196_010
ate: 07/30/2007
ime: 13:07:16.2541590
rev/Next: 357 us / 415 us
rigger: 100H,100M,CAEN,MISS
k/Int/Dif: 0 / 0 / 0
ormal: 141
wl: 0
ow Gain: 0

Figure 3.16: Example of an event displays of a TELLIE double pulse event where the hits of the second pulse are lost to deadtime. The N100 trigger signal on channel 0 of the CAEN digitizer (top middle window) shows the beginning of the second pulse but only one trigger occurs.

times for the events in this test. The gap in hits at ~500 ns is the hit deadtime between the triggered events. It can be seen that the use of TUBii LO decreases this deadtime from ~160 ns to ~80 ns.

3.5.5 CAEN Digitizer

After the trigger and hit deadtime is minimized, the features of the CAEN digitizer can also be used to provide some information about the remaining hit deadtime between a triggered event and its retrigger. This is because the analog trigger signals are still being produced during this time. The CAEN digitizer readout window can thus be extended into the deadtime region to read out the analog trigger signal during this time. This trigger signal should be sufficient information to determine if an event producing many PMT hits occurred during the deadtime region allowing its removal from analysis. Figure 3.18 shows an example CAEN trace of a coincidence event in which the delayed event falls into the deadtime but could be identified by the CAEN.

3.5.6 Trigger Model Updates

Prior to the described deadtime tests, the trigger model used in simulation was observed to disagree with data. An overhaul of the model taking into account all three new retriggering logic condi-

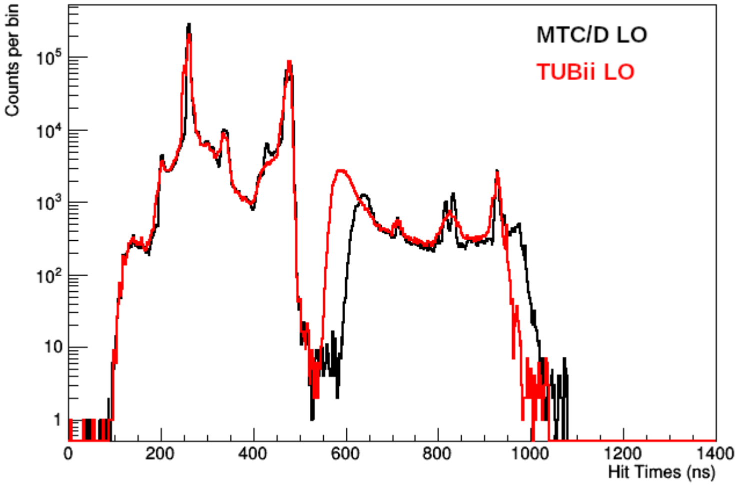

Figure 3.17: Two TELLIE test runs taken with the same settings except for the source of LO. Hits in the second trigger window start being read out ~80 ns earlier when using TUBii LO indicating a ~80 ns reduction in the hit deadtime for retrigger events.

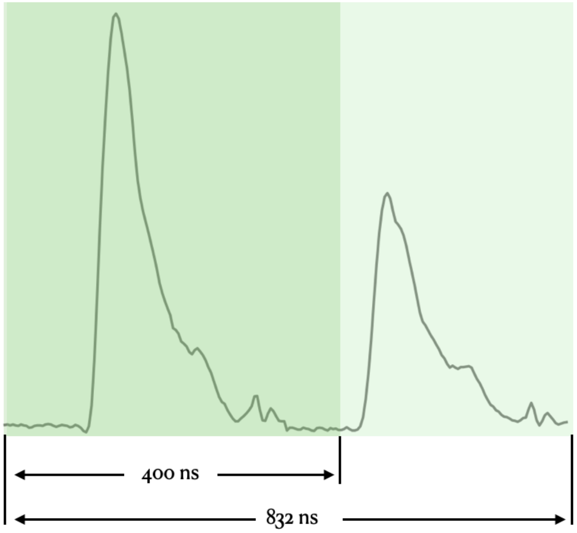

Figure 3.18: An example of a coincidence event in which the delayed event falls into the deadtime but could be identified by the CAEN. The plot shows the CAEN trace extended into the deadtime window. A clear second peak is observed in the CAEN trace. Figure provided by S. Yang [67].

tions, TUBii LO, and DGT was developed. The various timings and delays of the trigger system were calibrated using the pedestal and TELLIE deadtime tests described above. Testing showed significant improvement in agreement between simulation and data.

3.5.7 Results

This section detailed new retriggering logic and hardware functionality to account for cable delays and reduce the deadtime in the detector. The deadtime was measured using multiple sources and a model was developed using the results of these tests. Trigger deadtime in the detector was completely eliminated while the hit deadtime between events was reduced by $\sim$50%. With the addition of the extended CAEN digitizer window, all potential deadtime in the detector will be covered by these improvements. These improvements ensure that the required rejection efficiency of certain coincident events at $>$99% efficiency for the $0\nu\beta\beta$ analysis will not be limited by the trigger system.

Chapter 4

SIMULATION, RECONSTRUCTION, AND CALIBRATION IN SNO+

Interpretation of data from the SNO+ detector requires several steps between data taking and analysis. Detailed simulations are required to predict signal rates and estimate signal efficiencies. Reconstruction of detected events is required to infer their properties such as the energy deposited and the position they occurred at. Calibration is then required to verify that the simulation correctly reproduces the observed data. These steps are described in the following chapter.

4.1 Simulation

The primary simulation and analysis tool used by SNO+ is called `RAT` (Reactor Analysis Tool) [68]. `RAT` is a software package originally developed by S. Seibert for the Braidwood Collaboration. `RAT` is written in `C++` , and built using the `GEANT-4` [69] and `ROOT` [70] packages.

The SNO+ experiment has developed a detailed model of the SNO+ detector, PMTs, and electronics that is incorporated into `RAT` . A dedicated database, RATDB, is used to store various information about the material properties of the detector such as the physical geometry, optical properties, PMT efficiencies, etc. In addition, this database stores run-by-run information describing the settings of the detector hardware and DAQ systems to accurately reproduce detector conditions in all simulations.

`RAT` is capable of producing a variety of different types of physical processes with many different settings to control the position, energy, direction, and other properties of the simulated events. Dedicated event generators have been developed by the SNO+ collaboration to simulate the most commonly studied types of events in the detector. This includes reactor neutrinos, solar neutrinos, various radioactive decays, and all of the calibration sources used in the detector.

After an event is generated by `RAT` , `GEANT-4` handles the propagation and interactions of the generated particles and their daughter particles through the model of the SNO+ detector. `GEANT-4` includes and simulates a complete set of physics processes for interactions of particles in matter over a large range of energies. `GEANT-4` handles these interactions up until the point that an optical photon reaches a PMT. At this point, the interaction of the optical photon is handled by `RAT` . `RAT` contains a model of the PMT which determines if a photoelectron is produced based on the point of contact, incident angle, and wavelength.

After photoelectrons are produced, a simulated PMT pulse is created for each photoelectron. These simulated PMT pulses are then input to a full simulation of the trigger system to determine whether the event would result in a trigger. If so, the event is saved in simulation with all the same information that is saved in a real event in data. Simulated files also contain additional information on the simulated events such as the generated energy, position, and direction of the simulated particles and other "MC Truth" information describing the true simulated values of these parameters. Events simulated in `RAT` are output and saved in the same format as real data, a custom `ROOT` file. This allows the same reconstruction and analysis methods to be applied to both simulation and data.

4.2 Reconstruction

When events are detected or simulated, a specific set of data is saved: the time of the trigger, each PMT that is hit, the time each PMT was hit relative to the trigger time, and the amount of charge detected by each PMT. For each event, this set of data must be used to infer the physical properties of the event itself. This process is referred to as reconstruction. The most important quantities obtained in scintillator phase through reconstruction are the position and energy of the event. Additional information, such as the precise time that the event occurred, the direction of the event, or information about the physical process that caused the event is also reconstructed.

The SNO+ collaboration has developed detailed algorithms to reconstruct these properties. The optimal methods are applied to all events and are described in more detail in the following section.

4.2.1 Position & Time

The first values to be reconstructed are the position and precise time of the event. These two values are reconstructed simultaneously using the "hit time residuals" defined as:

$$t_{\text{res}} = t_{\text{hit}} - t_{\text{fit}} - t_{\text{tof}} \tag{4.1}$$

where t_{res} is the hit time residual, t_{hit} is the time when the PMT was hit, t_{fit} is the reconstructed time that the event occurred, and t_{tof} is the time of flight from a given reconstructed position to the position of the hit PMT. Under ideal conditions (e.g. no optical effects, perfect time resolution for PMT hits, etc.), when the position and time are correctly chosen, the hit time residual distribution will match the photon emission time profile. The photon emission time profile obtained from the SNO+ scintillator is shown in Figure 4.1.

The fitting algorithm then performs a likelihood fit of the hit time residual distribution to the

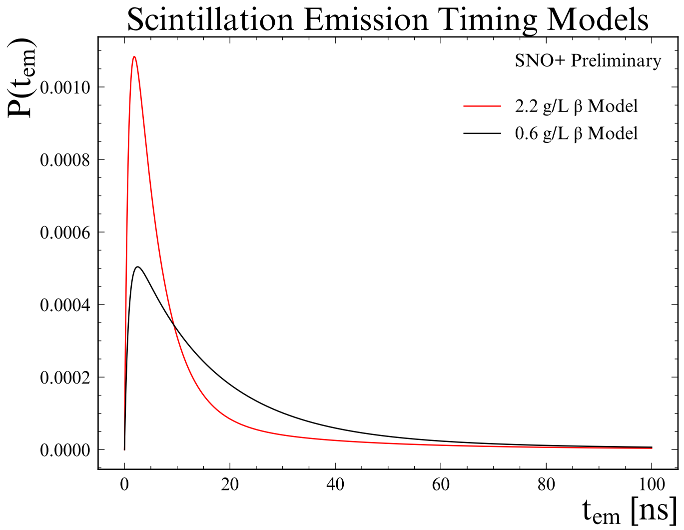

Figure 4.1: Scintillator emission time profile as modeled in `RAT` . Models for both full fill (2.2 g/L β Model) and partial fill (0.6 g/L β Model) are shown. Figure provided by R. Hunt-Stokes [71].

scintillator emission time profile with the likelihood defined as:

$$\log \mathcal{L} = \sum_{i=0}^{N_{\text{hits}}} \log P(t^i_{\text{res}}) \tag{4.2}$$

where $P(t^i_{\text{res}})$ is the probability of a hit having time residual t_{res} and N_{hits} is the total number of PMTs hit in the event. The algorithm varies the hypothesized position and time of the event to maximize $\log \mathcal{L}$, returning the best fit parameters. The resulting position obtained from this fit has been demonstrated to have a resolution of $\sim$15 cm with biases < 2 cm in simulation.

4.2.2 Energy

The next reconstructed quantity is the energy of the event. All events are reconstructed under the hypothesis of a single electron. As a result, particles that are quenched (e.g. αs) will have reconstructed energies smaller than their actual energies due to quenching (e.g. $\sim$10× smaller for αs). The energy reconstruction is of particular importance to the following analysis of reactor antineutrinos as the survival probability is dependent on the energy of the event.

As seen in Chapter 3 the light emitted by a particle in scintillator and therefore the number of detected photoelectrons is approximately linear with energy. However, the SNO+ electronics can only record one hit per PMT per event. In addition, the charge resolution of the PMTs is not sufficient to distinguish between a single p.e. and a few p.e. As a result, the relationship between PMT Hits and energy becomes nonlinear as the probability of a PMT receiving multiple hits increases.

The first step of the energy reconstruction is then to obtain a value that is linear with energy. This is done by dividing the detector into segments of PMTs with approximately equal hit probability. The value is defined as:

$$H = -\sum_{i=1}^{S} N^i_{PMT} \log\left(1 - \frac{N^i_{Hits}}{N^i_{PMT}}\right) \tag{4.3}$$

where S is the number of segments, N^i_{PMT} is the number of PMTs in the segment, and N^i_{Hits} is the number of hit PMTs in the segment.

This segmentation uses groups of similar PMTs to estimate the hit probability of all the PMTs in the group. The probability of the PMTs being hit is then converted to the average number of p.e. per channel before being multiplied by the number of PMTs to obtain the linear H parameter. The H parameter is effectively an estimate of the number of detected p.e which is proportional to energy. Simulation can then be used to find the constant of proportionality and calibration sources can then be used to verify the conversion.

Many of the effects that affect the constant of proportionality are position dependent. For example, optical effects such as absorption, and scattering depend on the path length of the photons. In addition, total internal reflection can occur for events near the AV surface and the efficiency of each PMT depends on the angle of incidence of the photon. These effects are modeled in simulation and a correction is produced as a function of radius r and polar angle θ. This function takes advantage of the azimuthal symmetry of the SNO+ detector and is shown in Figure 4.2.

Prior to the calibration described in Section 4.3.6, the fractional energy resolution in MC is

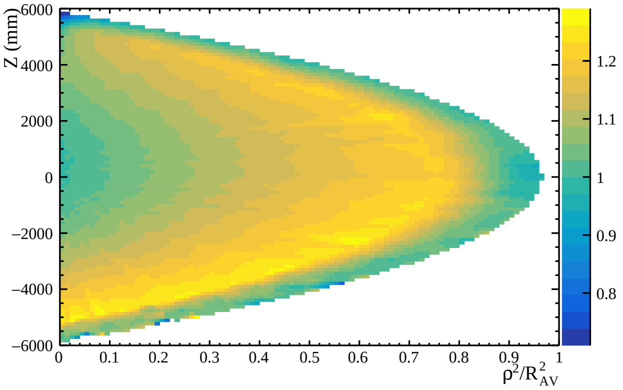

Figure 4.2: Scaling between each position in the detector and the center as a function of z vs. $\rho = x^2 + y^2$ used in energy reconstruction.

found to be ∼4%, and the fractional energy bias is found to be <1% for 2.5 MeV electrons near the center of the detector.

4.2.3 Direction

Two types of light are emitted in interactions in the SNO+ detector, Cherenkov and scintillation light. The scintillation light is isotropic and thus does not provide any information regarding the direction of the event. The Cherenkov light, however, is directional and is emitted in a cone in the direction of travel of the particle.

In the water phase of SNO+, only Cherenkov light is created, and thus reconstruction of the direction is fairly straightforward. However, in the scintillator phase of SNO+, the amount of scintillation light is ∼50× larger than the amount of Cherenkov light. This requires more sophisticated methods in order to separate the scintillation and Cherenkov light to recover the directional information. In fact, SNO+ is the first large-scale liquid scintillator experiment to demonstrate event-by-event direction reconstruction [59], however, this direction reconstruction is not used in the following analysis.

4.2.4 Classifiers

In addition to the reconstruction of the continuous values of the properties of events such as position and energy, the PMT hit data can be used to measure other properties of the event.

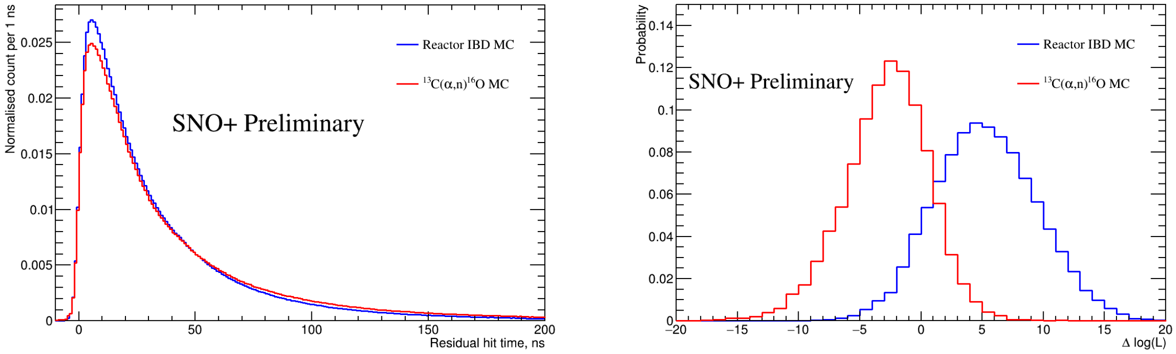

Figure 4.3: Performance of the IBD classifier in simulation. The hit time residuals for both the reactor IBD and α-n MC are shown on the left, while the resulting likelihood ratios for both the reactor IBD and α-n MC are shown on the right. Figures provided by C. Mills [58].

For example, the data can be used to distinguish between different physical processes that create events or general properties of the PMT hits can be calculated to characterize the event. These algorithms are referred to as "Classifiers". A few classifiers are of particular importance for the analyses described in the following chapters.

α-n - IBD Classifier

The classifier most relevant to the analysis of reactor antineutrinos is the α-n - IBD Classifier. As the name implies, this classifier is designed to distinguish between the prompt event of an α-n event which is produced by proton recoils and the prompt event of an inverse beta decay event which is produced by a positron which deposits its energy and then annihilates, emitting two 511 keV γs.

This classifier works by using the observed hit time residual distribution to perform a likelihood ratio test between the expected distributions for α-n and IBD events. Figure 4.3 shows the expected hit time residual distributions for α-n and IBD events as well as the output likelihood distributions from MC. An optimized cut on this likelihood ratio removes 70% of α-n events while retaining 93% of IBD events.

$\alpha - \beta$ Classifier

Another classifier used in the following analyses is referred to as the "$\alpha - \beta$ Classifier". This classifier is designed to distinguish between $0\nu\beta\beta$ events and radioactive decays of ^{214}BiPo and ^{212}BiPo. The

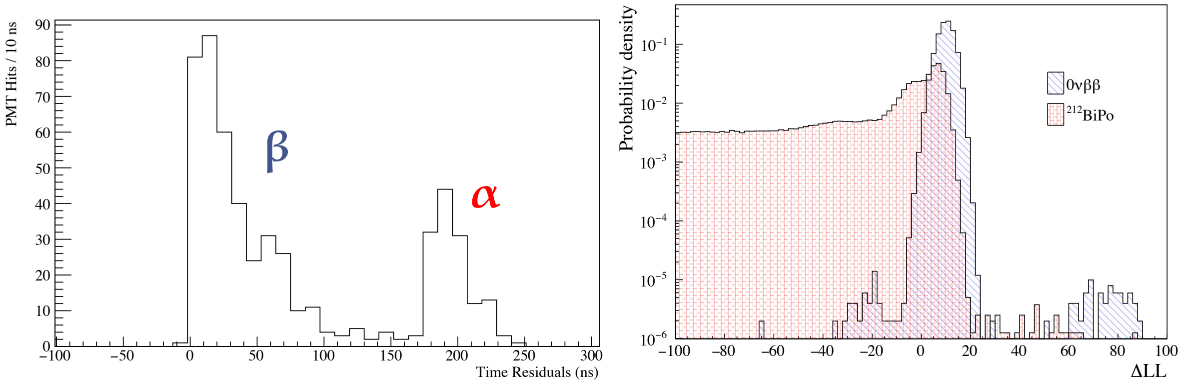

Figure 4.4: The left plot shows an example of the hit time residuals of an event tagged as a ^{212}BiPo by the $\alpha-\beta$ Classifier. The right plot shows the likelihood ratio distributions of $0\nu\beta\beta$ and ^{212}BiPo. Figures provided by M. Luo [72].

$0\nu\beta\beta$ event consists of two electrons produced with a total energy of 2.5 MeV. ^{214}BiPo/^{212}BiPo decays consist of a β decay with Q value of 3.3/2.3 MeV followed by an α decay with energy of 7.8/9.0 MeV with a lifetime of 237/0.43 μs. Because of the short lifetime of these decays, it is possible for both decays to occur within the same 420 ns event window producing two peaks in the hit time residual distribution. Figure 4.4 shows an example of the hit time residuals for a tagged double peak ^{212}BiPo pileup event.

This classifier works by using the observed hit time residual distribution to perform a likelihood ratio test between the expected distributions for $0\nu\beta\beta$ and $^{214/212}$BiPo pileup events. Figure 4.4 also shows the output likelihood distributions from a sample of simulated events during the partial fill phase data used in the analysis described in Chapter 5. A clear separation is seen between ^{212}BiPo events and $0\nu\beta\beta$ events.

4.3 Calibration

In order to draw reliable conclusions from the data, each step in the process of obtaining the physical properties of detected events must be calibrated. In general, this is done by producing data using a well understood signal with known physical properties, then ensuring that the physical properties inferred in both data and simulation are correct. The various calibrations and sources used to perform these calibrations are described in this section.

Source	Particle Type	Energy (MeV)	Calibrated Quantity
AmBe	n,γ	2.2, 4.4	Neutron Capture Response
^{8}Li	Optical Photons	-	Cherenkov Light Response
^{16}N	γ	6.1	Energy Reconstruction
^{46}Sc	$\gamma \times 2$	2.0 (1.1 + 0.9)	Energy Reconstruction
^{48}Sc	$\gamma \times 3$	3.3 (1.3 + 1.0 + 1.0)	Energy Reconstruction
^{57}Co	γ	0.1	Energy Reconstruction
^{137}Cs	γ	0.7	Energy Reconstruction

Table 4.1: Radioactive calibration sources that have been deployed or are in preparation for the SNO+ experiment. Sources with multiple signals in coincidence give the total energy with the individual energies in parenthesis.

4.3.1 Calibration Sources

Radioactive Sources

Calibration sources containing known radioactive materials can be used to provide a well understood signal produced in a known location. Table 4.1 lists the radioactive sources that have been deployed or are in preparation for deployment in the SNO+ experiment. These sources cover a range of energies relevant to the majority of planned physics analyses in SNO+. The AmBe, ^{8}Li, and ^{16}N sources were deployed during the water phase while the AmBe and ^{16}N sources have been deployed in the external water near the AV during the scintillator phase. A rope system is used to deploy and control the position of each source in the detector.

The ^{16}N source was inherited from SNO [73] and was the primary calibration source used in the water phase. It is planned to only be deployed outside the AV in the scintillator phase due to the risk of contamination. ^{16}N is produced near the detector and transported via a small tube into a decay chamber. The ^{16}N then primarily decays via an electron to ^{16}O* which promptly deexcites via a 6.1 MeV γ. The electron is detected by a PMT within the source encapsulation allowing the decay to be tagged while the 6.1 MeV γ escapes the encapsulation and is detected and used for calibration.

The AmBe source was also inherited from SNO and has been used in the water phase to calibrate the neutron response [51]. It has also only been deployed outside the AV in the scintillator phase due to the risk of contamination. The source contains a mixture of powdered ^{241}Am and ^{9}Be encapsulated in a stainless steel container. The ^{241}Am primarily decays via an α followed by a prompt 59.5 keV deexcitation γ. The α is captured by the ^{9}Be (with $\mathcal{O}(10^{-4})$ efficiency), producing a neutron and ^{12}C. ~60% of the time, the neutron is produced with little kinetic energy and the ^{12}C is produced in an excited state, promptly deexciting via a 4.4 MeV γ. The other ~40% of the time, the emitted neutron carries significant kinetic energy and scatters protons which create scintillation light. In both cases, the neutron thermalizes and captures on hydrogen with a lifetime of ~200 μs, producing a 2.2 MeV γ. The 4.4 MeV γ, 2.2 MeV neutron capture γ, and proton recoil signals can all be used for calibration.

The AmBe source is of particular interest for the analysis of reactor antineutrinos described in Chapters 6-9. This is because the signal produced by antineutrinos is a coincidence of a positron and a 2.2 MeV neutron capture γ. In addition, the primary background to this analysis is a similar α-n process but with α capture on ^{13}C rather than ^{9}Be. Calibration using data obtained with the AmBe source is still ongoing.

In addition to the deployed radioactive sources, intrinsic radioactivity within the AV can also be used as a calibration source. Several radioactive decays studied by SNO+ collaborators include ^{210}Po α decays, ^{214}BiPo β-α coincidence decays, ^{212}BiPo β-α coincidence decays, and ^{14}C β decays. These backgrounds provide continuous calibration sources allowing monitoring of the energy reconstruction, and optical properties of the detector as a function of time.

Optical Sources

Two optical calibration sources are used by the SNO+ collaboration. These systems use LEDs or lasers to inject light with a fixed wavelength into the detector. This allows calibration of the optical properties of the detector medium and the PMT response as a function of wavelength. In addition, the timing of the light injection is known and the trigger system allows for calibration sources to trigger the detector asynchronously, allowing calibration of the PMT timing delays.

The first optical calibration source is the laserball. The laserball was originally designed for the SNO experiment [74] and redeveloped for SNO+ to satisfy the increased purity requirements during the scintillator phase [45]. It consists of an 11 cm diameter light-diffusing sphere which is connected to a nitrogen dye laser via an optical fiber. A variety of dyes allow the light to be produced at a range of different wavelengths from ∼300-500 nm. The sphere contains hollow glass beads suspended in silicone gel which diffuse the light injected into the sphere to produce an approximately isotropic light source.

The other optical calibration source is the Embedded LED/Laser Light Injection Entity (ELLIE) [45]. The ELLIE system was developed for SNO+ to eliminate the risk of contamination associated with deploying instrumentation into the detector. The ELLIE system consists of optical fibers permanently mounted on the PSUP which inject light produced by LEDs or lasers. ELLIE consists of three modules. The Timing Module (TELLIE) measures the timing and gain of the PMTs and consists of ∼100 optical fibers coupled to LEDs and mounted across many positions in the detector. The beam produced by each TELLIE fiber has a wide angle to cover as many PMTs as possible. The Scattering Module (SMELLIE) measures scattering in the detector and consists of ∼15 optical fibers which can be coupled to one of several lasers. These lasers produce a narrow beam at several wavelengths between 375 and 700 nm. Finally, the Attenuation Module (AMELLIE) measures the attenuation length in the detector using LEDs at several different wavelengths coupled to ∼10 optical fibers.

4.3.2 Electronics Calibration

The calibration of the data begins with the electronics responsible for converting the PMT pulses into the time and charge observed by each PMT. The two types of electronics calibrations performed in SNO+ were described in detail in Section 3.3.4.

4.3.3 PMT Calibration

Next, the response of the PMTs must be calibrated using an optical source. This calibration is referred to as a PCA (PMT Calibration) and can be done with either the deployed laserball source or with the TELLIE calibration system. During a PCA run, the light source is tuned to provide signals primarily from single p.e. A large sample of single p.e. data is taken for each channel and used primarily to calibrate three things:

- PMT gain: The peak in the measured charge distribution for each PMT.
- Channel-to-channel time delays: The time difference between hits occurring on different channels at the same time.
- Time-walk effect: The relationship between measured charge and time. Larger PMT pulses will have a faster risetime and thus trigger earlier than smaller pulses.

4.3.4 Optical Calibration

The optical properties of the detector media (scintillator, acrylic, water, etc.) must be calibrated to accurately reproduce data. This includes the absorption and scattering of each material as a function of wavelength. In addition, the angular response and relative efficiencies of each PMT are obtained in the optical analysis. In water phase this was performed using the laserball [49], but in scintillator phase, it will be performed using the ELLIE LED/laser calibration systems.

In this calibration, light of a specific wavelength is injected into the detector from several different positions. The occupancy of each PMT in data and in corresponding simulations are then compared. The angular response and relative efficiencies of the PMTs as well as the optical parameters of each material are then optimized to maximize the agreement between data and simulation.

4.3.5 Scintillator Timing Calibration

The timing of light emission by particles depositing their energy in the scintillator must also be calibrated. The scintillator emission profile is modeled in simulation as the sum of several exponential decay terms with a rise time. The model is parameterized by a decay constant and amplitude for each term as well as a single rise time parameter.

The calibration of this model has been performed in the SNO+ scintillator phase using βs and αs from tagged ^{214}BiPo decays. The hit time residual distribution for the tagged events in data is compared to the corresponding hit time residual distribution in simulation. The parameters in the

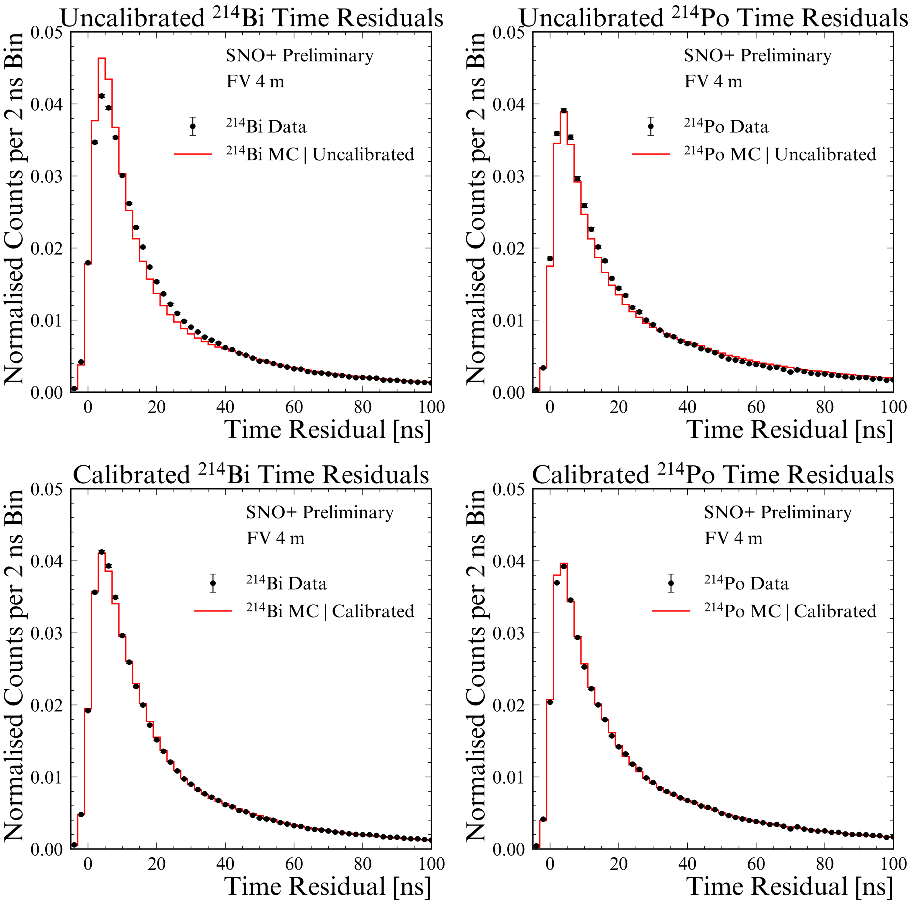

Figure 4.5: Comparison between data and simulation of the time residual distributions for tagged events. Results are shown for tagged ^{214}Bi β decays and tagged ^{214}Po α decays both before and after the calibration. Plots provided by R. Hunt-Stokes [71].

scintillator model are then optimized to find the best agreement between data and simulation. The results of the timing calibration for both the ^{214}Bi β decay and the ^{214}Po α are shown in Figure 4.5. Additional work is ongoing to calibrate the timing of proton recoil events using a similar method applied to the AmBe calibration source.

4.3.6 Energy Calibration using Intrinsic Radioactivity in SNO+

The final calibration discussed in this chapter is a calibration of the energy reconstruction using intrinsic radioactivity in the SNO+ detector. A full calibration of the reconstructed energy using the previously mentioned radioactive sources was not completed at the time of this analysis. As a result, intrinsic radioactivity was used to both calibrate the energy response across the detector

Cut	Prompt Event	Delayed Event
Valid Fit	True	True
Data Cleaning	Pass	Pass
Radius	R $<$ 6.0 m	R $<$ 6.0 m
Energy	1.2 $<$ E $<$ 3.5 MeV	0.6 $<$ E $<$ 1.1 MeV
Δt	2 $<$ Δt $<$ 1000 μs	
Δr	Δr $<$ 0.8 m	

Table 4.2: Selection criteria used to tag ^{214}BiPo events.

and estimate systematic uncertainties used in the analysis of reactor antineutrinos described in Chapters 6-8.

This calibration uses the coincidence of ^{214}BiPo decays as a calibration source. As mentioned in previous sections, ^{214}BiPo decays consist of two time correlated events. The first event, ^{214}Bi decay, is a β decay with a Q value of 3.27 MeV. The second event, ^{214}Po decay, occurs in the same location, has a lifetime of 237 μs, and decays via a 7.83 MeV α. Due to quenching, this α reconstructs at ~0.8 MeV.

The coincidence of these two events in both time and space provides a distinct signal that is nearly background free which allows a direct comparison of simulated ^{214}Bi β decays and ^{214}Po α decays to data for calibration. The selection criteria used to tag ^{214}BiPo events are summarized in Table 4.2. The time difference between the tagged ^{214}Bi and ^{214}Po events can be fit with a falling exponential distribution plus a flat background ($A \times e^{-t/\tau} + B$). This distribution is shown in Figure 4.6. The fitted lifetime $\tau = 238.6 \pm 2.0$ μs is in good agreement with the known ^{214}Po lifetime of 237 μs and the fitted constant $B = 2.4 \pm 2.9$ is consistent with 0 indicating a pure sample of ^{214}BiPo events.

Applying this set of selection criteria to data produces a sample of ~60,000 tagged ^{214}BiPo decays to use for this calibration. Figure 4.7 shows the reconstructed energy distributions of a sample of tagged ^{214}Bi events in the center of the detector (R $<$ 3.5m) along with a corresponding sample of simulated ^{214}Bi events. As a result of the previously mentioned calibrations being performed using events near the center of the detector, the agreement is quite good. However, Figure 4.7 also

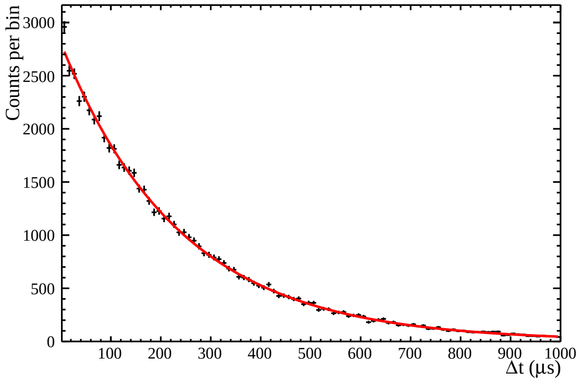

Figure 4.6: Fitted ^{214}Po decay time. The fit agrees well with a pure sample of tagged ^{214}BiPo decays.

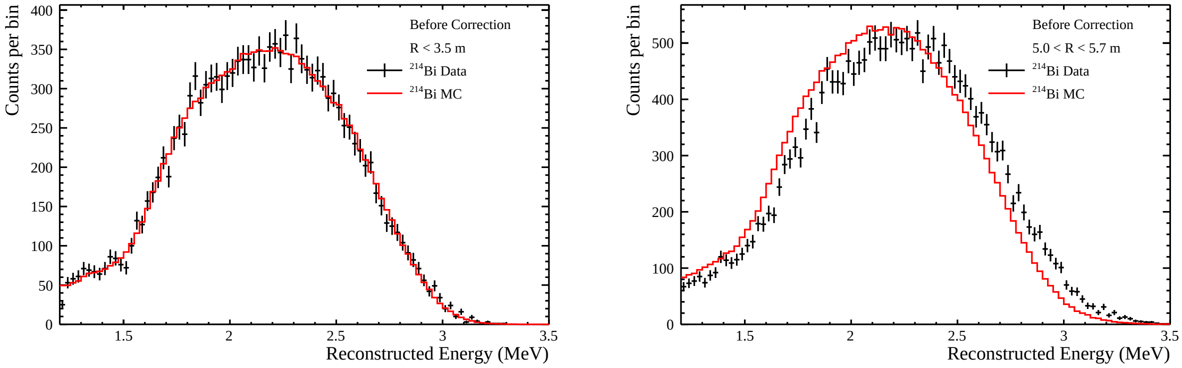

Figure 4.7: Comparisons of the energy distributions of tagged ^{214}Bi between data and simulation before application of the correction function. The left plot shows good agreement in the center of the detector while the right plot shows discrepancies between data and MC at higher radius.

shows the agreement between data and simulation at higher radius (5.0 m $<$ R $<$ 5.7 m) which is significantly poorer. The primary goal of this calibration is to improve the agreement between data and simulation at higher radius to allow the use of a larger fiducial volume.

The first step of this calibration is to perform a Gaussian fit to the energy distribution of ^{214}Bi events at the center of the detector (R $<$ 3.3 m) in data. This gives a mean fitted energy of 2.20 MeV for ^{214}Bi events. The detector is then segmented into bins in z vs. ρ^2 taking advantage of the azimuthal symmetry of the detector. The binning is chosen such that each bin is approximately equal in volume and contains ~1000 tagged ^{214}BiPo events in data for use in the calibration. The

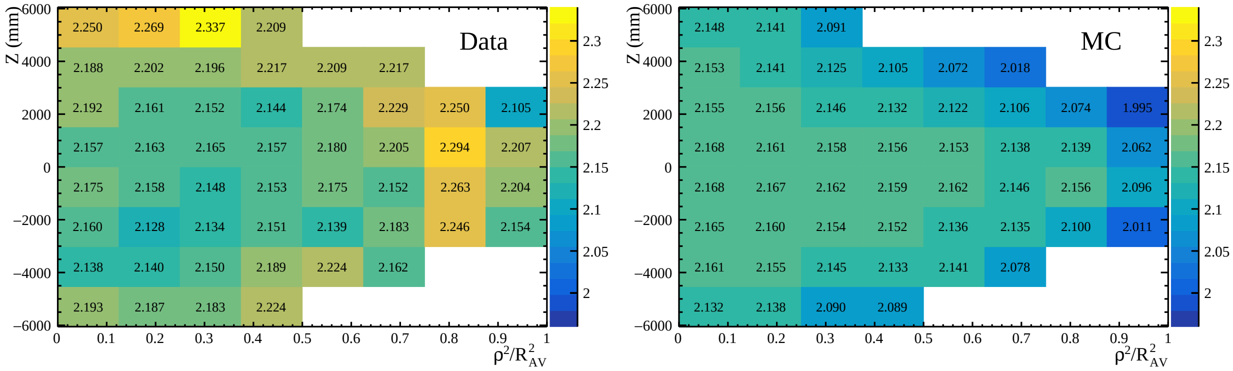

Figure 4.8: Fitted mean energies of tagged ^{214}BiPo events as a function of z vs. ρ^2 in both data and simulation.

same Gaussian fit is performed on each sample of tagged ^{214}BiPo events in both data and simulation to obtain the maps of mean energies at each position in the detector shown in Figure 4.8.

These maps are then converted to an energy non-uniformity correction function by taking the ratio of the fitted mean in the center of the detector (2.2 MeV from data with R $<$ 3.3 m) to the fitted mean in each bin. A bi-linear interpolation function is then used to interpolate the value of the function between bins to provide a continuous correction function. Two separate correction functions are produced, one to be applied to data and one to be applied to simulation. This is done to both improve the agreement between data and simulation and the agreement between events at the edge of the detector and the center. Figure 4.9 shows the correction function for both data and simulation.

Figure 4.10 shows the effect of the function in several pairs of plots. The first set of plots shows the agreement between data and simulation at high radius (5 $<$ R $<$ 5.7 m) before and after application of the correction function. The second set of plots shows the agreement between data in the center (R $<$ 3.3 m) and data near the edge (5.0 $<$ R $<$ 5.7 m) of the detector before and after application of the correction function. Both sets of plots show improvement in the agreement between data sets as desired. In addition, Figure 4.11 shows the results of the application of the correction function to data collected using the AmBe calibration source. The 2.2 and 4.4 MeV γ peaks can be seen. The source was positioned just outside the AV. As a result, the events are

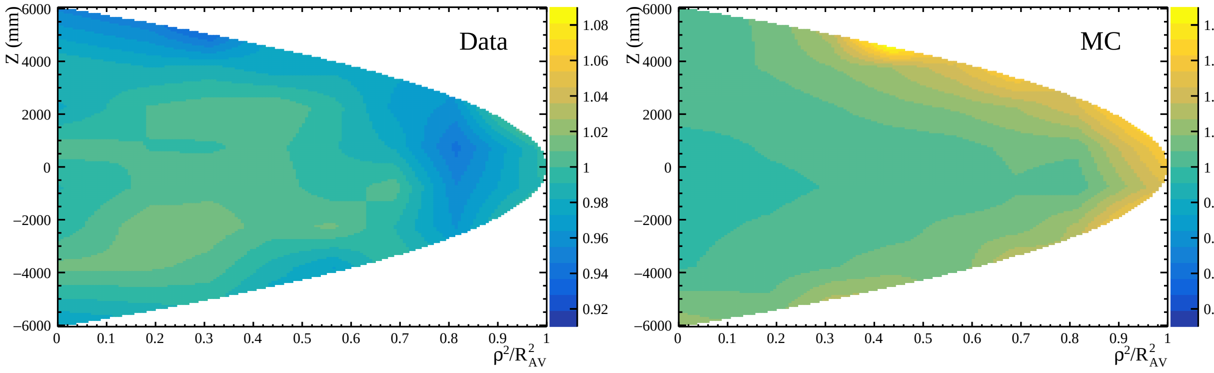

Figure 4.9: The residual energy correction as a function of position in the detector for both data (left) and MC (right).

predominantly located near the AV, the location with the largest disagreement between data and simulation prior to this calibration.

Now having shown that the correction function improves the agreement between data and simulation, the systematic uncertainties on the energy scale and energy resolution are estimated. First, the sample of tagged ^{214}BiPos is binned in $\mathrm{R}^3/\mathrm{R}^3_{\mathrm{AV}}$ which provides equal volume bins. The energy distributions for both data and simulation are fitted with a Gaussian and the ratio of their means are shown as a function of $\mathrm{R}^3/\mathrm{R}^3_{\mathrm{AV}}$ in Figure 4.12. The error in each bin is taken to be $\sigma = \sqrt{(1-\mu_{\mathrm{Data}}/\mu_{MC})^2 + \sigma^2_{\mathrm{stat}}}$. The RMS of the bin-by-bin errors is found to be 1.8%. The blue shaded areas in Figure 4.12 show the 1.8% systematic bands on the energy scale for both the tagged ^{214}Bi and ^{214}Po events. It can be seen that the systematic uncertainty covers the discrepancies between data and simulation for both decays.

Next, the fitted σ of the tagged ^{214}Bi events are used to estimate the systematic uncertainty on the energy resolution. Figure 4.12 shows the fitted σ as a function of $\mathrm{R}^3/\mathrm{R}^3_{\mathrm{AV}}$. The error in each bin is taken to be $\sigma = \sqrt{\mathrm{abs}(\sigma^2_{\mathrm{Data}} - \sigma^2_{MC}) + \sigma^2_{\mathrm{stat}}}$. The RMS of the bin-by-bin errors is found to be 6.5% at the energy of the 2.2 MeV ^{214}Bi decay. This uncertainty is assumed to scale with $\sqrt{E}$ which gives a systematic uncertainty of $4.4\%\times\sqrt{E}$. The blue shaded areas in Figure 4.12 show the $4.4\%\times\sqrt{E}$ systematic bands on the energy resolution for both the tagged ^{214}Bi and ^{214}Po events. Again, it can be seen that the systematic uncertainty covers the discrepancies between simulation

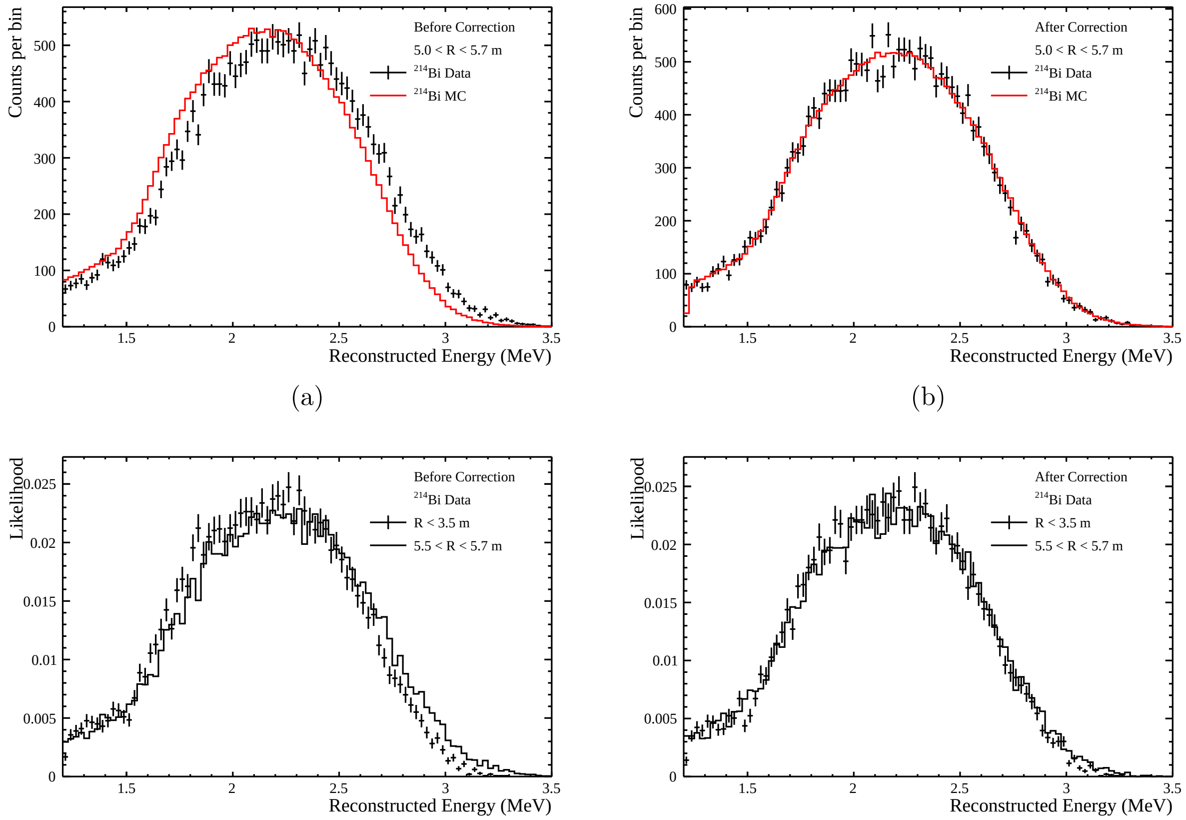

(a) (b)

(c) (d)

Figure 4.10: Results of applying the residual energy correction function to data and MC. (a) and (b) show the agreement between data and MC while (c) and (d) show the agreement between the center and edge of the dectector in data. Both show improved agreement when the correction is applied.

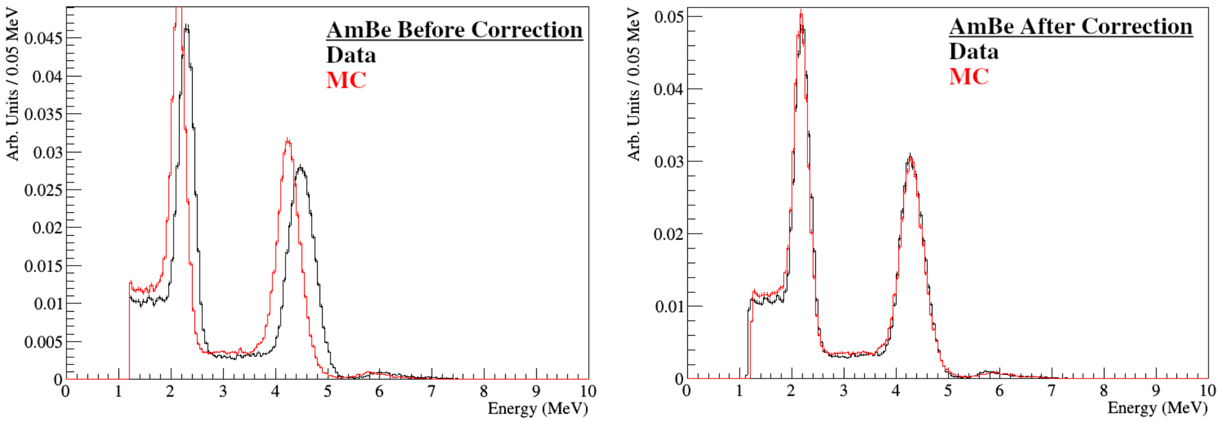

Figure 4.11: Results of applying the residual energy correction function to the AmBe calibration source. The agreement between data and MC is greatly improved. These figures were provided by T. Kaptanoglu.

and data for both decays.

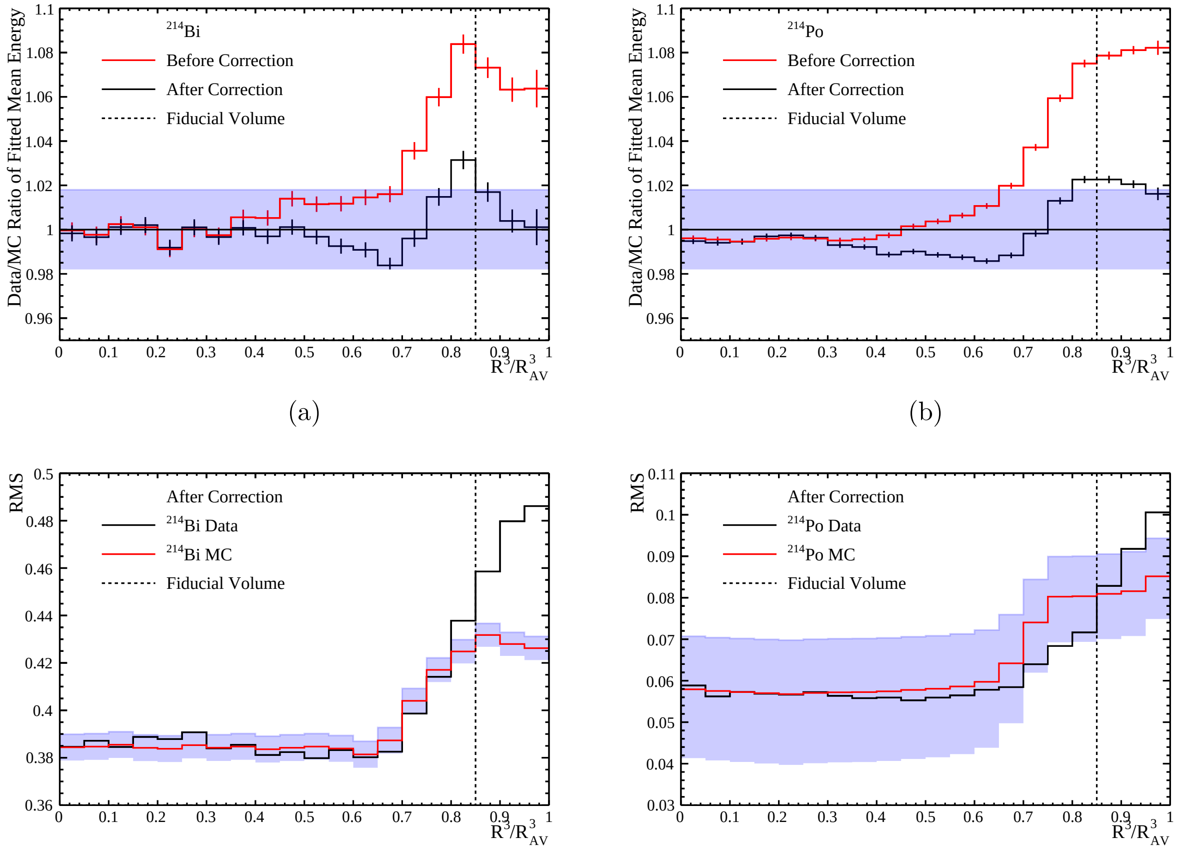

(a) (b)

(c) (d)

Figure 4.12: Plots showing the systematic uncertainties on the energy reconstruction overlayed on the results from tagged ^{214}Bi and ^{214}Po. The uncertainties cover the remaining discrepancies between simulation and data.

Chapter 5

BACKGROUNDS TO $0\nu\beta\beta$ IN SNO+

One of the advantages of the phased approach taken by SNO+ is the ability to measure many backgrounds before deploying tellurium in the detector. This is also beneficial because it allows these background analyses and measurements to be made without any need for blinding data in the region of interest (ROI) or any risk of biasing a $0\nu\beta\beta$ analysis. In addition, it allows SNO+ to either rule out any unexpected backgrounds or to understand them before a $0\nu\beta\beta$ analysis is performed. The SNO+ $0\nu\beta\beta$ background model, and two analyses performed to measure these backgrounds are presented in the following chapter.

5.1 SNO+ $0\nu\beta\beta$ Background Model

The primary goal of the SNO+ experiment is to search for $0\nu\beta\beta$. The signature of this signal for ^{130}Te is a peak at its Q value of 2.5 MeV. The decay proceeds through emission of two electrons and the primary distinguishing factor is the energy deposited in the scintillator. Additional methods of identifying and removing backgrounds through pulse shape discrimination [75] or measurement of direction in scintillator are in development.

The SNO+ collaboration has developed a detailed model of all potential backgrounds that can mimic the $0\nu\beta\beta$ signal. The expected reconstructed energy distribution around the $0\nu\beta\beta$ Q value

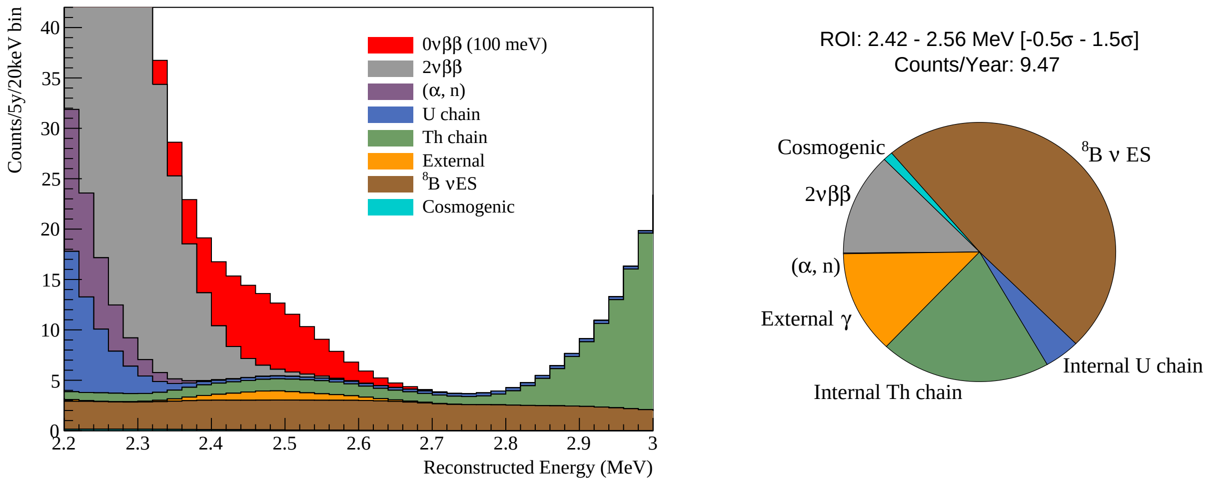

Figure 5.1: Expected reconstructed energy distribution of the $0\nu\beta\beta$ signal and backgrounds, as well as a pie chart showing the breakdown of backgrounds in the region of interest (2.42-2.56) MeV.

is shown in Figure 5.1. The SNO+ background model includes many backgrounds not within the energy range of this plot [76]. Only those with a non-negligible probability of reconstructing in the energy ROI are discussed in this section.

5.1.1 Solar Neutrinos

The expected dominant background to the $0\nu\beta\beta$ signal is solar neutrinos. Only one process in the Sun produces a significant amount of neutrinos which reconstruct at $\sim$2.5 MeV. ^{8}B solar neutrinos have a broad energy spectrum as can be seen in Figure 5.1 and interact in the detector via elastic scattering off of an electron. ^{8}B solar neutrinos have been studied in detail by many solar neutrino experiments and the rate is well measured. This gives good confidence in the prediction for the rate of this background. The single electron signal is not distinguishable from the double electron signal from $0\nu\beta\beta$, however, the direction of the electron is strongly correlated with the direction of the neutrino. As a result, reconstruction of the direction of events could allow a reduction of this background.

5.1.2 Internal Th and U Chains

Thorium-232 (^{232}Th) and Uranium-238 (^{238}U) are naturally occurring isotopes with very long half lives of 1.4×10^{10} and 4.5×10^{9} years respectively. Trace amounts of these elements exist in all of the

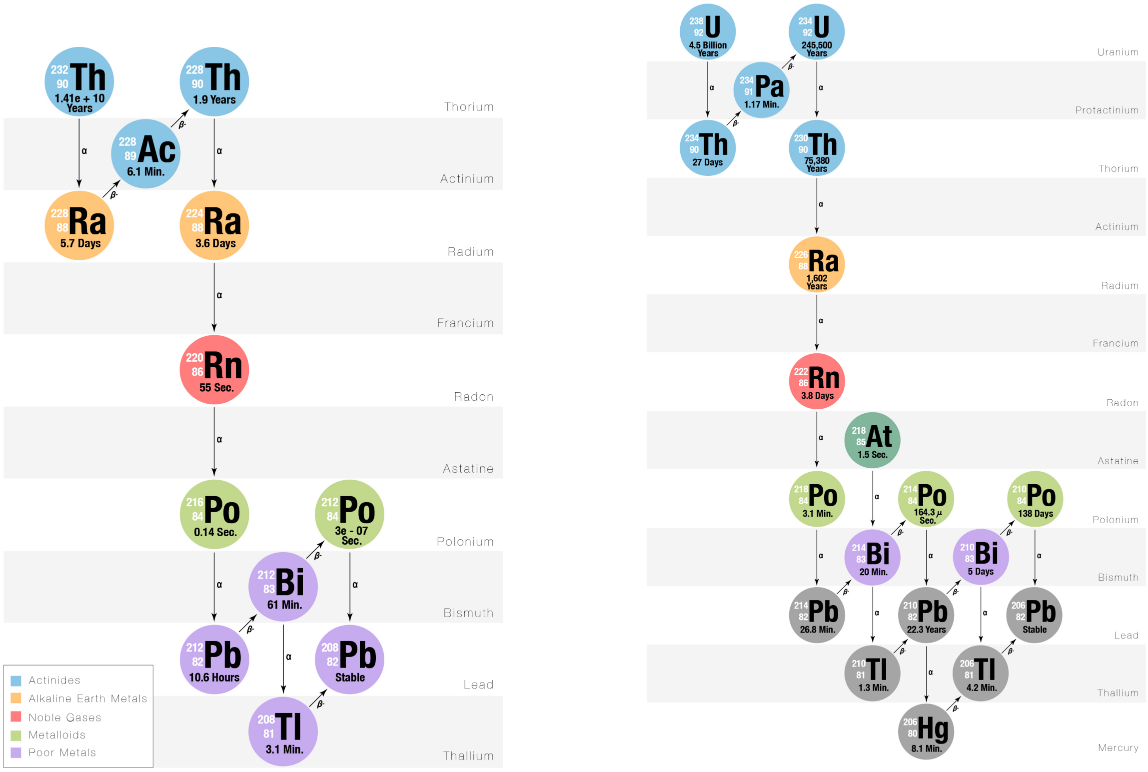

Figure 5.2: (Left) ^{232}Th decay chain, (Right) ^{238}U decay chain. The decay channel and half lives are listed for each isotope.

components of the SNO+ detector and their decays lead to a cascade of radioactive decays before each reaches a stable isotope of lead. These two radioactive decay chains are shown in Figure 5.2. Given their long half lives, these elements provide a near constant rate of decays in the detector resulting in "secular equilibrium" where the production of each isotope in the chain is the same as the decay rate. When equilibrium is achieved, the measured rate of decays in the chain can be used to estimate the intrinsic ^{232}Th and ^{238}U content of the detector.

The introduction of additional radioactive isotopes within the chain can break this equilibrium for all downstream isotopes. For example, exposure of the detector to mine air can introduce additional ^{222}Rn into the detector volume. This leads to an elevated rate of ^{222}Rn and all downstream isotopes. Each isotope will then decay away with the longest half life of the parent isotopes within the chain. For example, with ^{222}Rn, all decays in the chain prior to ^{210}Pb will decay back to equilibrium with the ^{222}Rn half life of 3.8 days. However, the isotopes later in the chain decay away with the long ^{210}Pb half life of 22.3 years.

Each decay in these chains proceeds through emission of either an α or a β with a fixed maximum energy (the "Q value") for the decay. Some decays also result in the emission of γs. Two isotopes within these chains are of particular importance because their Q values are near the $0\nu\beta\beta$ ROI: ^{214}Bi and ^{212}Bi.

^{214}Bi is part of the ^{238}U chain and proceeds via a β decay with a Q value of 3.3 MeV. As a result, this decay can fall in the $0\nu\beta\beta$ ROI. The following decay in the chain is ^{214}Po, which decays via an α with energy 7.8 MeV and has a lifetime of just 237 μs. Due to quenching, this α produces an amount of light similar to a $\sim$0.8 MeV electron.

^{212}Bi is part of the ^{232}Th chain and proceeds via a β decay with Q value of 2.3 MeV. This Q value is slightly below the $0\nu\beta\beta$ energy however the following decay in the chain is ^{212}Po, which has a lifetime of 430 ns. ^{212}Po decays via an α with an energy of 9.0 MeV. Because of its short lifetime, the ^{212}Po can fall in the same trigger window as the ^{212}Bi. This causes an increase in the reconstructed energy, which can result in the event reconstructing in the ROI.

This coincidence of the β and α decays in the same place with a short time difference is a very distinct signal that allows identification of ^{214}Bi and ^{212}Bi decays. This identification can then be used to produce a pure sample of ^{214}Bi or ^{212}Bi decays (as was done in Section 4.3.6) or it can be used to efficiently remove nearly all ^{214}Bi and ^{212}Bi decays (as will be done in Section 5.3).

Efficient rejection of these backgrounds is essential to the search for $0\nu\beta\beta$. While solar neutrinos are expected to be the dominant background after all rejection, the rate of these BiPo events is expected to be much higher. The sensitivity projections for SNO+ and Figure 5.1 are made using the expected concentration levels of ^{232}Th and ^{238}U and rejection of ^{214}BiPo/^{212}BiPo events at 99.99%/99% efficiency.

5.1.3 External γ

External γ events come from the same ^{232}Th and ^{238}U chains present in the components external to the scintillator volume. This includes the AV, rope supports, external water, and PMTs. Decays in these chains produce γs outside of the target volume which either propagate into, or are reconstructed within the target volume. The most relevant isotopes in these decay chains are ^{208}Tl and ^{214}Bi.

^{208}Tl is a $\beta\gamma$ decay with a Q value of 5.0 MeV and a γ energy of 2.6 MeV. This γ can propagate from the external volume into the fiducial volume and have an energy very close to that of a potential $0\nu\beta\beta$ signal making it the most important external background for the $0\nu\beta\beta$ search. The β produced in the ^{214}Bi decay does not propagate far and is therefore less likely to fall in the $0\nu\beta\beta$ fiducial volume. However, measurements made in the water phase use the external water, requiring ^{214}Bi to be accounted for.

These backgrounds are of particular importance because they are the only backgrounds that will have a radial dependence. This radial dependence is almost entirely due to the mean free path length of the γ as it Compton scatters electrons as demonstrated in Figure 5.3. As a result, the fiducial volume used in a $0\nu\beta\beta$ analysis will depend strongly on the external background levels.

5.1.4 $2\nu\beta\beta$

The remaining significant background to $0\nu\beta\beta$ is $2\nu\beta\beta$ decay. As no ^{130}Te was present in the detector, this background is not considered in the following analyses, a benefit of SNO+'s phased approach.

5.2 External Backgrounds in Water Phase

The first of these two background analyses is a measurement of the external backgrounds during the SNO+ water phase. These external backgrounds are divided into four types based on their source: AV and Ropes, External Water, PMT, and Internal Water. The ^{214}Bi and ^{208}Tl backgrounds for all sources as well as the AV and Ropes backgrounds were found to have very similar distributions in simulation and were combined in this analysis.

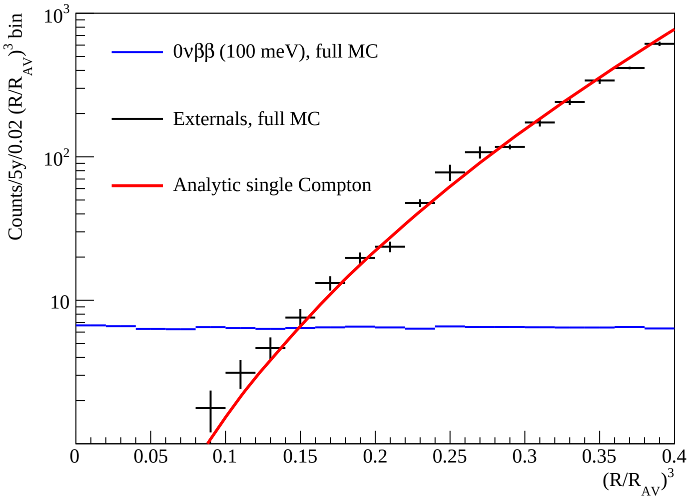

Figure 5.3: Radial distributions of a simulated $0\nu\beta\beta$ signal compared to simulated external γ decays and an analytical calculation of the expected distribution of Compton scatters of the γ. The external γ MC and analytical calculation agree well, showing that the physics of Compton scattering drives the radial dependence.

Two main variables are used to distinguish the events: the radial position of the event (R^3/R^3_{AV}), and the dot product of the reconstructed direction of the event with its reconstructed radial unit vector $\hat{U} \cdot \hat{R}$. A diagram for an example event occurring in the external water and pointed outward is shown in Figure 5.4. A value of $\hat{U} \cdot \hat{R} > 0$ indicates the event is pointed outward towards the PMTs and a value < 0 indicates the event is pointed inward towards the target volume. In addition, the reconstructed energy of the event, and a variable describing how directional the detected photons were, β_{14}, are used to select ^{214}Bi and ^{208}Tl events.

The analysis uses data and simulation to identify regions that are dominated by each background. The populations of the different backgrounds can be seen in the plot of $\hat{U} \cdot \hat{R}$ vs R^3/R^3_{AV} from data shown in Figure 5.5. A fairly uniform isotropic background from the internal and external waters can be seen in the internal and external regions of the detector. In addition, a large peak of events can be seen at $R^3/R^3_{AV} = 1$. This peak comes from events on the AV and Ropes. Finally, a large number of events pointing inward ($\hat{U} \cdot \hat{R} < 0$) at high radius correspond to backgrounds from the PMTs. The regions dominated by each of the four backgrounds are marked by boxes in Figure 5.5 and defined in Table 5.1. The reconstructed energy range used in this analysis

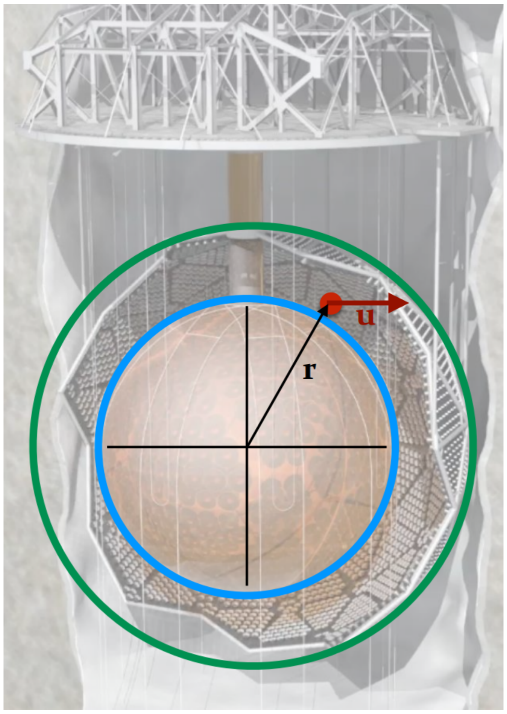

Figure 5.4: Diagram showing U and R used to calculate $\hat{U} \cdot \hat{R}$ for an event in the external water pointing outward.

is greater than the average reconstructed energies of ^{214}Bi and ^{208}Tl events. This is required to remove contamination from other backgrounds such as ^{40}K.

A box analysis was performed using these regions. Simulations of each background were used to estimate the expected number of events in each region due to each background at the nominal levels used for sensitivity projections. These simulated backgrounds are then scaled to match the number of observed events in data in each region taking into account the contamination from other backgrounds. This gives a system of four equations with four unknowns:

$$\sum_i R_i \times f_i^j = N_{\text{obs}}^j \tag{5.1}$$

where i is the source of the events and j is the box used to identify them for the internal water, external water, AV + Ropes, and PMTs. f is the fraction of events falling in a given box, N is the number of observed events in a given box, and R is the rate of each background. Each f_i^j comes

Region	Cuts
All	Valid Reconstruction Pass Data Cleaning Cuts $-0.14 < \beta_{14} < 0.95$ ITR > 0.55 Cleaned PMT Hits ≥ 15 $3.0 <$ E < 5.0 PMT Hits < 39 $R_{AV} < 1$ or -5m $<$ posz $<$ 5m
AV	5.55 m $< R_{AV} <$ 5.7 m $U \cdot R_{AV} > 0.4$
External Water	6.3 m $< R <$ 6.8 m $U \cdot R > 0.4$
PMT	$1.6 < R^3 < 2.0$ $U \cdot R < -0.8$
Internal Water	$R_{AV} <$ 4.7m

Table 5.1: Summary of cuts used to identify each external background.

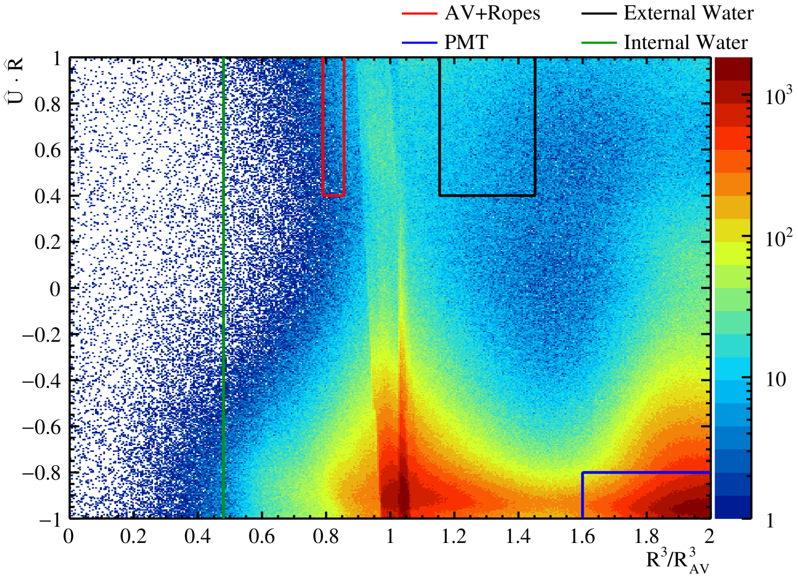

Figure 5.5: $\hat{U} \cdot \hat{R}$ vs. R^3/R^3_{AV} distribution for background events in water phase data.

Parameter	Uncertainty
x offset (mm)	$^{+50.1}_{-55.6}$
y offset (mm)	$^{+47.7}_{-59.6}$
z offset (mm)	$^{+75.8}_{-34.7}$
x scale (%)	$(x > 0)$ $^{+0.16}_{-0.23}$ $(x < 0)$ $^{+0.17}_{-0.30}$
y scale (%)	$(y > 0)$ $^{+0.12}_{-0.22}$ $(y < 0)$ $^{+0.17}_{-0.45}$
z scale (%)	$(z > 0)$ $^{+0.30}_{-0.42}$ $(z < 0)$ $^{+0.09}_{-0.24}$
x resolution (mm)	$\sqrt{3214 + \lvert 0.393x - 290 \rvert}$
y resolution (mm)	$\sqrt{2004 + \lvert 0.809y - 1365 \rvert}$
z resolution (mm)	$\sqrt{7230 + \lvert 0.730z + 3211 \rvert}$
Angular resolution	$^{+0.122}_{-0.020}$
β_{14}	$^{+0.005}_{-0.010}$
Energy scale (%)	1.02
Energy resolution	$^{+0.0084}_{-0.0079}$

Table 5.2: Summary of the evaluated systematic uncertainties for the reconstructed parameters. From [52].

from the simulation of each background, N^j_{obs} comes from the observed events in data, and the rates R_i are solved for. The results are reported as the scaling factor relative to the nominal rates of each background used for sensitivity projections (i.e. 1 corresponds to the nominal rate).

Systematic errors due to uncertainties in energy, position, direction ($\hat{U} \cdot \hat{R}$), and isotropy (β_{14}) were evaluated using the ^{16}N calibration source described in Section 4.3. Table 5.2 shows a summary of all systematic uncertainties applied in this analysis. These are the same uncertainties used in the SNO+ invisible nucleon decay analysis [52].

Systematic uncertainties are applied using a "shift and refit" approach where the simulation is shifted according to each uncertainty and the rates R_i are recalculated. The differences between the nominal R_i and the systematically shifted R_i are taken as the systematic uncertainties. The individual systematic uncertainties for each parameter are then summed in quadrature to obtain the total systematic uncertainty. The uncertainties are dominated by the energy resolution and energy scale systematics due to the energy range used in the analysis.

Background	Measured Rate (Fraction of Nominal)	Expected $0\nu\beta\beta$ Background Counts (5 Years Data)
AV+Ropes	$0.21 \pm 0.009^{+0.64}_{-0.21}$	$0.6^{+1.9}_{-0.6}$
External Water	$0.44 \pm 0.003^{+0.32}_{-0.27}$	$0.1^{+0.07}_{-0.09}$
PMT	$1.48 \pm 0.002^{+1.65}_{-0.60}$	$2.3^{+2.6}_{-1.0}$
Total	-	$3.0^{+3.2}_{-2.2}$
Nominal Total	-	6.1

Table 5.3: Results of the external background analysis. The rate as a fraction of the nominal expectation and the corresponding expected $0\nu\beta\beta$ background counts for 5 years of data are given.

This analysis was performed for several data taking periods during the water phase. The final period had the largest livetime, occurred after the installation of the cover gas system which resulted in a significant reduction of radioactive backgrounds, and occurred after an optical calibration of the detector using the laserball [49]. Therefore, the results during this period are the most relevant for projections for the SNO+ tellurium phase. The results for this ~185 day livetime period are shown in Table 5.3. In addition, the effect on the expected background counts in the $0\nu\beta\beta$ ROI is shown in Table 5.3.

All measured rates are consistent with or below their nominal values. In addition, the total estimated events in the ROI at the measured rates of the external backgrounds is lower than the nominal prediction by a factor of ~2. This total is within 1σ of the nominal value due to its large systematic uncertainty. This measurement shows good agreement with expectation and is an important step in estimating the backgrounds expected in a SNO+ $0\nu\beta\beta$ analysis.

5.3 $0\nu\beta\beta$ Backgrounds in Partial Fill Phase

The second of these background analyses is an investigation of events in the $0\nu\beta\beta$ region of interest (ROI) during the partial scintillator fill phase. Limited access to SNOLAB due to COVID-19 restrictions caused a temporary pause in filling operations with 365 tons of scintillator in the detector. This period provided several months of stable data and allowed analysis and measurements of many backgrounds relevant to both the pure scintillator and Te-loaded phases of SNO+.

A diagram of the detector configuration during the partial fill phase is shown in Figure 5.6.

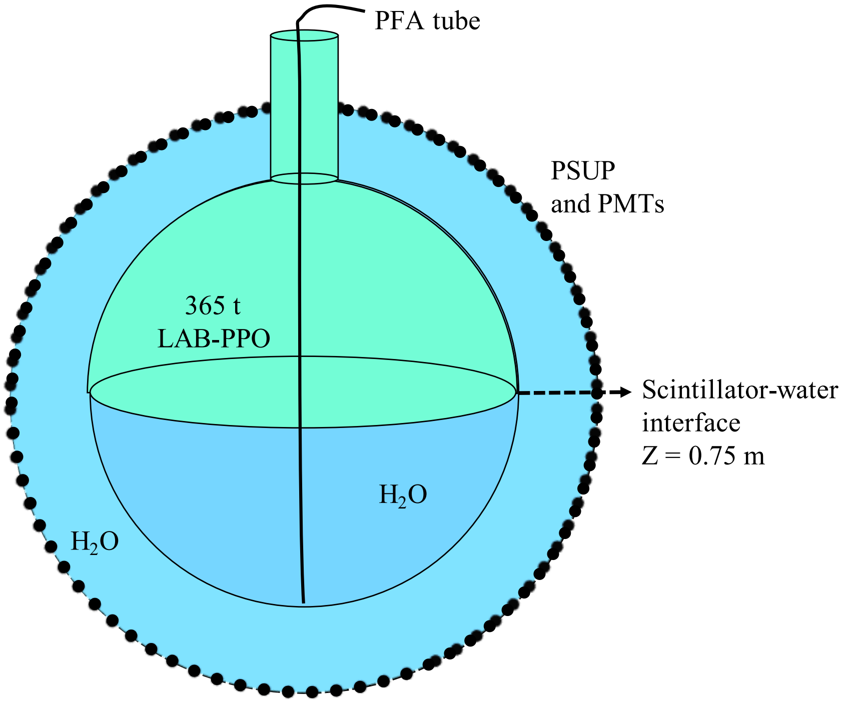

Figure 5.6: Diagram of the SNO+ detector configuration during the partial fill phase. Figure provided by A.S. Inácio [48].

During this phase, the detector was approximately half full with the less dense scintillator in the top half of the AV and the denser water in the bottom half. The interface between the scintillator and water was 0.75 m above the equator. This resulted in a smaller target volume and additional optical effects from the water scintillator interface. The fiducial volume during this period was expanded from 3.3 m to 4.0 m. This improved the total exposure but resulted in a larger expected contribution from external backgrounds. The interface also introduces an additional background source: radioactive decays from the internal water.

The scintillator contained 0.5 g/L PPO, less than the planned 2.2 g/L. This resulted in a light yield that was lower than projected for the full 2.2 g/L. Also, the concentration of PPO affects the scintillator time profile, which is necessary to identify certain backgrounds. These challenges resulted in a less efficient rejection of certain backgrounds. Finally, a plastic "PFA tube" (perfluoroalkoxy) was deployed in the center of the detector to aid with extraction of the water at the bottom of the detector. This tube also presented another source of radioactivity and optical effects. While this unorthodox configuration presented several challenges during the partial fill phase, analysis of the data taken during this period was still performed.

This "ROI analysis" aims to understand and tag all events in the future $0\nu\beta\beta$ ROI while keeping a high efficiency for a hypothetical $0\nu\beta\beta$ signal. The goal of the analysis is to ensure that all measurable backgrounds during the partial fill phase are consistent with the expectations used in sensitivity projections and that no unexpected backgrounds are present in the $0\nu\beta\beta$ ROI.

The dominant backgrounds in this analysis are the previously described ^{214}BiPo and ^{212}BiPo events which can be identified due to their coincidence decays. This analysis identifies and removes ^{214}BiPo events by tagging the coincidences using the number of PMT hits of the delayed event (NHits Delayed), as well as the time difference of the events (Δt), and the distance between the two events (Δr). A likelihood analysis is performed to tag and remove these events.

A sample of simulated ^{214}BiPo events and time randomized data events are used to create PDFs of Δt vs. Δr and the PMT Hits of the delayed event for ^{214}BiPo events and accidental coincidences.

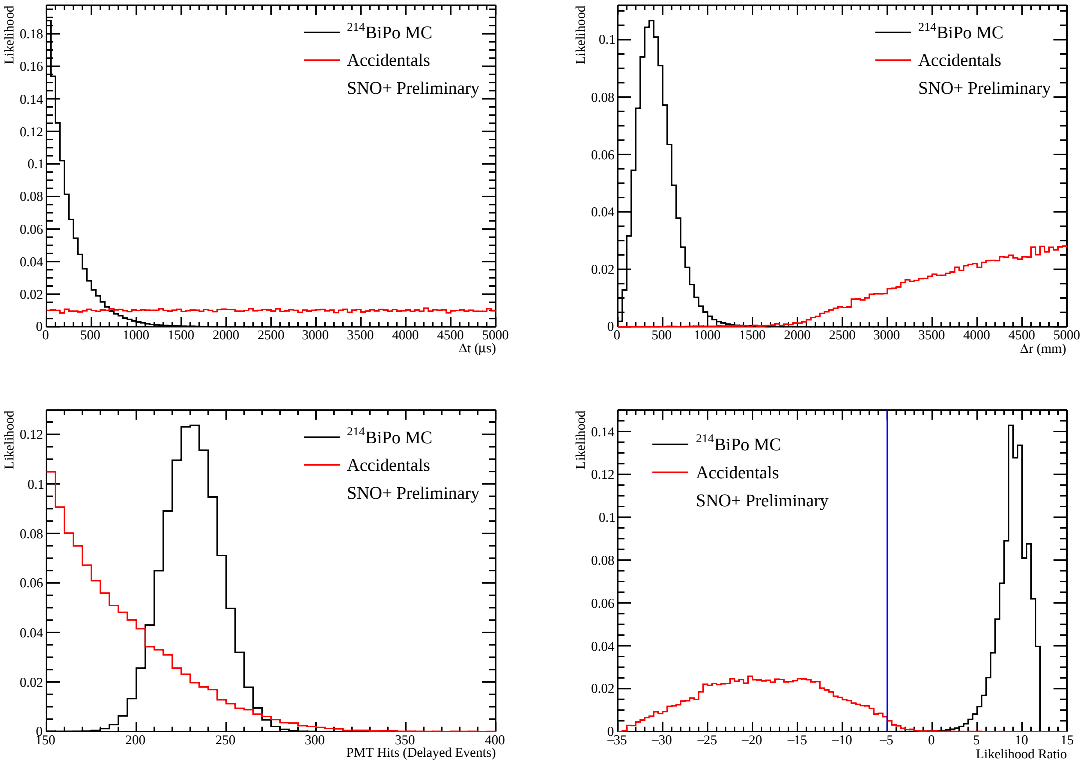

Figure 5.7: PDFs and likelihood ratio used to discriminate between ^{214}BiPo events and accidental coincidences. The blue line in the likelihood ratio plot shows the cut used to tag the ^{214}BiPo events.

A likelihood ratio is calculated for the hypotheses of a ^{214}BiPo event and an accidental coincidence, and a selection is applied to tag events as ^{214}BiPo. The PDFs and resulting likelihood ratio for both ^{214}BiPo MC and randomized data (accidentals) are shown in Figure 5.7. Other selections are applied to remove events that occur after muons pass through the detector or events where the delayed event is affected by instrumental effects.

In addition to the likelihood ratio, the $\alpha - \beta$ classifier described in Section 4.2.4 is applied to identify and remove events where the $^{214/212}$Po event occurs within the same trigger window as the $^{214/212}$Bi event. This is particularly important for the ^{212}BiPo background as the Po has a lifetime of 430 ns which results in a significant number of these "in-window" events.

Due to the challenges associated with the detector conditions, the 99.99/99% rejection efficiencies of $^{214/212}$BiPo events were not expected to be achieved in the partial fill phase. Initial tests

Background Source	Expected Events in Partial Fill ROI
Internal Water	1.8
PFA Tube ^{214}BiPo	2.9
Externals	2.5
(α, n)	0
Th Chain (Scint)	0.1
U Chain (Scint)	0.3
^{8}B νES	0.5
Total Backgrounds	8.0

Table 5.4: Expected events from each background source in the ROI during partial fill.

showed a ^{214}BiPo tagging efficiency of 99.7% in simulation. However, applying this tagging efficiency to the data resulted in a prediction that was smaller than the observed number of events in data. Detailed investigations of this tagging efficiency resulted in optimization of the analysis cuts, and development of a method to account for certain instrumental effects in the SNO+ detector. It also resulted in the campaign described in Section 3.5 which improved the properties of the trigger system and its model in simulation. After these improvements, the analysis predicted a 99.9% tagging efficiency for ^{214}BiPo events and a 94.2% tagging efficiency ^{212}BiPo events in simulation.

After removal of $^{214/212}$BiPo and other tagged background events, the remaining events can be compared with the expected number of backgrounds falling in the $0\nu\beta\beta$ ROI. The location of the ROI was determined using the energy distribution of a simulated $0\nu\beta\beta$ signal. A Gaussian is fit to the peak and the range used is $[-0.5\sigma, +1.5\sigma]$, the same values used for SNO+ sensitivity estimates. This gives the ROI in partial fill to be from 2.37-2.56 MeV.

The backgrounds in the previously described model along with the additional backgrounds from the radioactivity of the internal water and the PFA tube are used to estimate the expected number of events remaining in the ROI. Simulation is used to predict the probability of an event from each background source falling in the ROI and existing measurements or predictions are used to predict the rates of each background. For example, the measured rates obtained from the external background analysis in the previous section are used to predict their contributions in partial fill.

In a sample of 70 days of stable data taken during the partial fill phase from June-October 2020,

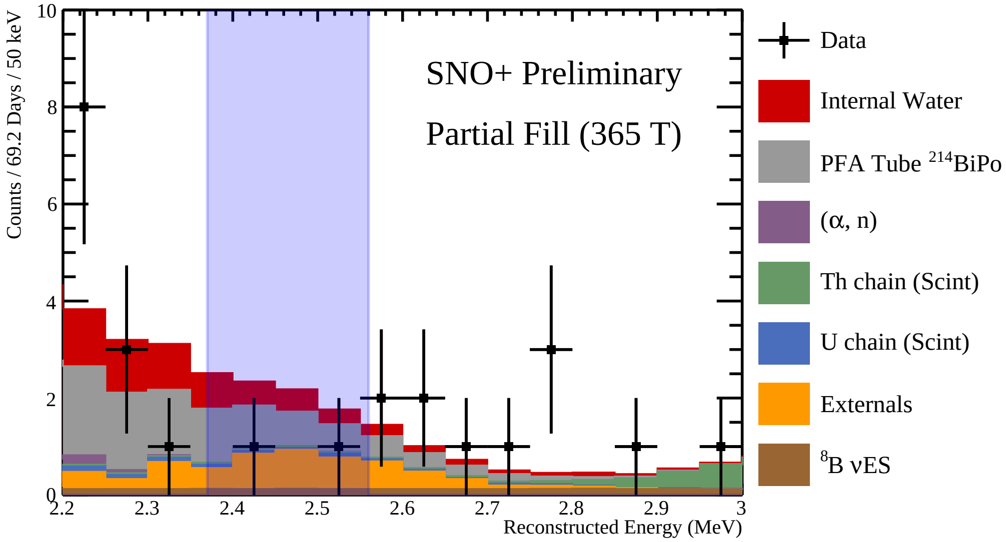

Figure 5.8: Events remaining in the 4.0 m FV after removal of tagged $^{214/212}$Bi events. Two events are observed in the ROI compared to an expectation of 8. The ROI is highlighted in blue.

an expectation of 8.0 events is predicted in the ROI. The expectation for each of the background sources individually is shown in Table 5.4. The energy distribution of the observed events is shown in Figure 5.8. Two events are observed in the ROI, less than expectation. Figure 5.9 shows the position distribution of events in the detector in an extended energy range from ∼2.3-2.8 MeV. The fiducial volume is shown as a black line, and the two events in the ROI are displayed as red diamonds.

In this detector state, the observed number of backgrounds is still found to be below expectation. Many of the challenges associated with this analysis will not be present in future data. The backgrounds from the internal water and PFA tube will be gone. No optical effects from the scintillator water interface or PFA tube will be present. The full volume will allow a smaller radial cut, reducing external backgrounds, and the full PPO should provide improved timing allowing more efficient background rejection.

A detailed understanding and constraint of all backgrounds is one of the most important steps towards a successful $0\nu\beta\beta$ result. SNO+ has an advantage by being able to measure these

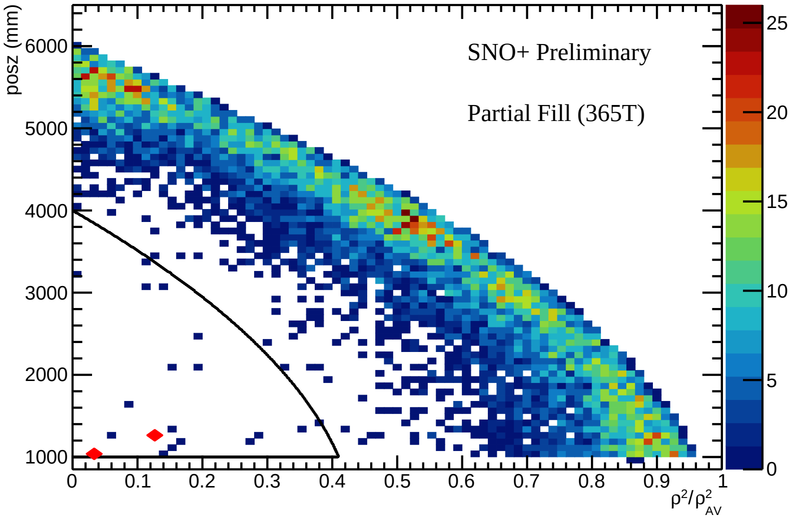

Figure 5.9: The color map shows the position of events in an extended energy range from ∼2.3-2.8 MeV. The fiducial volume is shown as a black line, and the two events in the ROI are displayed as red diamonds.

important backgrounds before filling with our $0\nu\beta\beta$ isotope ^{130}Te. Analyses of these backgrounds will provide useful insights to determine whether backgrounds are within our expectation and whether better rejection of backgrounds can be achieved for a future $0\nu\beta\beta$ result from SNO+. The two measurements presented here show backgrounds below or consistent with expectation.

Chapter 6

REACTOR ANTINEUTRINO SIGNAL CALCULATION

The following few chapters describe the primary analysis of this thesis: a measurement of neutrino oscillation parameters using reactor antineutrinos.

Reactor antineutrinos are produced in large quantities in nuclear reactors and then propagate to the SNO+ detector. This chapter describes the calculation of the expected rate of reactor antineutrino interactions in SNO+. This chapter also describes the calculation of the expected rates of the dominant backgrounds able to mimic the reactor antineutrino signal.

6.1 Reactor Antineutrino Production

Nuclear power plants produce electrical power using the heat produced in nuclear fission reactions. Heavy isotopes are bombarded with neutrons to induce fission reactions which, in turn, emit more neutrons, continuing the reaction. The daughter nuclei of these nuclear fission reactions are unstable and undergo beta decay, a process in which a bound neutron is converted into a proton, producing an electron and an electron antineutrino ($n \rightarrow p + e^- + \bar{\nu}_e$). There is no significant production of any other neutrinos, making nuclear reactors a pure $\bar{\nu}_e$ source. The rate of antineutrino emission

Reactor Type	^{235}U	^{238}U	^{239}Pu	^{241}Pu
PHWR	0.52	0.05	0.42	0.01
PWR/BWR	0.568	0.078	0.297	0.057

Table 6.1: Relative contribution of each fissile isotope (f_i) to the fuel composition of each reactor design.

for a nuclear reactor is given by:

$$\frac{d^2 N_{\bar{\nu}_e}(E_{\bar{\nu}_e}, t)}{dEdt} = \frac{P_{th}(t)}{\sum_i f_i \epsilon_i} \sum_i f_i S_i(E_{\bar{\nu}_e}) \tag{6.1}$$

where the sums are over the fissile isotopes, f_i is the fraction of fissions due to the ith isotope, ϵ_i is the average thermal energy released per fission of the ith isotope, $S_i(E_{\bar{\nu}_e})$ is the number of antineutrinos emitted per fission of the ith isotope, and $P_{th}(t)$ is the thermal power of the reactor.

Commercial nuclear reactors primarily contain four fissile isotopes: ^{238}U, ^{235}U, ^{239}Pu, and ^{241}Pu. The fuel composition of a nuclear reactor depends on its design. There are many different nuclear reactor designs, however only three are used by nuclear reactors in North America: pressurized heavy water reactors (PHWR), pressurized water reactors (PWR), and boiling water reactors (BWR). The fuel composition of PWR and BWR have been measured by the KamLAND and Daya Bay collaborations [35] [77] while the fuel composition of PHWR was provided by private communication from the Atomic Energy of Canada Limited (AECL). The fuel compositions for each reactor type are summarized in Table 6.1. Reactors of all other types have a small contribution to the total flux and are modeled as PWR.

The energy spectra of all four fissile isotopes are modeled in `RAT` using the Huber-Mueller model. Each energy spectrum is modeled as an exponential of a fifth-order polynomial. The models for ^{235}U, ^{239}Pu, and ^{241}Pu are obtained by measurements of the beta decay spectrum from exposure of these isotopes to thermal neutrons [78]. ^{238}U only undergoes fission induced by fast neutrons, and its model is calculated theoretically [79]. The antineutrino emission spectrum for each isotope is shown in Figure 6.1. These energy distributions predict that ~6 $\bar{\nu}_e$ are produced per fission reaction [80], and calculations of the energy released per fission for each isotope (ϵ_i) gives

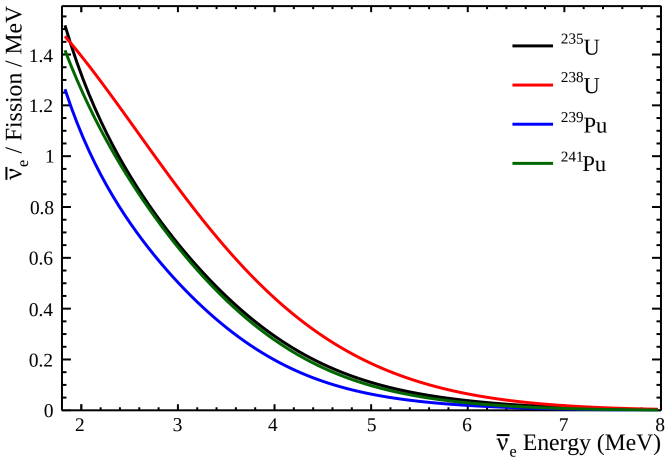

Figure 6.1: The energy spectrum of emitted antineutrinos for each fissile isotope ($S_i(E_{\bar{\nu}_e})$) as modeled in `RAT` .

~200 MeV [81]. These values correspond to a rate of $\sim 2{\times}10^{20}$ $\bar{\nu}_e$ / s / GW thermal power [80].

The final value needed to determine the rate of neutrinos produced by a nuclear reactor is thus its thermal power output (P_{th}). Nuclear reactor complexes vary in size with each having a designed power output. The design power of nuclear reactors is publicly available; however, several factors cause the actual power output of a nuclear reactor complex to vary over time. The power output regularly varies to match the demands of the electrical grid, cores are shut off due to refueling and maintenance, and reactors are either permanently shut down or newly constructed.

The International Atomic Energy Agency (IAEA) annually publishes a report with details of the operations of every nuclear reactor in the world. This report includes the load factor (LF) which corresponds to the percentage of the designed thermal power at which the reactor is running. The report provides the LF for each reactor core for each month of the year. This gives reasonably good time resolution for most nuclear reactors in the world.

Three Canadian nuclear reactor complexes contribute ~60% of the total antineutrino flux at SNO+. Thus, a more precise time resolution for these reactors is desirable. The Independent Energy System Operator (IESO) reports the hourly electrical output of these reactors. The electrical output can be converted to a LF and has been shown to reproduce the monthly data reported by IAEA [58]. In simulation, the average daily electrical power is used to model the three Canadian reactor complexes.

There are several additional effects with small contributions to the expected flux. These effects are not modeled in the simulation and are instead assigned a systematic uncertainty. Fission of other isotopes was found by the Daya Bay collaboration to contribute to the $\bar{\nu}_e$ flux at sub-percent level [82]. Daya Bay has also published measurements of these fission fractions as a function of fuel burn-up during a complete refueling cycle [82]. Only the average fission fractions are used in this analysis. These uncertainties will be discussed in Chapter 8.

6.2 Reactor Antineutrino Propagation

With the $\bar{\nu}_e$ production rate from each reactor now calculated, we must next account for the propagation of the neutrinos to the SNO+ detector. The neutrinos are emitted isotropically from each reactor core and thus the $\bar{\nu}_e$ flux at the SNO+ detector is given by:

$$N_{SNO+} = \sum_i \frac{N_i}{4\pi L_i^2} \tag{6.2}$$

where N_{SNO+} is the total flux at SNO+, the sum is over all nuclear reactors, N_i is $N_{\bar{\nu}_e}$ from Equation 6.1 calculated for the ith reactor, and L_i is the distance between SNO+ and the ith reactor. The dependence on $1/L^2$ results in the closest reactors having the largest contributions.

The calculations of the $\bar{\nu}_e$ flux have so far ignored the effect of neutrino oscillation. The full three flavor survival probability, including matter effects as described in Section 2.3.2, is used to calculate the resulting $\bar{\nu}_e$ flux after oscillation using the method described in [83]. This calculation is performed using the 2021 PDG global best fit oscillation parameters [27] unless otherwise specified. These oscillation parameters are summarized in Table 6.2.

The Bruce reactor complex is both the closest reactor, at a distance of 240 km, and has the largest P_{th} in North America (and second largest in the world), at 18 $\mathrm{GW_{th}}$. As a result, it has

Oscillation Parameter	Value
Δm^2_{21}	$7.53 \pm 0.18 \times 10^{-5}$ eV^2
Δm^2_{32}	$2.453 \pm 0.0033 \times 10^{-3}$ eV^2
$\sin^2 \theta_{12}$	$0.307^{+0.013}_{-0.012}$
$\sin^2 \theta_{23}$	0.546 ± 0.021
$\sin^2 \theta_{13}$	0.0220 ± 0.0007

Table 6.2: PDG 2021 [27] global fit oscillation parameters used in $\bar{\nu}_e$ prediction.

the largest contribution to the total $\bar{\nu}_e$ flux at SNO+ (∼40%). Two additional Canadian reactor complexes (Pickering and Darlington) are the next closest at 350 km with contributions of 10% each to the total $\bar{\nu}_e$ flux at SNO+. Because such a large fraction of the flux comes from just three reactor complexes with similar baselines, the features in the oscillated energy spectra of these complexes are fairly well preserved in the total energy spectrum. A full list of all reactors within 1000 km of SNO+ along with their design powers can be found in Table A.1.

6.3 Reactor Antineutrino Interaction and Detection

Now that the neutrinos have made their way to SNO+, they can interact and be detected. The process by which $\bar{\nu}_e$'s are detected is called Inverse Beta Decay (IBD). In this process, an antineutrino undergoes a charged current interaction with a proton, yielding a neutron and a positron ($\bar{\nu}_e + p \to e^+ + n$). The Feynman diagram and a schematic diagram of the interaction are shown in Figure 6.2.

This process has several desirable qualities, including a strong correlation between $\bar{\nu}_e$ and e^+ energy, two detectable signals (e^+ emission and n capture) occurring near each other in both time and space, and a larger cross section than elastic scattering. While the cross section for this interaction is still small, the flux of $\bar{\nu}_e$ from nuclear reactors is large enough to provide a detectable signal.

In order for an IBD interaction to occur, the neutrino must have sufficient energy to produce the final products in the rest frame of the proton. This results in an energy threshold for electron antineutrinos of:

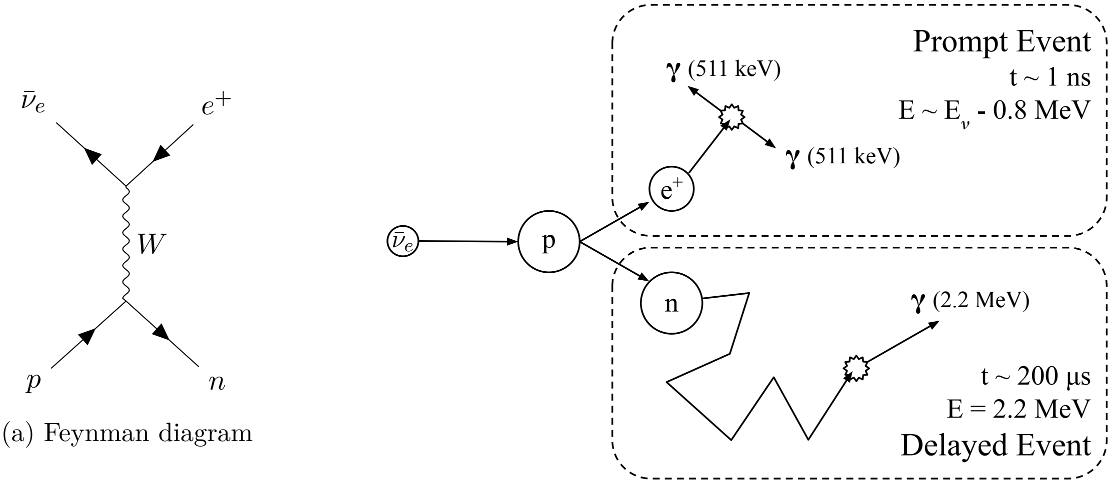

(a) Feynman diagram

(b) Schematic diagram

Figure 6.2: Two representations of the IBD process.

$$E_\nu^{\text{thresh}} = \frac{(m_n + m_e)^2 - m_p^2}{2m_p} = 1.806 \text{ MeV} \tag{6.3}$$

where m_n is the mass of the neutron, m_p is the mass of the proton, and m_e is the mass of the electron. For $\bar{\nu}_\mu$ and $\bar{\nu}_\tau$, m_e is replaced by m_μ and m_τ respectively. This raises the energy threshold far above the energy of antineutrinos produced by reactors, making these flavors undetectable.

For $\bar{\nu}_e$ above this energy threshold, the cross section for IBD interactions has been calculated to first order by Vogel and Beacom [84] to be:

$$\left(\frac{d\sigma}{d\cos\theta}\right)^{(1)} = \frac{\sigma_0}{2}[(f^2 + 3g^2) + (f^2 - g^2)v_e^{(1)}\cos\theta]E_e^{(1)}p_e^{(1)} - \frac{\sigma_0}{2}\left[\frac{\Gamma}{M}\right]E_e^{(0)}p_e^{(0)} \tag{6.4}$$

where σ_0 is a normalization constant, f is the vector coupling constant, g is the axial coupling constant, $E_e^{(0,1)}$, $p_e^{(0,1)}$, and $v_e^{(1)}$ are the energy, momentum, and velocity of the positron expanded in orders of $1/M$, and Γ is an additional term defined in the Vogel and Beacom paper [84]. Equation 6.4 is then numerically integrated over $\cos\theta$ in `RAT` to obtain the total cross section. Figure 6.3 shows the reactor antineutrino energy spectrum and the IBD cross section overlayed. The product

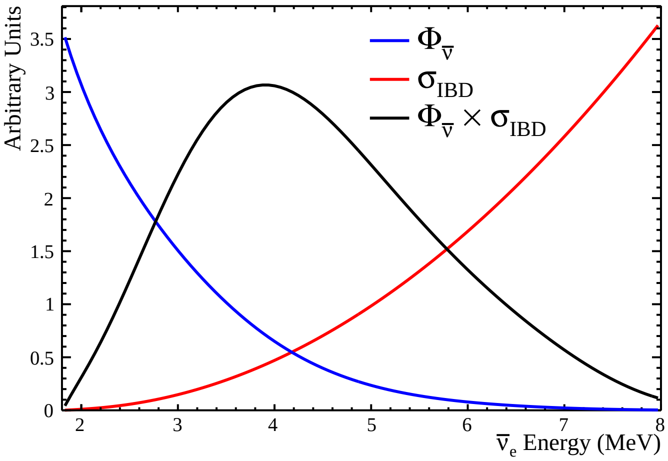

Figure 6.3: The reactor antineutrino energy spectrum and IBD cross section. The product of the reactor antineutrino energy spectrum with the IBD cross section gives the expected energy distribution of detected reactor antineutrinos without oscillation. The shape of all three are shown here with arbitrary scaling.

of these two distributions gives the expected energy distribution of reactor antineutrino interactions without oscillation.

The final value needed to calculate the rate of IBD interactions is the number of target protons. This is given by the number of hydrogen atoms in the AV:

$$N_p = \left(\frac{\rho_{\text{scint}} f_H N_A}{m_H}\right) V_{AV} \tag{6.5}$$

where ρ_{scint} is the density of the scintillator, f_H is the fraction of hydrogen in the scintillator by mass, N_A is Avogadro's number, m_H is the atomic mass of hydrogen, and V_{AV} is the volume of the AV.

The density of the scintillator is dependent on temperature and is calculated assuming the average temperature across the SNO+ volume of 12.1°C. The density of the SNO+ scintillator has been measured to be $\rho_{\text{scint}} = 0.8626 \pm 0.001$ g/cm^3 at this temperature [85]. In addition, there is a variation in temperature across the PSUP of approximately 6°C which translates to a 0.5%

uncertainty in the density of the scintillator [85].

The SNO+ liquid scintillator is composed of >99% linear alkyl benzene (LAB), whose atomic formula is $C_6H_5C_nH_{2n+1}$ where n ranges from 9 to 13. In addition, there is a small fraction ($\sim 0.2\%$) of PPO ($C_{15}H_{11}NO$). The chemical composition of the SNO+ scintillator has been certified by the provider with an accuracy of 0.1% [86]. Independent measurements performed by SNO+ collaborators are consistent with this certification. These material properties are then input into the `RAT` simulation which handles the calculation of the fraction of hydrogen in the scintillator mass.

These values, along with the known values of N_A, m_H, and V_{AV} can then be used to calculate a total of 5.75×10^{31} target protons in the AV. The number of target protons is then multiplied by the product of the rate of reactor antineutrinos reaching the SNO+ detector with the IBD cross section to arrive at the expected rate of IBD interactions in the SNO+ detector.

After the IBD interaction occurs, two signals are produced. While both the positron and the neutron are created in the interaction, the "prompt" signal comes from the positron within a few nanoseconds of the interaction while the "delayed" signal results from the capture of the emitted neutron on average $\sim$200 μs later.

Because the mass of the neutron is much larger than the positron, it is produced with very little kinetic energy, typically tens of keV. Thus, the energy of the positron is strongly correlated with the energy of the incident neutrino. In addition, the positron quickly annihilates, producing two 511 keV γs. This means the total energy deposited in the scintillator by the positron can be approximated by[2]:

$$E_{\text{dep}} \approx \text{KE}_{\bar{\nu}_e} - \text{KE}_n - m_n + m_p + m_e \approx \text{KE}_{\bar{\nu}_e} - 0.8 \text{ MeV} \tag{6.6}$$

The strong correlation between the energy deposited by the prompt positron and the energy of

---

[2] This approximation is for demonstration only and is not used in the full `RAT` simulation

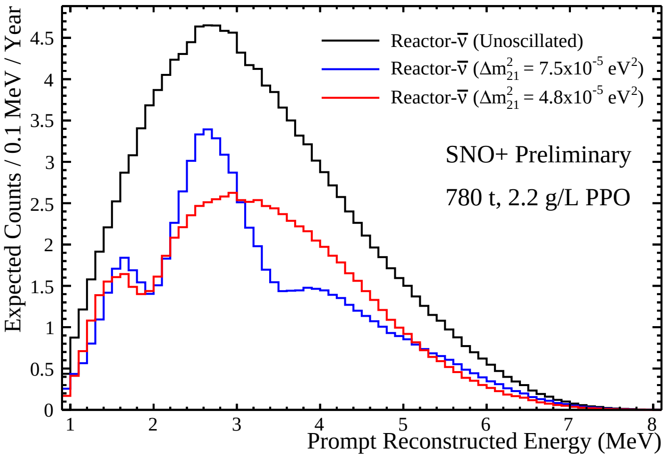

Figure 6.4: Expected rate of reactor $\bar{\nu}_e$ events for no oscillation, and two different choices of Δm^2_{21}.

the incident neutrino makes inferring the properties of the incoming neutrinos much simpler. The expected distributions of deposited energy are shown for no oscillation and two different choices of Δm^2_{21} in Figure 6.4. The features due to oscillation are clearly visible due to the favorable location of SNO+ relative to the nearest reactor complexes. The differences in energy distributions are what allow the measurement of Δm^2_{21} from these interactions.

As previously mentioned, the neutron is produced in the IBD interaction with very little kinetic energy and cannot be detected directly. After being produced, the neutron thermalizes and travels a short distance (typically $\sim$30 cm) before capturing on hydrogen. The neutron has a lifetime of $\sim$200 μs and produces a deuteron and a 2.2 MeV γ when being captured. This 2.2 MeV γ is detected and used to tag the prompt positron event.

The coincidence of these two events (prompt positron, delayed neutron capture) provides a distinct signal that is not easily mimicked, greatly reducing backgrounds.

6.4 Backgrounds to Reactor Antineutrinos

While the coincidence of the prompt positron and delayed neutron capture provides a very distinct signal, there are still backgrounds able to mimic this signal. Generally, these backgrounds are broken into two categories, correlated and uncorrelated backgrounds. Correlated backgrounds are backgrounds from physical processes that also produce multiple signals in coincidence with each other. Uncorrelated or "accidental" backgrounds are backgrounds resulting from two unrelated signals occurring near each other in both space and time by random chance. This section describes the major backgrounds to the analysis of reactor antineutrinos and their expected rates.

6.4.1 α-n

The dominant background to reactor antineutrinos in this analysis comes from α-n interactions. This background is particularly dangerous because it also produces a neutron resulting in a delayed signal that is identical to that of reactor antineutrinos.

The α-n Interaction

The α-n interaction results when an α particle is captured by a ^{13}C atom in the detector. This reaction produces a neutron and an ^{16}O atom: α + ^{13}C $\rightarrow$ n + ^{16}O. This interaction can also occur via α capture on other atoms such as $^{14/15}$N and $^{17/18}$O, however the amount of nitrogen and oxygen in the SNO+ scintillator is negligible.

Much like the IBD interaction, this interaction consists of two coincident signals: a prompt signal that can proceed through three separate channels, and a delayed signal from the capture of the neutron on hydrogen ~200 μs later. The three channels of the α-n interaction are summarized by the cartoon in Figure 6.5 and described here:

1) Proton Recoil: The first and most likely channel by which the α-n interaction proceeds is through the emission of an energetic neutron which scatters protons. While the neutron does not produce scintillation light itself, the scattered protons do, producing peak 1.

2) Inelastic Scatter: The second channel is through the emission of an energetic neutron which then scatters inelastically off of a ^{12}C nucleus. This excites the ^{12}C nucleus, and results in the emission of a 4.4 MeV de-excitation γ producing peak 2.

3) Excited ^{16}O: The third channel is through production of a low energy neutron and an ^{16}O atom in an excited state. There are two separate excited states, which each produce $\sim$ 6 MeV of

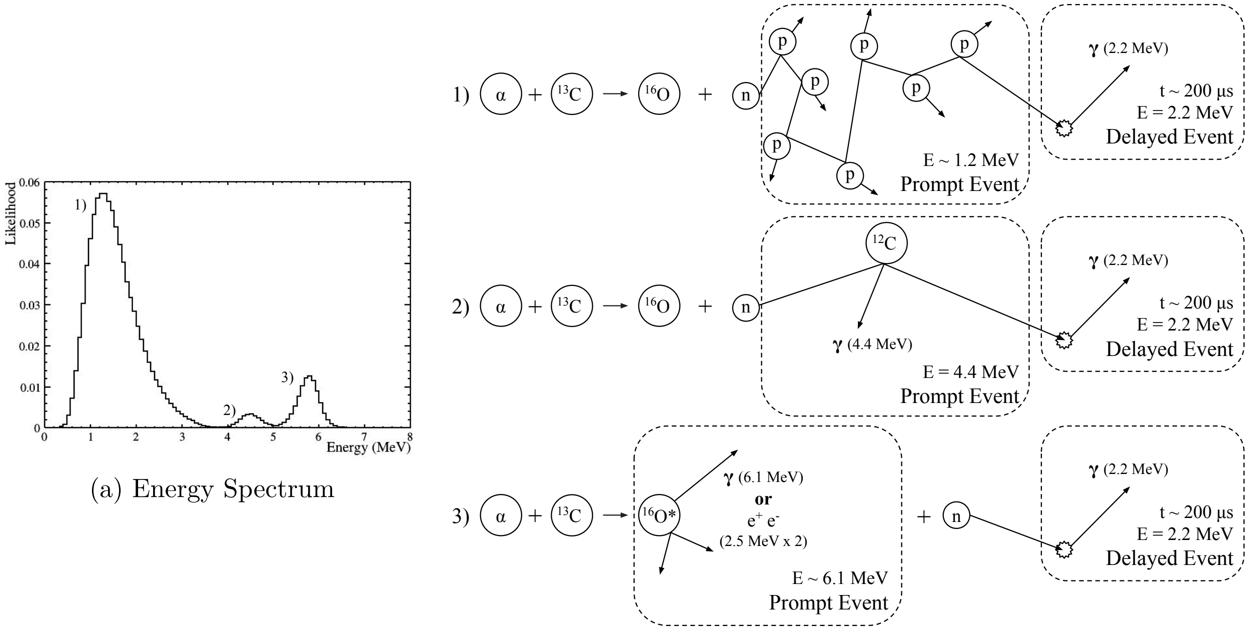

(a) Energy Spectrum

(b) Schematic diagram

Figure 6.5: a) Energy distribution showing the peaks from the different channels the α-n interaction can undergo b) Cartoon showing the three different channels by which the α-n interaction can proceed.

visible energy. These de-excitations result in peak 3.

α-n Rate

The dominant source of α particles in the SNO+ detector is decays of ^{210}Po. ^{210}Po comes from the ^{238}U chain and decays via emission of a 5.3 MeV α particle. However, due to quenching in the scintillator the α only deposits ~0.4 MeV of energy. The rate of ^{210}Po in the detector is constantly monitored by performing a fit to the detected events around the energy range of the ^{210}Po peak. This analysis is performed by S. Riccetto and provides the ^{210}Po rate on a day by day basis over the full dataset used in this analysis. This rate over time is shown in Figure 6.6. For the purposes of this analysis, the average rate over the dataset of 38 Hz is used to predict the α-n rate.

Next, the probability of an α particle undergoing an α-n reaction is needed to convert the α rate to an α-n rate. This probability comes from the following equation which treats the scintillator as a thick target:

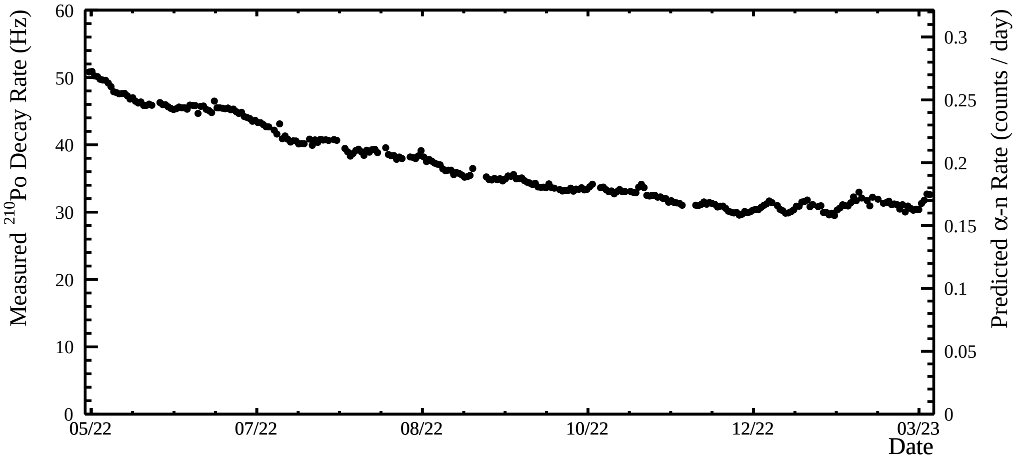

Figure 6.6: Plot showing the measured ^{210}Po and corresponding prediction for the α-n rate from the data period used in this analysis. Measured ^{210}Po rates provided by S. Riccetto.

$$P_{\alpha\to\alpha-\mathrm{n}} = n_{^{13}C}\int_0^{E_\alpha}\frac{\sigma(E)}{dE/dx}dE \tag{6.7}$$

where $P_{\alpha\to\alpha-\mathrm{n}}$ is the probability that an α produces an α-n interaction, $n_{^{13}C}$ is the number density of ^{13}C atoms in the scintillator, E_α is the energy of the ^{210}Po α (5.3 MeV), $\sigma(E)$ is the (energy dependent) cross section of the α-n interaction, and dE/dx is the stopping power.

The cross section for the α-n interaction used in `RAT` comes from the JENDL/AN-2005 library [87]. The cross section provided by JENDL is based on direct measurements of the α-n cross section [88] [89]. A comparison of the JENDL cross section with several direct measurements of the cross section is shown in Figure 6.7. The provided cross sections are total cross sections encompassing all three channels by which the α-n proceeds. The stopping power is provided by the SRIM software package [90].

The $\alpha \to \alpha$-n conversion rate has also been calculated by the Daya Bay experiment to be $5.75 \pm 0.41 \times 10^{-8}$ [92]. This calculation uses the same values for the cross section and stopping power as described above. The only difference between this calculation and the same calculation for SNO+ is thus the number density of ^{13}C atoms in the scintillator. For the SNO+ scintillator,

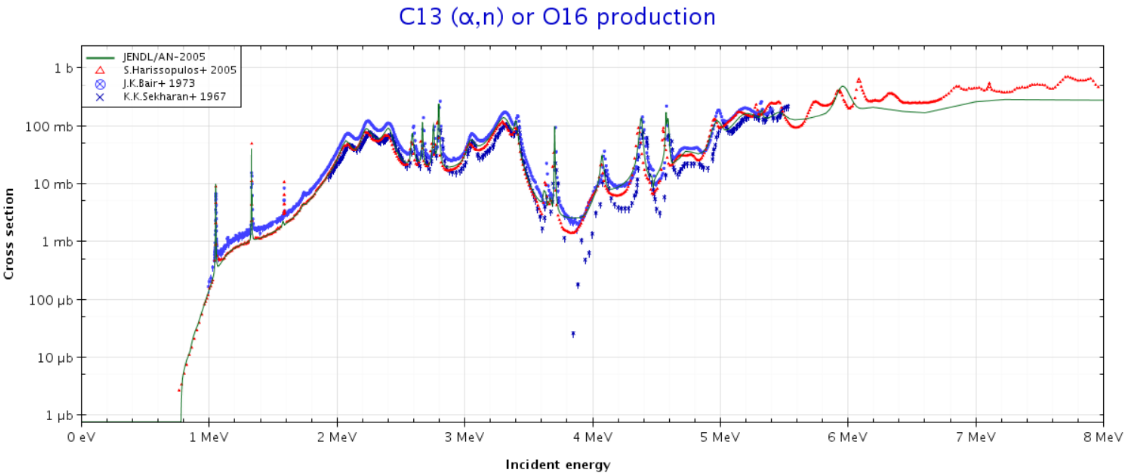

Figure 6.7: Comparison of JENDL/AN-2005 calculated cross section and direct measurements. Plot made using JANIS Web [91].

this value has been measured to be $n_{^{13}C} = 4.19 \times 10^{20}$ cm^{-3} [93]. This value is slightly larger than that of the Daya Bay scintillator of $n_{^{13}C} = 3.85 \times 10^{20}$ cm^{-3}. The result is then scaled up according to the ratio of the densities giving a probability of $6.26 \pm 0.45 \times 10^{-8}$.

The α rate multiplied by the $\alpha \rightarrow \alpha$-n conversion rate thus gives the average α-n rate to be 0.21 ± 0.02 events/day where the uncertainty is still dominated by the cross section uncertainty. The α-n rate over time differs from the α rate by simply a multiplicative factor and thus is included in the rate plot shown in Figure 6.6.

α-n Prompt Energy Spectrum

The previous calculation only predicts the total rate of α-n interactions in the SNO+ detector. Because the interaction occurs through three separate channels, the relative probability of each channel occurring and the energy deposited for each channel are necessary to predict the total energy spectrum of α-n events.

The probability of producing ^{16}O in the ground (channels 1 and 2) or excited states (channel 3) also comes from the JENDL/AN-2005 library [87]. The values used by the `RAT` simulation are summarized in Table 6.3. These probabilities have large uncertainties discussed further in Section 8.3.

State	Probability
Ground	90.8%
1^{st} Excited State	8.0%
2^{nd} Excited State	1.2%

Table 6.3: Probability of ^{16}O states being produced in α-n interaction. Only the first two excited states are accessible at the ^{210}Po α energy (5.3 MeV).

When ^{16}O is produced in the ground state, an energetic neutron is created. This neutron tends to have an energy of ~3-7 MeV. The calculation of this energy distribution used in `RAT` uses the same JENDL library and stopping power from SRIM as the $\alpha \rightarrow \alpha$-n conversion calculation from above.

After the input neutron energy distribution is used to produce a neutron, its behavior is modeled using the `GEANT-4` simulation package. This includes the behavior of the neutron as it scatters protons and the probability of the neutron inelastically scattering off ^{12}C. The modeling of the proton recoils is based on measurements made using the SNO+ scintillator in a neutron beam [93]. These measurements provide the quenching and Birks' constant of protons used in `RAT` . The inelastic scatter peak produces a 4.4 MeV de-excitation γ which is then also modeled in simulation.

The ^{210}Po α is also energetic enough to produce ^{16}O in its first or second excited state. In the first excited state, ^{16}O decays emitting an $e^+ + e^-$ pair with a total energy of 5.03 MeV. The e^+ then annihilates, creating two additional 511 keV γs bringing the total visible energy to 6.05 MeV. In the second excited state, the ^{16}O atom de-excites through a 6.13 MeV γ. These de-excitations are then modeled in simulation.

The resulting energy distribution of the α-n background in SNO+ is then shown in Figure 6.5.

α-n Delayed Event

In all three cases, after the prompt event deposits energy, a low energy neutron remains. This low energy neutron then behaves the same as the low energy neutron in the case of an IBD, capturing on hydrogen with a lifetime of ~200 μs and producing a 2.2 MeV γ. This makes it impossible to use the delayed event to distinguish between α-n and IBD events.

Surface α-n Events

In addition to the ^{210}Po decays occurring in the liquid scintillator, a significantly larger rate of ^{210}Po decays occur due to ^{210}Po impacted on the AV. The fiducial volume in this analysis was chosen in part to reduce this background to a negligible rate.

6.4.2 Geoneutrinos

The second largest background to reactor IBD events is then geoneutrinos. Geoneutrinos are $\bar{\nu}_e$ produced in radioactive decays in the crust and mantle of the Earth. Because these events are also detected via IBD interactions of $\bar{\nu}_e$, they are an irreducible background to reactor antineutrinos. The only distinguishing factor is their energy spectra.

The energy spectra of the geoneutrinos produced in several radioactive decay chains are shown in Figure 6.8. Because the IBD interaction has a threshold of 1.8 MeV, only geoneutrinos produced by the ^{238}U and ^{232}Th chains are detected. These decay chains result in the production of several $\bar{\nu}_e$ with well known energy spectra:

$$^{238}\mathrm{U} \rightarrow {}^{206}\mathrm{Pb} + 8\alpha + 6\mathrm{e}^- + 6\bar{\nu}_e \tag{6.8}$$

$$^{232}\mathrm{Th} \rightarrow {}^{208}\mathrm{Pb} + 6\alpha + 4\mathrm{e}^- + 4\bar{\nu}_e \tag{6.9}$$

Multiple geological models exist predicting the abundance of ^{238}U and ^{232}Th in the Earth's crust and mantle. The geoneutrino flux is then predicted by integrating over the volume of the Earth weighted by the abundance of each isotope and accounting for additional effects such as the ^{238}U and ^{232}Th decay rates, the energy spectra of the emitted neutrinos, the varying density of the Earth, and the distance the neutrino must travel. In addition, neutrino oscillation must be taken into account. Because the neutrinos are produced throughout the crust and mantle at a large range of distances from SNO+, the survival probability of the neutrinos can be averaged over L. The average survival probability used in the prediction is thus:

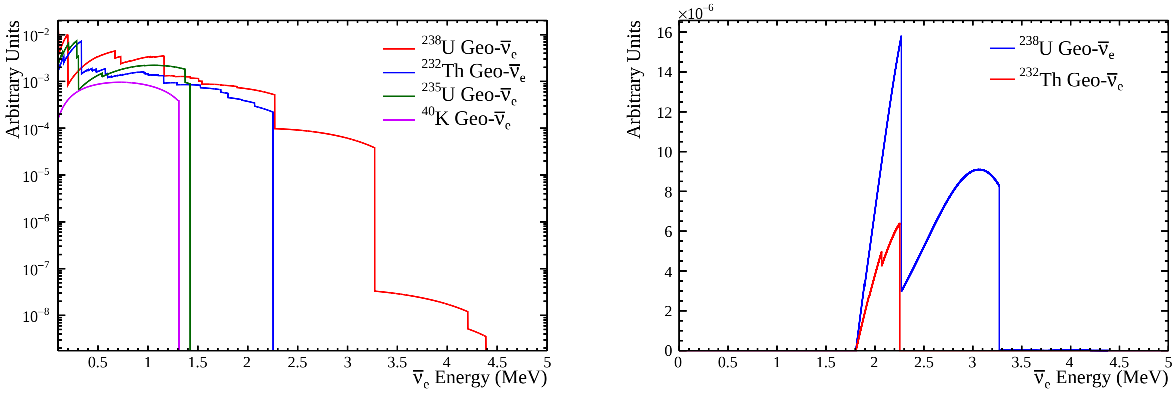

(a) (b)

Figure 6.8: $\bar{\nu}_e$ energy spectra produced by radioactive decay chains responsible for geoneutrinos. (a) The energy spectra of emitted geoneutrinos for several decay chains. (b) The expected energy spectra of detected geoneutrinos after taking the product with the IBD cross section. Only the ^{238}U and ^{232}Th chains produce neutrinos above the IBD energy threshold.

Isotope	Low Q Flux (TNU)	Mid Q Flux (TNU)	High Q Flux (TNU)
^{238}U	29.7 ± 4.7	34.1 ± 5.0	41.5 ± 5.0
^{232}Th	8.2 ± 0.7	9.5 ± 0.8	11.5 ± 0.8
Total	37.9 ± 5.3	43.6 ± 5.8	53.1 ± 5.8

Table 6.4: Geoneutrino flux predictions for three models provided by O. Šrámek to SNO+ based on the methods used in [94].

$$\langle P_{ee} \rangle = \cos^4\theta_{13}\left(1 - \frac{\sin^2(2\theta_{12})}{2}\right) + \sin^4\theta_{13} \tag{6.10}$$

The result of this calculation is then reported in units of Terrestrial Neutrino Units (TNU) which is the number of interactions per 10^{32} target protons per year. The models and predictions used in this analysis are provided by O. Šrámek, and are based on the methods used in [94]. These three models are referred to as the Low Q, Mid Q, and High Q models. The expected geoneutrino flux at SNO+ from several additional models are examined in [95]. All models examined result in predictions within the range of the Low and High Q models provided by Šrámek.

The known energy spectra of the decays in the ^{235}U and ^{232}Th are then multiplied with the IBD cross section to obtain the energy spectra of detected $\bar{\nu}_e$ at SNO+. The rate of detected geoneutrinos is then calculated in the `RAT` simulation using the Mid Q model and the number of target protons. This results in an expectation of 5.5 interactions from the ^{238}U chain, and 20 interactions from the ^{232}Th chain giving a total of 26 interactions per year at SNO+ with the energy spectra shown in Figure 6.8.

While they are a background to the measurement of Δm^2_{21} and θ_{12} using reactor antineutrinos, geoneutrinos themselves are an interesting signal as they can be used to constrain geological models of radiogenic heat production in the Earth. The KamLAND and Borexino experiments have used large liquid scintillator detectors similar to SNO+ to observe the geoneutrino flux in Japan and Italy respectively [40] [39]. With sufficient data, SNO+ will make the first observation of geoneutrinos in North America.

6.4.3 Accidental

As previously mentioned, uncorrelated or accidental backgrounds are backgrounds resulting from two unrelated signals occurring near each other in both space and time by random chance. In order to be tagged as an IBD event, the energies of the prompt and delayed events must also have similar energies to those of a reactor antineutrino interaction.

The rate of accidental backgrounds can then be calculated using a data driven method. The expected accidental rate is given by:

$$R_{\text{acc}} = r_p \cdot r_d \cdot \Delta t \cdot \epsilon_{\text{sel}} \tag{6.11}$$

where r_p is the rate of "prompt-like" events, r_d is the rate of "delayed-like" events, Δt is the selected coincidence window, and ϵ_{sel} is the selection efficiency of additional cuts.

The Δt window used is 2 ms and the rate of prompt-like and delayed-like events in data are measured in data on a run-by-run basis. The accidental rate over time is shown in Figure 6.9. The average predicted rate of accidental coincidences with no additional selection criteria is $\sim$0.5 events/day, higher than the rate of reactor antineutrinos. The selection criteria that define prompt-like and delayed-like events as well as additional selection criteria which reduce the accidental

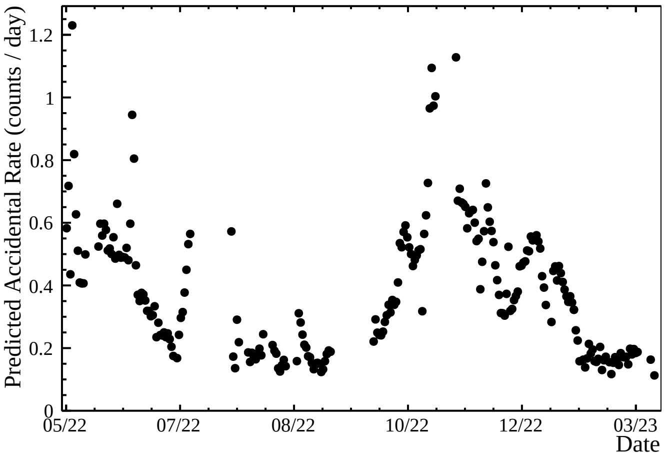

Figure 6.9: Data driven calculation of the accidental rate over time before any selection criteria are applied.

background to a negligible rate are described in Chapter 7.

6.4.4 Other Backgrounds

Atmospheric Neutrinos

Atmospheric neutrinos are produced in the decays of particles created when cosmic rays interact in the Earth's atmosphere. These neutrinos tend to have a significantly higher energy than reactor antineutrinos and interact in the detector through neutral and charged current interactions with ^{1}H, ^{12}C, and ^{13}C. While the neutrinos are typically too high in energy to be tagged as a reactor antineutrino, their interactions can produce neutrons capable of mimicking both the prompt and delayed signals.

A prediction of the rate of atmospheric neutrinos producing IBD-like coincidences was performed in the partial fill phase of SNO+ by C. Lin [96]. This study used the GENIE Monte Carlo generator to simulate a large sample of atmospheric neutrino events in the SNO+ detector. The selection criteria used to identify IBD events was then applied resulting in a negligible expectation for the atmospheric background. The rate is expected to scale with the volume for full fill, increasing the prediction by a factor of ∼2, however, this amount is still negligible.

Cosmogenic Backgrounds

The interactions of cosmic muons within the SNO+ detector can produce backgrounds to reactor antineutrinos through a few different mechanisms:

1) Production of ^{9}Li or ^{8}He in scintillator: When these nuclei are produced by muons, they undergo the following $\beta + n$ decays with half lives of 180 ms and 120 ms respectively:

$$^{9}\text{Li} \rightarrow 2\alpha + n + \bar{\nu}_e + e^- \tag{6.12}$$

$$^{8}\text{He} \rightarrow {}^{7}\text{Li} + n + \bar{\nu}_e + e^- \tag{6.13}$$

These $\beta + n$ decays are capable of mimicking the IBD signal.

2) ^{18}O(n,n+p)^{17}N interactions in the water: Muons can interact with oxygen in the external water causing this interaction. The ^{17}N also undergoes $\beta + n$ decay with a half-life of 2.9 s.

3) Production of multiple neutrons: Muons passing through the detector are capable of producing multiple neutrons which can then mimic the prompt and delayed signals.

Cuts are applied to remove events after muons and IBD candidates with more than two coincident events. These cuts are described in Chapter 7 and reduce the cosmogenic backgrounds described to a negligible level.

Sideband Events

Runs at the beginning of both the partial and full fill data sets had high rates of radioactive backgrounds but were initially included in the analysis due to the expected effect on the accidental background contribution being small. In both datasets, an excess of events in a delayed event energy sideband was observed in these runs with elevated radioactive backgrounds. These events had a reconstructed energy between 1.5 and 1.85 MeV. Figure 6.10 shows the energy distribution of all known backgrounds fit to the observed energy distribution including the sideband region. An excess of events from 1.5 to 1.85 MeV can be seen.

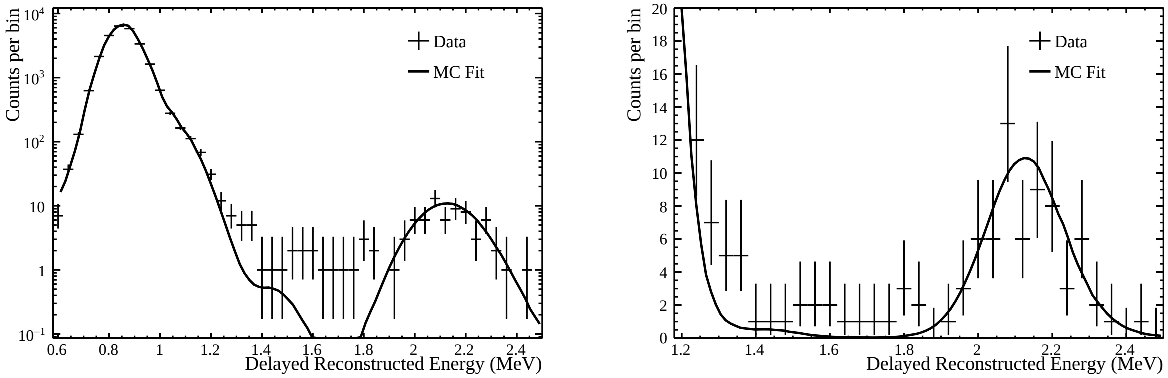

Figure 6.10: Fit of delayed energy signal and sideband region shown in both a logarithmic and linear scale. An excess of events is seen between 1.5 and 1.85 MeV.

Figure 6.11 shows the Δt and Δr distributions of these sideband events combined for both partial and full fill to increase statistics. These distributions are compared to the expectation for accidentals, neutron capture, and ^{214}BiPo decays. These distributions are clearly inconsistent with accidentals. In addition, ^{214}BiPo and neutron capture events have expected Δt and Δr distributions very similar to each other and in good agreement with these events.

Figure 6.11 then shows the position distributions of these sideband events. The events are reasonably uniform throughout the detector making them inconsistent with any background that is localized or requires effects from the choice of fiducial volume. This includes, for example, an excess of surface α-n events or effects of the neutron gamma escaping the detector without depositing all of its energy.

Figure 6.11 also shows the energy distribution of the prompt events for these sideband events. The prompt event energy distribution of these events agrees well with ^{214}Bi. However, the ^{214}Po decay is not energetic enough to produce these events with energy in the sideband region of 1.5-1.85 MeV. ^{214}Po also has a rare (0.0104% branching fraction) α-γ decay which reconstructs at a slightly higher energy than the ^{214}Po α decay. This decay causes the slight shoulder in the energy distribution from 1.4-1.6 MeV in Figure 6.10. While this decay is closer in energy to these events, its energy and expected rate is still not enough to explain these events.

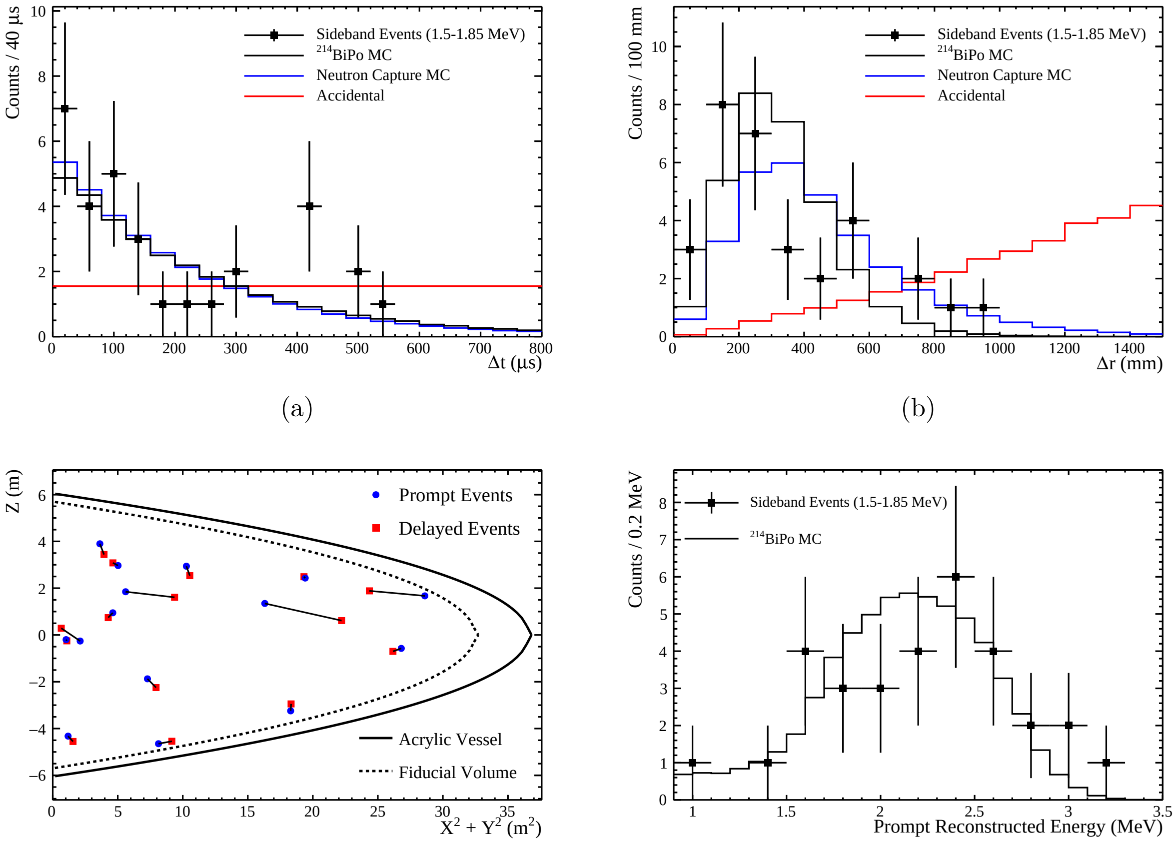

(a)

(b)

(c)

(d)

Figure 6.11: Various distribution of events in the sideband region. All distributions are in good agreement with ^{214}BiPo MC.

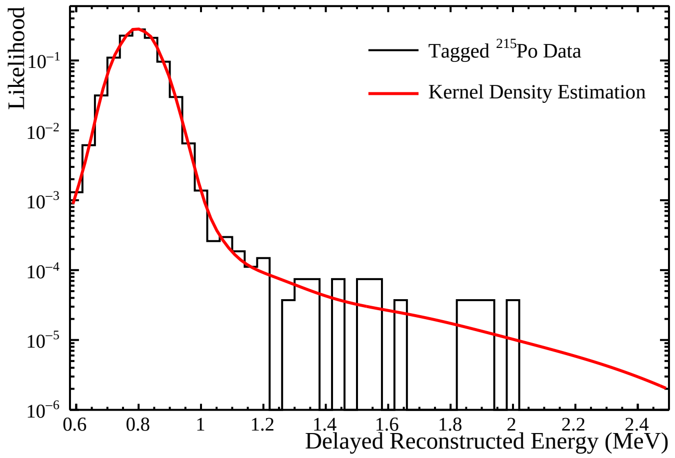

Figure 6.12: Energy distribution of tagged ^{215}Po events and the resulting PDF obtained using a kernel density estimation of the events.

A potential explanation for this increased energy is pileup of the delayed ^{214}Po events with ^{210}Po or ^{210}Bi (two of the highest rate radioactive decays). However, simulation shows that these pileup events still do not have a high enough energy, and analytical calculations of the expected pileup predict too small of a rate. In addition, a few variables are used by SNO+ to classify if pileup occurs within an event. The first, ITR (In-Time-Ratio) is defined as the fraction of hits that fall within a 7 ns window around the prompt peak, the second, the alpha-beta classifier performs a likelihood ratio test between pileup of Bi and Po events and a single $0\nu\beta\beta$ event. Both of these classifiers favored a single event over pileup for all events. Finally, the hit time residuals were inspected by eye and showed no evidence of pileup.

Another tagged alpha decay was used to investigate the possibility of a similar tail. The coincidence of ^{219}Rn and ^{215}Po decays are used to tag the 7.5 MeV α emitted in the ^{215}Po decay with a lifetime of 2.57 ms. This decay is very similar in energy to the 7.8 MeV ^{214}Po α decay however it has a significantly longer half-life which allows it to be easily distinguished from neutron capture. Figure 6.12 shows the energy distribution of tagged ^{215}Po events. A tail of events at high energy is observed. A data-driven model for these events is then obtained using a kernel density estimation of the events. This model is also shown in Figure 6.12.

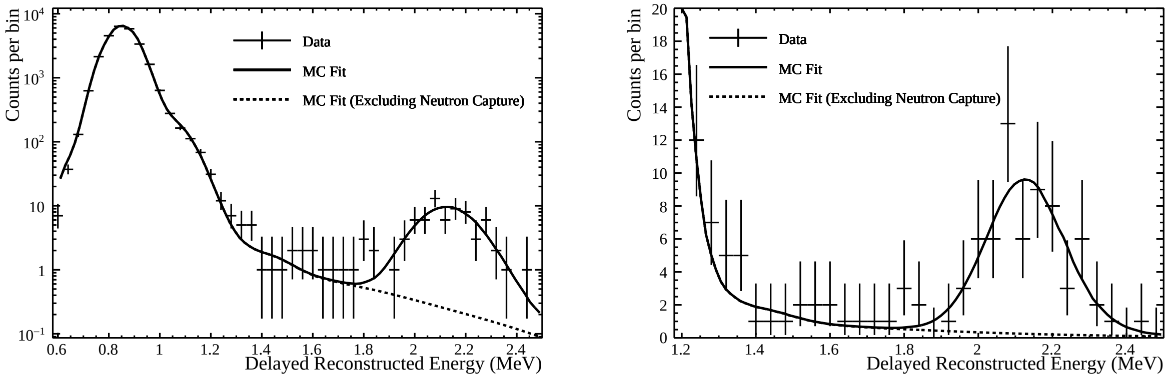

Figure 6.13: Fit of the delayed energy signal and sideband regions including known signals and additional distributions to explain the sideband events.

The ^{215}Po data driven model was then used to estimate the number of events contributing to the IBD signal region. Figure 6.13 shows the resulting sideband fit including the ^{215}Po data driven model which gives much better agreement between data and prediction. Several other physically motivated shapes were also used to estimate the number of events contributing to the signal region to give further estimates on an uncertainty. This included a decaying exponential and a Gaussian with a realistic resolution for a monoenergetic particle.

A few additional steps were taken to address this unexpected background. First, runs with high rates of ^{214}BiPo decays and other radioactive backgrounds were removed from this analysis. In addition, the energy window used to select delayed events was tightened to reduce the probability of these sideband events contributing to the signal region.

The best estimate after these steps was found to be 1.1 ± 1.1 events, a small contribution relative to the previously mentioned signal and backgrounds. This contribution is accounted for in the fit described in Chapter 8 and studies showed that this level of contribution would have a small effect on the measurement of Δm^2_{21} and θ_{12}.

Chapter 7

REACTOR ANTINEUTRINO EVENT SELECTION

Now that we have a prediction for the total number of IBD-like interactions in the detector, we can attempt to identify these interactions in data. This chapter describes the methods used to choose the data used for this analysis and to select the IBD-like interactions in this data set. Also, the selection efficiency is evaluated for all events to arrive at a prediction for the total number of observed events. Finally, the selection is applied to data and the observed events are compared with prediction.

7.1 Data Selection

The data used in this analysis was taken from April 2022 - March 2023. During this time, no filling operations were occurring, leaving the target volume in a stable state. Calibration and detector maintenance occurred regularly during this time and the data taken during these periods were not used in this analysis. In addition, many criteria are applied to physics data runs to ensure that the runs are high quality and suitable for a physics analysis. These criteria remove runs with issues such as PMT breakdowns, electronics failures, or other issues potentially harming data quality. Runs passing these criteria are referred to as "gold" physics runs.

Cut	Prompt Event	Delayed Event
Valid Fit	True	True
Data Cleaning	Pass	Pass
Radius	$R < 5.7$ m	$R < 5.7$ m
Energy	$0.9 < E < 8.0$ MeV	$1.85 < E < 2.5$ MeV
Δt	$\Delta t < 2$ ms	
Δr	$\Delta r < 2.5$ m	
Other Selection Criteria		
^{214}BiPo Tag	False	False
Muon Veto	20 s	
Muon Spallation Cut	10 μs	
Multiplicity Cut	$\mathcal{M} = 1$	
Posterior Probability Ratio	$\mathcal{P} >$ -3.5	

Table 7.1: Summary of criteria used to select IBD events.

Another criterion applied to this analysis removes runs with high rates of backgrounds. It was observed that radioactive backgrounds in the detector increased during filling operations. These backgrounds then decay away with their respective half lives after filling operations end. The selected gold physics runs included runs immediately following the end of filling operations. These runs were observed to contain a large amount of radioactive backgrounds increasing background expectations and as a result, were also removed from this analysis. After applying all data selection criteria, ~3500 high quality physics runs remain, corresponding to a total runtime of 146 days.

7.2 Event Selection

Identification of IBD-like events was performed using a two step process. First, a loose set of selection criteria was applied, then PDFs and Bayesian priors on the event rates were used to calculate a posterior probability ratio between IBD events and accidental events to further reduce backgrounds. The full selection criteria are summarized in Table 7.1.

The initial loose selection criteria require both the prompt and delayed events to have valid reconstructed values and to pass data cleaning cuts. They also require both events to reconstruct within a 5.7 m radius fiducial volume. This fiducial volume was chosen to maximize statistics while avoiding the region closest to the AV where reconstruction becomes less reliable and the rate of α-n events from surface ^{210}Po decays greatly increases.

The prompt events are required to have a reconstructed energy between 0.9 and 8.0 MeV, while delayed events require a reconstructed energy between 1.85 and 2.5 MeV. The time difference between the prompt and delayed events (Δt) as well as the distance between the reconstructed positions of the prompt and delayed events (Δr) are required to be within 2 ms and 2.5 m respectively. These selection criteria are very efficient at tagging reactor antineutrino events while backgrounds increase outside these ranges (especially accidentals below 0.9 MeV).

Several additional selection criteria are used to remove backgrounds. First, any event tagged as the prompt or delayed event of a ^{214}BiPo coincidence is removed from the data set. The removed events are the same sample of tagged ^{214}BiPo events used in the energy non-uniformity correction described in Section 4.3.6. This cut reduces the accidental background because the rate of events within the delayed event energy range is dominated by ^{214}Bi.

Three selection criteria are applied in order to remove the cosmogenic backgrounds discussed in Section 6.4.4. The first is a muon veto. This cut removes all data in the 20 seconds following any tagged muons. In addition, after applying the muon veto, all events in the 20 seconds following an event with $>$ 3000 NHits are also cut under the assumption that the high NHit event was an untagged muon or other high energy particle that could result in cosmogenic backgrounds.

Next is a muon spallation cut. The cut removes events within 10 μs of an event with 3 or more OWL PMT hits. The goal of this cut is to remove events in which a muon interacts in the cavity producing OWL hits and a high energy neutron. The high energy neutron can then travel into the detector and create both the prompt and delayed events similar to channel 1 of the α-n interaction.

The final cut is a multiplicity cut. This cut removes tagged IBD pairs where more than 2 events are in coincidence with each other. In order to be considered an additional coincidence event, an event must have a reconstructed energy $>$ 0.4 MeV and a Δr $<$ 2 m. The goal of this cut is to remove any events with multiple neutrons or any potential three-fold coincidence backgrounds. These three cuts reduce the cosmogenic backgrounds to a negligible level.

Several of the described cuts remove data from the analysis reducing the total livetime used in the analysis. This loss of livetime is calculated to be 7.84% resulting in a final total livetime of 134.4 days of data.

7.3 Likelihood Tagging Method

After the loose selection criteria are applied, an additional likelihood tagging is performed to further reduce backgrounds. This method performs a likelihood ratio test between IBD and accidental events. In this analysis, the delayed energy and a 2D PDF of Δt vs. Δr are used to calculate the likelihood of an event being a reactor IBD or an accidental. For reactor IBD events, these PDFs are produced using a `RAT` simulation accounting for all of the effects discussed in Sections 6.1 - 6.3 on a run by run basis. The reactor flux is scaled up by a factor of 30000 in these simulations to provide sufficient statistics to build the PDFs.

For accidental events, the PDFs are produced using a data driven method. For each subrun (typically ∼5 minutes of data), events passing the prompt and delayed cuts are selected. Then, prompt and delayed event candidates are paired together randomly to produce the PDFs. This method removes any real coincidences from the data. By definition, accidental events are uncorrelated in time, therefore the Δt distribution is assumed to be flat for this background. The PDFs for these variables are shown for both reactor IBD and accidental events in Figure 7.1.

In addition to the likelihood ratio test, the expected rates of reactor IBD and accidental events are known on a run by run basis. This information is incorporated into the likelihood as a Bayesian prior to produce a Posterior Probability Ratio, $\mathcal{P}$ defined as:

$$\mathcal{P} = \ln\left(\frac{\mathcal{L}_{\text{reac}}}{\mathcal{L}_{\text{acc}}}\right) + \ln\left(\frac{r_{\text{reac}}}{r_{\text{acc}}}\right) \tag{7.1}$$

where $\mathcal{L}_{\text{reac/acc}}$ is the likelihood of the event being a reactor antineutrino/accidental, and $r_{\text{reac/acc}}$ is the expected rate of reactor antineutrinos/accidentals for a given run. The accidental rate varies significantly (by a factor of ∼5) as seen in Figure 6.9 while the variations in the reactor

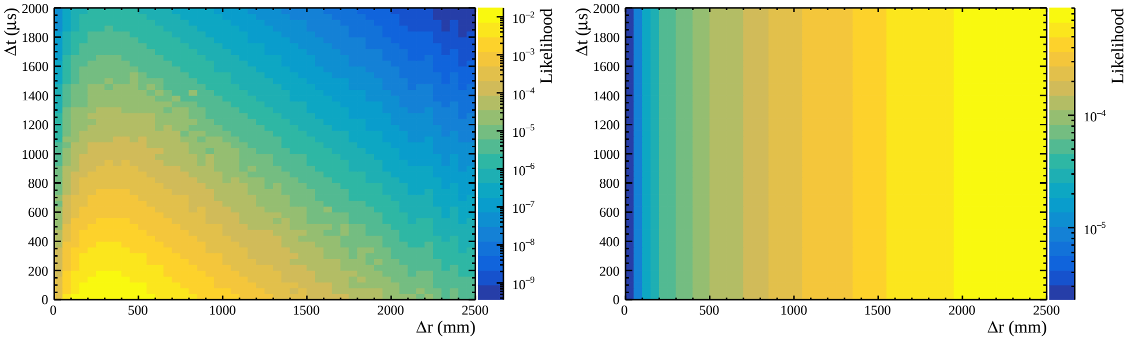

(a) Reactor $\bar{\nu}_e$ (b) Accidental

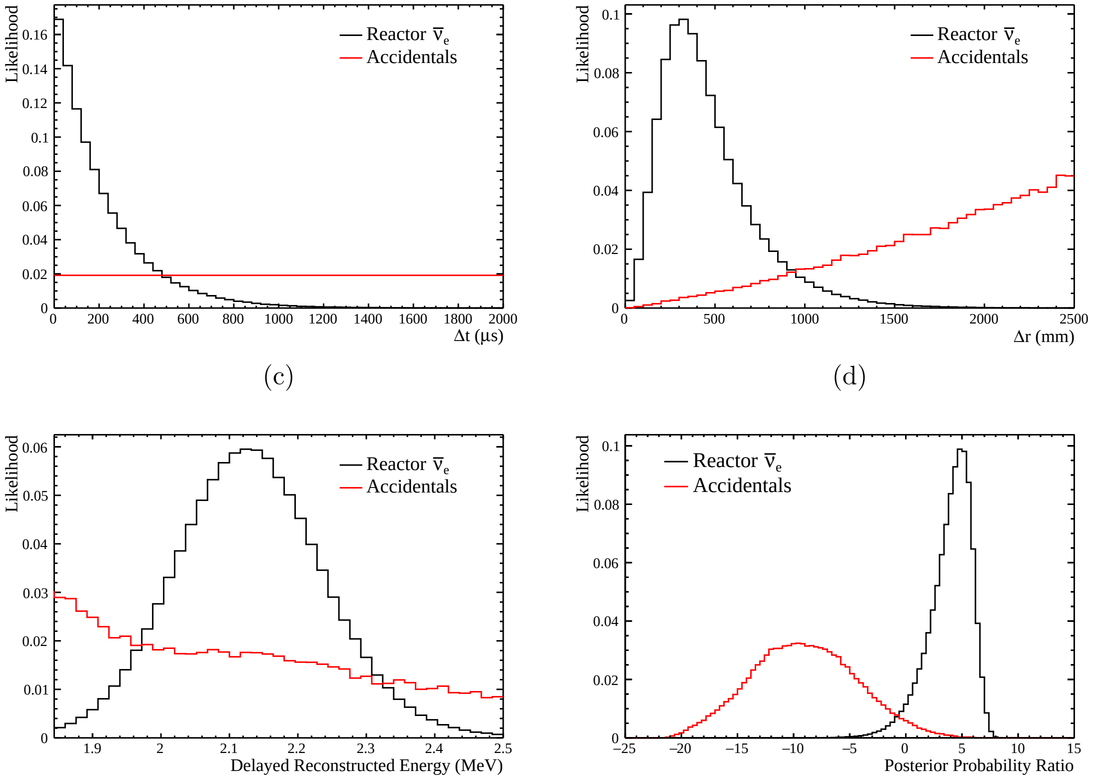

(c) (d)

(e) (f)

Figure 7.1: a,b) 2D PDFs of Δt vs. Δr for Reactor $\bar{\nu}_e$ and Accidentals. c,d) Corresponding 1D PDFs of Δt and Δr for Reactor $\bar{\nu}_e$ and Accidentals. e) Delayed energy PDFs for Reactor $\bar{\nu}_e$ and Accidentals. f) The resulting posterior probability ratio distributions for Reactor $\bar{\nu}_e$ and Accidentals.

Event Type	Full AV prediction	Selection Efficiency	Expected Events
Reactor $\bar{\nu}_e$	35.8	78%	27.9
α-n	27.3	67%	18.2
Geo $\bar{\nu}_e$	9.5	72%	6.8
Accidental	51.6	0.6%	0.3
Other			1.1
Total	124.2		54.3
Observed			59

Table 7.2: Table of predicted events before and after selection efficiency for each event type.

rate are small in comparison. The resulting Posterior Probability Ratio distribution is then shown in Figure 7.1. In this distribution, the likelihood term is the dominant effect, while the Bayesian prior term effectively results in a slightly looser or tighter cut dependent on the known event rates.

One of the benefits of this likelihood based method is that cut optimization is straightforward. The cut value used is chosen to optimize $S/\sqrt{S+B}$ where S is the expected number of signal events and B is the expected number of background events. The optimal cut is found to be $\mathcal{P}$ > -3.5.

7.4 Selection Efficiency

These sets of cuts are then applied to MC of all event types produced using the previously described `RAT` simulation to obtain the selection efficiency for events occurring within the AV. The selection efficiency and resulting prediction for each of the major signals and backgrounds are given in Table 7.2 and Figure 7.2 shows the expected energy distribution. These selection criteria greatly reduce the accidental background, while still providing a high efficiency for the reactor antineutrino signal.

7.5 Selected Reactor IBD Candidates

After all selection criteria are applied, 59 reactor IBD candidate events are observed, in good agreement with the total prediction of 54.3. The position distribution of the tagged IBD candidates is shown in Figure 7.3. The tagged events appear to be uniform throughout the detector with reasonable distances between the prompt and delayed events. This is as expected and rejects the possibility of any unknown localized background.

Several distributions are inspected comparing the observed reactor IBD events to the nominal

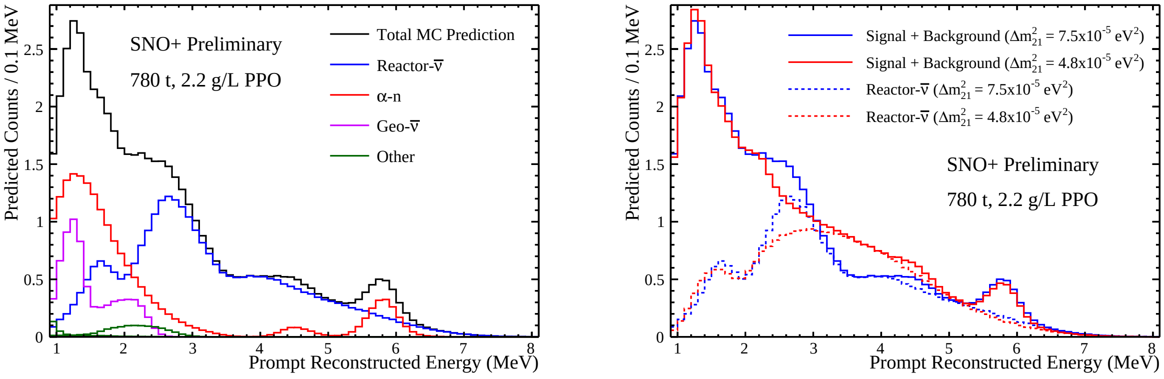

(a) (b)

Figure 7.2: Predicted energy distribution of events. (a) Shows the predicted energy distributions for each event type. (b) Shows the predicted energy distributions for two different choices of Δm^2_{21}.

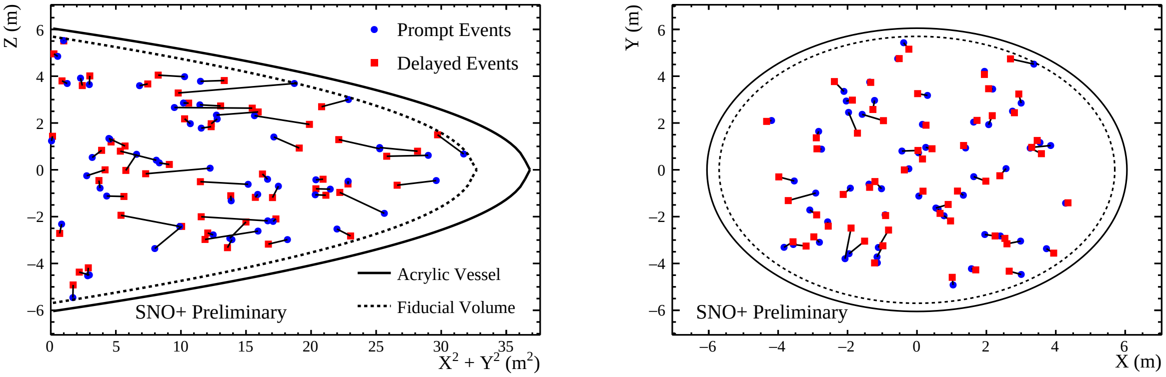

(a) (b)

Figure 7.3: Position distributions of the prompt and delayed events of selected IBD candidates.

prediction. The nominal prediction assumes the number of events shown in Table 7.2 and the PDG global fit oscillation parameters. These distributions are shown in Figure 7.4. All distributions agree well with prediction.

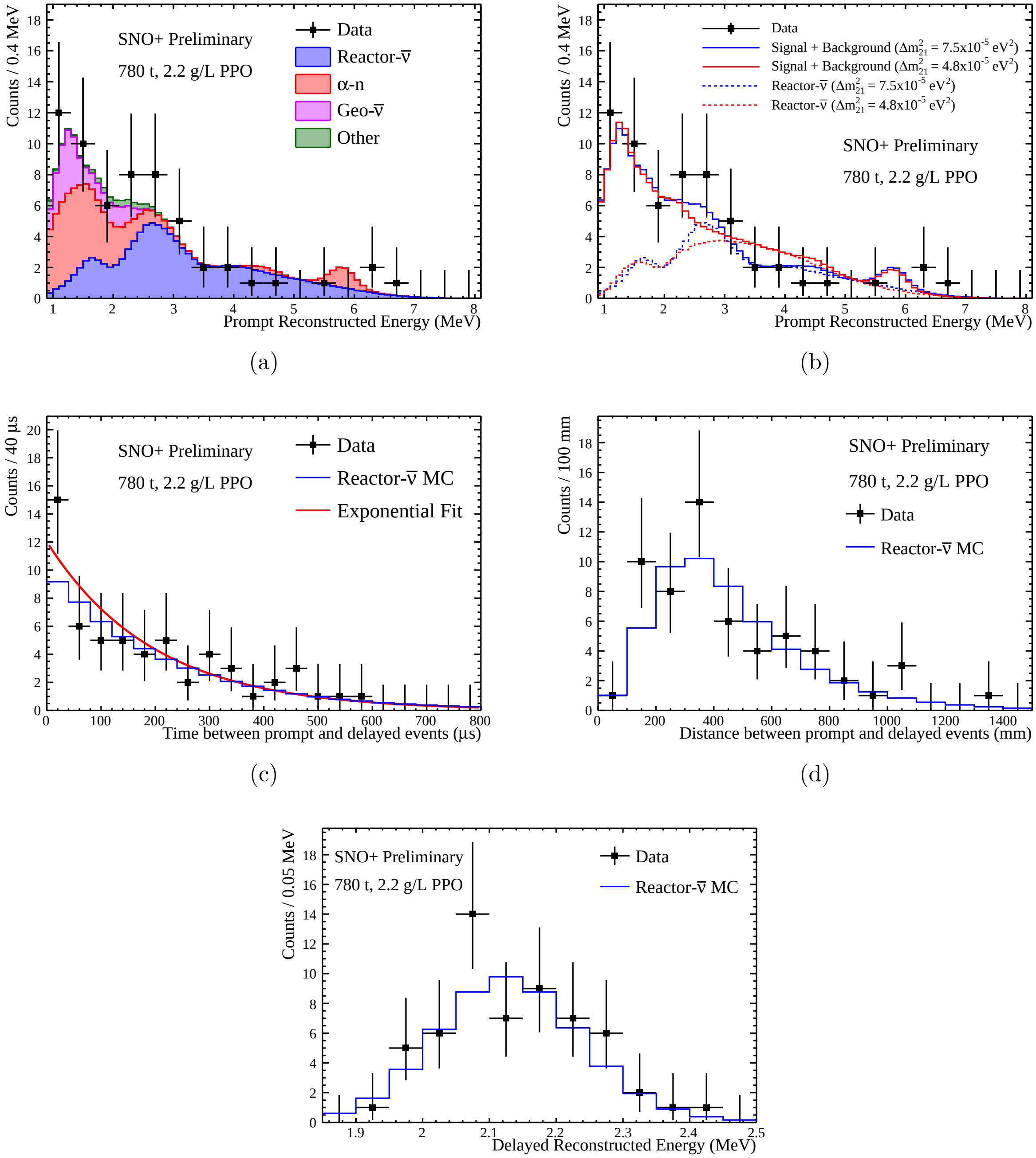

(a) (b)

(c) (d)

(e)

Figure 7.4: Distributions of selected IBD candidates compared to the nominal prediction. (a,b) Prompt energy distribution compared to expectation showing the contribution of each background and the effect of different oscillation parameters. (c,d,e) Δt, Δr, and delayed energy distributions of tagged events compared to Reactor-$\bar{\nu}_e$ (neutron capture) MC. All observed distributions agree well with prediction.

Chapter 8

REACTOR ANTINEUTRINO OSCILLATION FIT

After selecting IBD candidate events, distortions in the energy spectrum of the detected events are present. These distortions are caused by oscillation of the neutrinos to undetectable flavors and are dependent on the values of the neutrino oscillation parameters Δm^2_{21} and θ_{12}. Thus, the values of these oscillation parameters can be constrained using a spectral fit of the energy distribution. This chapter describes the analysis used to perform this measurement.

8.1 PDFs

In order to calculate the likelihood of a given event, probability density functions (PDFs) for the energy of each signal and background are needed. These PDFs describe the likelihood for an event of a given type to have a given energy. These PDFs are produced by simulating a large number of events for each event type using the previously described `RAT` simulation package. The same selection criteria applied to data is then applied to the MC.

Channel	Energy Range
Proton Recoil	E $<$ 3.4 MeV
Inelastic Scatter off ^{12}C	3.4 MeV $<$ E $<$ 5.1 MeV
Excited ^{16}O	E $>$ 5.1 MeV

Table 8.1: Energy ranges of PDFs used for each possible α-n interaction channel.

8.1.1 Reactor Antineutrino PDFs

The PDFs for reactor antineutrino events are produced using a `RAT` simulation assuming no oscillation occurs between the reactor where they were produced and the SNO+ detector. The simulated energy of the neutrino and the reactor where it was produced are saved to allow oscillation to be applied later with the user's choice of oscillation parameters.

Each reactor within 1000 km is assigned its own PDF and all reactors further than 1000 km are combined into a single PDF. A list of all reactors within 1000 km of SNO+ is given in Table A.1. For each PDF, oscillation is applied on an event by event basis taking into account the true energy of the simulated neutrino (E_ν) and the distance it traveled (L). The method used for this calculation is described in [83].

8.1.2 α-n PDFs

The PDFs for α-n backgrounds were also produced using the `RAT` simulation package. As discussed in Chapter 6, the prompt event of the α-n interaction can proceed through 3 separate channels: production of a high energy neutron causing proton recoils, inelastic scattering of a neutron off a ^{12}C nucleus, or production of an excited state of ^{16}O. Each of these interactions results in a different amount of energy deposition in the detector. In addition, the relative probabilities of each interaction are poorly constrained by existing data and predictions. Therefore, the distribution is split into three separate PDFs based on the energy of the simulated events. Table 8.1 summarizes the energy range for each process.

8.1.3 Geoneutrino PDFs

The PDFs for the geoneutrino backgrounds were also produced using the `RAT` simulation package. As discussed in Chapter 6, detectable geoneutrinos are produced in the Earth through two separate

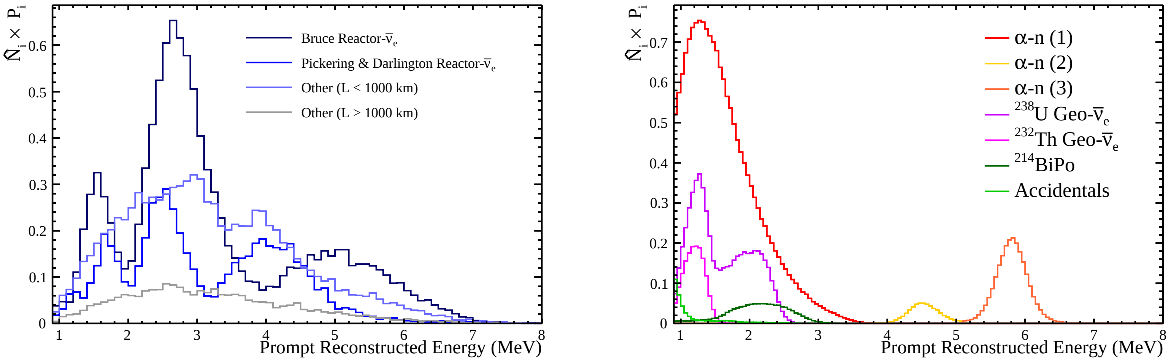

(a) Reactor $\bar{\nu}_e$ PDFs

(b) Background PDFs

Figure 8.1: PDFs used in the likelihood fit, reactors between 350 & 1000 km are combined into a single PDF.

decay chains ^{238}U and ^{232}Th. The two decay chains produce distinct energy spectra of antineutrinos and therefore are split into two separate PDFs.

8.1.4 Accidental PDF

The PDF of the accidental background was produced using the same data driven method described in Section 7.3.

The PDFs used in the fit are shown in Figure 8.1, with reactors between 350 & 1000 km combined into a single PDF.

8.2 Likelihood Fit

A binned extended maximum likelihood fit is then used to measure the oscillation parameters Δm^2_{21} and θ_{12}. The log likelihood used to determine a test statistic is defined as:

$$\begin{aligned}\ln(\mathcal{L}(\vec{n}_{\mathrm{obs}}|\Delta m^2_{21},\theta_{12})) = &\sum_{j=0}^{N_{\mathrm{bins}}} n^j_{\mathrm{obs}} \ln\left(\sum_{i=0}^{N_{\mathrm{pdfs}}} N_i(\Delta m^2_{21},\theta_{12}) P^j_i(\Delta m^2_{21},\theta_{12})\right) \\ &- \sum_{i=0}^{N_{\mathrm{nuis}}} \frac{(\mu_i-\hat{\mu}_i)^2}{2\sigma_i^2} - \sum_{i=0}^{N_{\mathrm{pdfs}}} N_i(\Delta m^2_{21},\theta_{12})\end{aligned} \tag{8.1}$$

In this equation, the first term is the likelihood, the second term is the sum of penalty terms, and the last term is the extended likelihood where N_i is the fitted number of events from each PDF contributing to the signal region. In the likelihood term, n^j_{obs} is the number of observed events in the j$^{\text{th}}$ energy bin in data, $P^j_i(\Delta m^2_{21}, \theta_{12})$ is the probability for an event drawn from the i$^{\text{th}}$ PDF to have energy in the j$^{\text{th}}$ bin given the oscillation parameters Δm^2_{21}, θ_{12}. For the penalty terms, μ_i is the fitted value of the nuisance parameter, $\hat{\mu}_i$ is the expected value of the nuisance parameter, and σ_i is the uncertainty on the expected value of the nuisance parameter.

The oscillation parameters Δm^2_{21} and θ_{12} are the parameters of interest while all other parameters are treated as nuisance parameters. These nuisance parameters include:

- Normalization of Reactor PDFs
- Normalization of Geoneutrino, α-n, and Accidental PDFs
- Ratio of U:Th Geoneutrino Rate
- Systematic Uncertainty Parameters

While they are treated as nuisance parameters in the fit, the values of some of these parameters are also of interest and will be examined later. All parameters are described in detail in Section 8.3.

A grid search is performed over the relevant values of the fit parameters Δm^2_{21} and θ_{12}. For each fixed value of Δm^2_{21} and θ_{12}, the nuisance parameters are varied to find the minimum value of $-\ln \mathcal{L}$. The minimum value of -ln $\mathcal{L}$ across all values of Δm^2_{21} and θ_{12} is thus the best fit value. After the global best fit values are found, a much finer grid scan is run around these values to obtain more precise estimates of the parameters and their uncertainties. A likelihood ratio between this best fit value and the value of $\mathcal{L}$ at each point is then taken:

$$\Delta \ln(\mathcal{L}(\Delta m^2_{21}, \theta_{12})) = \ln \left(\frac{\mathcal{L}(\Delta m^2_{21}, \theta_{12})}{\mathcal{L}(\Delta \widehat{m}^2_{21}, \widehat{\theta}_{12})} \right) \tag{8.2}$$

where $\Delta\widehat{m}_{21}^2$ and $\widehat{\theta}_{12}$ are the best fit values of Δm_{21}^2 and θ_{12}. By Wilks' Theorem [97], the value -$2\Delta\log(\mathcal{L})$ is distributed as a χ^2 distribution and can be used as a test statistic to compare the goodness of fit between two sets of oscillation parameters.

8.3 Systematic Uncertainties

The dominant systematic uncertainties are estimated and included in the fit as nuisance parameters. The relatively small expected number of signal events results in relatively large statistical uncertainties. Thus, for the data sample used in this analysis, systematic uncertainties are expected to be small in comparison. However, SNO+ will continue taking data, decreasing the statistical uncertainties in future analyses and requiring systematic uncertainties to be estimated to project the future sensitivity of the experiment.

Two types of uncertainties are included in the fit through the penalty terms: normalization uncertainties and shape uncertainties.

8.3.1 Normalization Uncertainties

Normalization uncertainties affect the number of expected events from each event type and are summarized in Table 8.3. Chapters 6 and 7 describe the prediction for detected event rates in the SNO+ detector in detail. The following sections describe the uncertainties on these rates.

Reactor Antineutrinos

Several different factors contribute to the uncertainty on the expected number of detected antineutrinos. The Daya Bay experiment has made detailed measurements of the reactor antineutrino flux [82]. These measurements provide several sources of uncertainty that affect the expected rate. This includes uncertainties on the rate of 2.4% due to uncertainties in the emitted antineutrino energy spectrum, 0.6% due to uncertainties in the fraction of fissile isotopes, 0.5% due to uncertainties in the reactor power production, and several other smaller sources.

In addition, the two sources (IESO and IAEA) used to obtain the thermal power output of the reactors were found to have differences of up to 1.0% in the reported thermal powers. This value was taken as an uncertainty on the reactor normalization. Also, the uncertainty from the prior

Source	Uncertainty
Emission Spectrum	2.4%
IESO vs. IAEA Power	1.0%
Fission Fraction	0.6%
Reactor Power	0.5%
Target Protons	0.5%
IBD Cross Section	0.4%
Spent Fuel	0.3%
Non-equilibrium	0.2%
Energy/Fission	0.2%
Fixed θ_{13}	0.14%
Total	2.8%

Table 8.2: Sources contributing to the uncertainty on the reactor antineutrino normalization.

target proton calculation of 0.5%, where the dominant uncertainty is assumed to be the variation in temperature across the detector is also used. Finally, fixing oscillation parameters other than Δm^2_{21} and θ_{12} when performing the fit results in an uncertainty on the expected reactor flux. Propagation of the measured error on θ_{13} results in a 0.14% uncertainty on the average survival probability of reactor antineutrinos.

The full list of sources of uncertainty on the antineutrino flux is summarized in Table 8.2. The dominant uncertainty comes from the emitted antineutrino spectrum which is a property of the fissile isotopes and thus correlated across all reactors. For this reason, the full uncertainty is treated as correlated in the fit. Combining these sources of uncertainty gives a total uncertainty on the reactor antineutrino normalization of 2.8%.

α-n

The normalizations of the α-n PDFs were predicted using the JENDL/AN-2005 calculation of the α capture cross section [91]. Several direct measurements of the cross section have also been made [98], [89], [88]. The JENDL/AN-2005 calculation and direct measurements have significant disagreements requiring a systematic for the total cross section of the α-n interaction.

The KamLAND experiment used the measurement from Harissopulos et. al [98] to predict the total cross section of the α-n interaction. In addition, a ^{210}Po^{13}C calibration source was used to tune the relative normalizations of the ground and excited states of the reaction [99]. KamLAND's analysis found the scalings needed for the ground, first, and second excited states were 1.05, 0.6, and 1.0 respectively. KamLAND's calibration also required additional uncertainties of 11% for the ground state and 20% for the excited state.

In this analysis, we assign conservative uncertainties on the total and relative normalizations of the different α-n interaction channels. These uncertainties cover both the disagreements between the JENDL/AN-2005 calculation and total cross section measurements as well as the additional scalings found by the KamLAND experiment. For the proton recoil and inelastic scatter channels, 30% uncertainties are assigned, and for the excited ^{16}O channels a 100% uncertainty is assigned.

Geoneutrinos

Because the total geoneutrino flux is poorly constrained by geological models and existing measurements, no constraint is applied. This allows the geoneutrino flux to be treated as a signal and measured in the fit. Geological models do have constraints on the relative contributions of the ^{238}U and ^{232}Th chains. These models constrain the ^{238}U:^{232}Th ratio to be 3.7±1.3 [95] and this constraint is applied as a pull term in the fit.

Sideband Events

In addition to the expected backgrounds, additional events were observed in the sideband of the delayed energy as described in Section 6.4.4. The rate of these events was significantly higher in runs with high rates of ^{214}BiPo decays. In addition, these events were found to have position, Δt, Δr, and prompt energy distributions in good agreement with ^{214}BiPo events. As a result, the prompt energy of these events was modeled as prompt ^{214}Bi decays. As mentioned in Section 6.4.4, the prediction and uncertainty obtained from a data driven model and several empirically chosen, physically motivated models is 1.1 ± 1.1 events.

8.3.2 Shape Uncertainties

Shape uncertainties affect the shape of the energy distribution and are summarized in Table 8.4. These uncertainties are important because their effect may mimic the effect of a different choice

Parameter	Uncertainty (σ_i/μ_i)
Reactor Normalization	2.8%
α-n Proton Recoil Normalization	30%
α-n Inelastic Scatter Normalization	30%
α-n Excited ^{16}O Normalization	100%
Geoneutrino Normalization	-
^{238}U:^{232}Th Ratio	35%
Sideband Event Normalization	100%

Table 8.3: Table of normalization uncertainties.

of oscillation parameters. The dominant shape uncertainties are those associated with the energy reconstruction. Section 4.3 describes the calibration and associated systematic uncertainties. Uncertainties associated with position reconstruction were found to be negligible.

Uncertainties in the energy reconstruction manifest as differences between the energy distributions for data and MC. To account for these uncertainties, transformations are applied to the MC PDFs used in the likelihood fit to improve the agreement. Each transformation is described by a parameter that is constrained by independent measurements. These constraints are included in the likelihood fit as penalty terms in Equation 8.2.

Three transformations are applied to the energy distribution to account for these discrepancies. An energy scaling, an energy smearing (resolution), and a nonlinear energy scale. Each transformation is a function that produces a new PDF from the original.

Because the analysis uses binned likelihoods, the transformations are applied using distortion matrices:

$$P'(E_i) = M_{ij}P(E_j) \tag{8.3}$$

where the M_{ij} represents the fraction of energy bin j that contributes to energy bin i after the transformation. The transformed PDFs $P'(E_i)$ are then used as the $P_i^j(\Delta m^2_{21}, \theta_{12})$ when calculating the likelihood using Equation 8.2.

Energy Scale

The first systematic is the energy scaling. The transformation applies a constant scale to the energy of events as:

$$P'(E) = P(c \cdot E) \tag{8.4}$$

This systematic is constrained to be $c = 1 \pm 0.018$ using tagged ^{214}BiPo events as described in Section 4.3.6.

In addition, all but one PDF comes from events where the detected particles are either βs or γs. The behavior of βs or γs is assumed to be similar enough to be treated identically. The α-n proton recoil PDF comes from detected protons and therefore may have a different energy scaling from βs and γs. To account for this, an additional energy scaling is applied only to the α-n proton recoil PDF.

Energy Resolution

The next systematic is the energy resolution. This transformation applies a smearing to the energy distribution by convolving the distribution with a Gaussian as:

$$P'(E) = \int P(E') \left(\frac{1}{\sigma\sqrt{2\pi}} e^{(E-E')^2/2\sigma^2} \right) dE' \tag{8.5}$$

This systematic is constrained to be $\sigma < 0.044\sqrt{E}$ using tagged ^{214}BiPo events as described in Section 4.3.6.

Energy Non-linearity

The final systematic is the energy non-linearity. This transformation applies a non-linear energy scaling as:

Parameter	Uncertainty (σ_i/μ_i)
Energy Scale	1.8%
Energy Resolution	4.4% $\times\sqrt{\mathrm{E}}$
Energy Nonlinearity	5.4%
Proton Recoil Energy Scale	3.0%

Table 8.4: Table of Shape Uncertainties.

$$P'(E) = P\left(\frac{1 + k_B E}{1 + k'_B E} \times E\right) \tag{8.6}$$

This form is motivated by Birks' law:

$$\frac{dL}{dx} = S \frac{\frac{dE}{dx}}{1 + k_B \frac{dE}{dx}} \tag{8.7}$$

and is chosen to represent the expected transformation if the value of Birks' constant k_B used in simulation differed from its actual value. The value of k'_B is constrained to be 0.074 ± 0.004 based on various measurements of Birks' constant [93] [100] [101] [102].

All shape uncertainties are summarized in Table 8.4.

8.4 Fitting Framework

The fitting framework for this analysis implements the fit described in this chapter. It is written in C++ and uses the MINUIT package [103] to minimize $-\ln(\mathcal{L})$ and estimate parameter uncertainties at each point in the grid scan of Δm^2_{21} and θ_{12}.

8.5 Expected Sensitivity

With the described fitting framework as well as predictions and PDFs for the expected events, it is now possible to produce an expectation for the sensitivity to the oscillation parameters Δm^2_{21} and θ_{12}. An Asimov data set is a representative data set used to estimate the experimental sensitivity of a measurement [104]. This data set is created by scaling the MC data sets to their expected normalizations in data. The result when applying the fitting framework to an Asimov data set can

Parameter	Expected Value	Asimov Dataset Result
Δm^2_{21}	7.53×10^{-5} eV^2	$7.5 \pm 0.8 \times 10^{-5}$ eV^2
θ_{12}	33.6°	$\theta_{12} > 22.7°$
U Geoneutrinos	5.36	5.3 ± 5.1
Th Geoneutrinos	1.44	1.4 ± 1.4
Proton Recoil Relative Normalization	0.86	0.86 ± 0.25
^{14}C Inelastic Scatter Relative Normalization	0.028	0.028 ± 0.008
Excited ^{16}O Relative Normalization	0.12	0.12 ± 0.077

Table 8.5: Expected sensitivities to parameters in 134.4 day data set.

be shown to approximate the median expected sensitivity of the measurement [104].

The Asimov data set is created using the predicted event counts in Table 7.2, and the PDFs shown in Figure 7.2. This data set is thus representative of the 134.4 day livetime data set used in this analysis. The fitting framework described in this chapter is then applied to obtain the result shown in Figure 8.2.

The fit correctly estimates the best fit values of Δm^2_{21} and θ_{12} to be within the same bin as the PDG values used as inputs to the simulation: 7.53×10^{-5} eV^2 and 33.6° respectively. This fit also estimates the median 1σ error for Δm^2_{21} to be 0.8×10^{-5} eV^2, however it predicts that some values of Δm^2_{21} outside this region are allowed within 1σ.

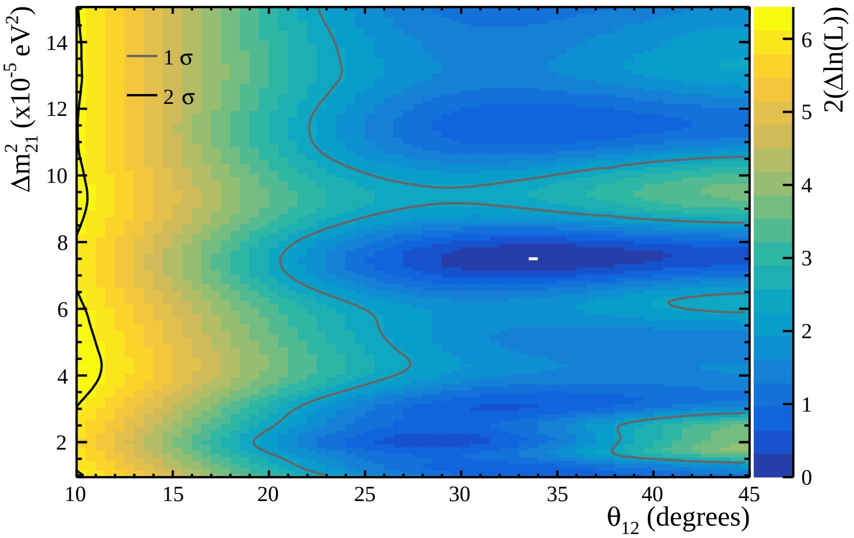

(a) Likelihood space for Asimov data set

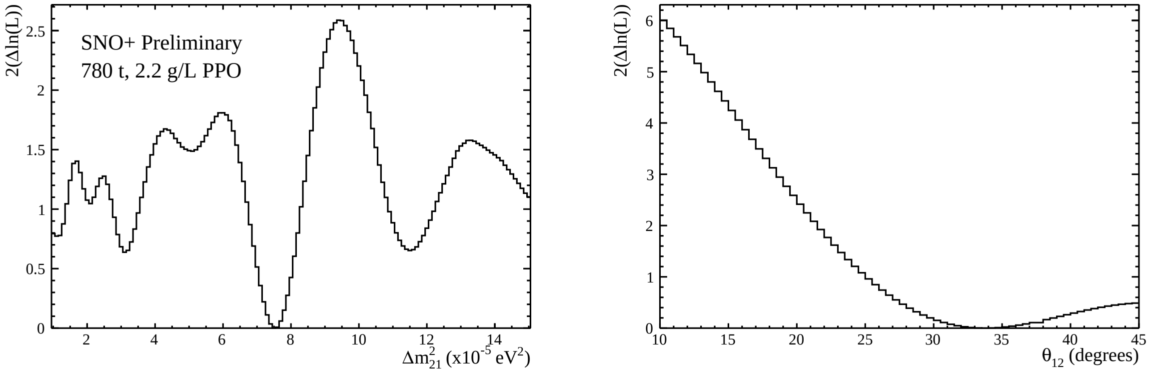

(b)

(c)

Figure 8.2: Expected sensitivity using an Asimov data set. (a) Shows the 2D likelihood space and 1 and 2 σ contours. The white bin is the best fit values of $\Delta m^2_{21} = 7.5 \times 10^{-5}$ eV^2 and $\theta_{12} = 33.5°$ (b) Shows the slice of the likelihood space at the PDG best fit value for $\theta_{12} = 33.6°$. (c) Shows the slice of the likelihood space at the PDG best fit value for $\Delta m^2_{21} = 7.53 \times 10^{-5}$eV^2.

Chapter 9

RESULTS AND FUTURE PROSPECTS

This chapter now describes the result obtained for Δm^2_{21} after applying the fit described in Chapter 8. The result is then compared to existing measurements of Δm^2_{21}. In addition, future improvements to the analysis are discussed, and projected sensitivities in the SNO+ experiment with additional data are presented. Sensitivities and future prospects of both oscillation parameter measurements and geoneutrino detection are discussed.

9.1 Results

The results of the fit are reported under three separate conditions. First, with no external constraints on Δm^2_{21} or θ_{12}, then with a Gaussian constraint on θ_{12} according to the PDG best fit result of $\sin^2(\theta_{12}) = 0.307 \pm 0.013$, and finally with Gaussian constraints on both Δm^2_{21} and θ_{12} according to the current PDG best fit result ($\Delta m^2_{21} = 7.53 \pm 0.18 \times 10^{-5}$ eV^2).

The best fit to the data and resulting likelihood space with no external constraints is shown in Figure 9.1. The resulting best fit parameters are summarized in Table 9.1. Applying the fit to data gives a result of $\Delta m^2_{21} = 7.96^{+0.48}_{-0.41} \times 10^{-5}$ eV^2 at the best fit value of $\theta_{12} = 40°$. Local minima

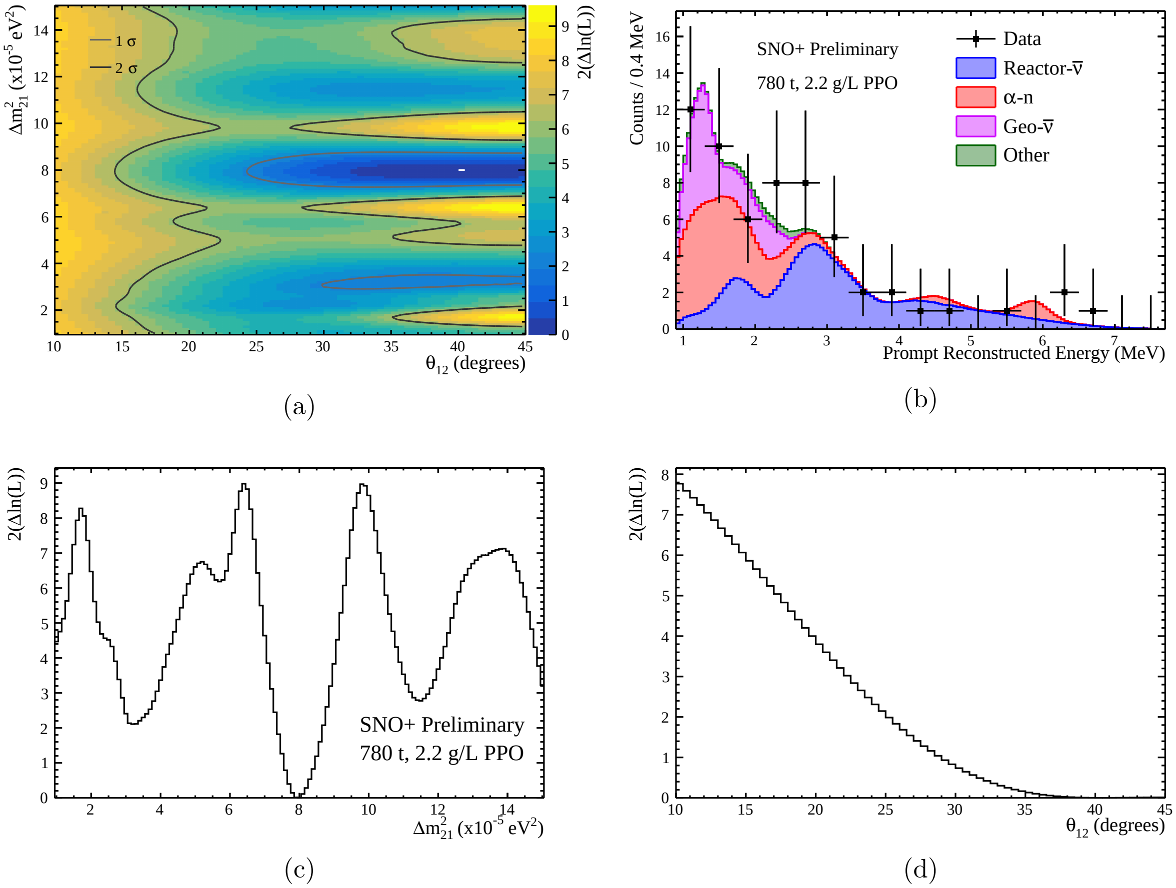

(a) (b)

(c) (d)

Figure 9.1: Results with current data set. (a) Shows the 2D likelihood space and 1, 2, and 3 σ contours. The white bin is the best fit values of $\Delta m^2_{21} = 7.95 \times 10^{-5}$ eV^2 and $\theta_{12} = 40°$ (b) Shows the fit as a stacked histogram compared to the observed data points (c) Shows the slice of the likelihood space at the best fit value for $\theta_{12} = 40°$. (d) Shows the slice of the likelihood space at the best fit value for $\Delta m^2_{21} = 7.95 \times 10^{-5}$ eV^2.

in the likelihood space appear at $\Delta m^2_{21} = 3.2 \times 10^{-5}$ eV^2 and 11.5×10^{-5} eV^2 and are disfavored at 1.5 and 1.7 σ respectively. The data is not sufficiently sensitive to θ_{12} to obtain a 1σ error, however, the 90% confidence interval is $\theta_{12} > 22°$. All of the fitted parameters summarized in Table 9.1 are in good agreement with expectation. This result also favors the best fit value over the case of no oscillation at 3.3σ.

When applying the constraint on θ_{12}, the best fit value of Δm^2_{21} is $\Delta m^2_{21} = 7.95^{+0.55}_{-0.46} \times 10^{-5}$ eV^2. Because of the limited statistics and therefore poor sensitivity to θ_{12} in this dataset, the fit combined

Parameter	Expected Value	Result (Unconstrained)
Δm^2_{21}	7.53×10^{-5} eV^2	$7.96^{+0.48}_{-0.41} \times 10^{-5}$ eV^2
θ_{12}	33.6°	40° ($\theta_{12} > 22.0^\circ$)
Total Reactor Antineutrinos	27.9	24.9 ± 0.7
Total Geoneutrinos	6.8	10.9 ± 6.9
U Geoneutrinos	5.36	8.6 ± 5.5
Th Geoneutrinos	1.44	2.3 ± 1.5
U/Th Ratio	3.7	3.8 ± 1.3
Total α-n	19.8	18.4 ± 4.7
Proton Recoil Relative Normalization	0.86	0.90 ± 0.24
^{14}C Inelastic Scatter Relative Normalization	0.028	0.028 ± 0.008
Excited ^{16}O Relative Normalization	0.12	0.073 ± 0.078
Sideband Background Normalization	1.1	1.2 ± 1.1
Energy Scale	0	$0.5 \pm 1.5\%$
Energy Resolution	0	$0.0 \pm 5.1\%$
Energy Nonlinearity	0.074	0.072 ± 0.003
Proton Recoil Energy Scale	0	$0.0 \pm 1.5\%$

Table 9.1: Best fit parameters in the 134.4 day data set with no external constraints. All parameters are in good agreement with expectations.

with the PDG constraint of θ_{12} is dominated by the constraint, giving the best fit $\theta_{12} = 33.5^\circ$. When applying the constraints on both θ_{12} and Δm^2_{21}, the best fit result obtained is $\Delta m^2_{21} = 7.59^{+0.18}_{-0.17} \times 10^{-5}$ eV^2.

The results of these fits are shown in Figures 9.2 and 9.3 and summarized in Table 9.2. Again, all the fitted parameters are in good agreement with expectation. Of particular note, is the results for the detected geoneutrinos. With both Δm^2_{21} and θ_{12} constrained, the total fitted number of geoneutrinos is 9.9 ± 6.9, slightly higher than the expected 6.8 but still in good agreement. This value corresponds to a geoneutrino flux of 64 ± 44 TNU which is within 1σ of all three geoneutrino flux models discussed in Chapter 6. Also notable is the relative normalizations of the 3 separate α-n channels, which are found to be in good agreement with expectation.

9.2 Comparison of Results

Two types of experiments have notable sensitivity to Δm^2_{21}, solar and reactor experiments. The global solar value of Δm^2_{21} comes from an analysis performed by the SuperK collaboration combining results from all available solar experiments: SuperK [42], SNO [105], Borexino [106], the Homestake

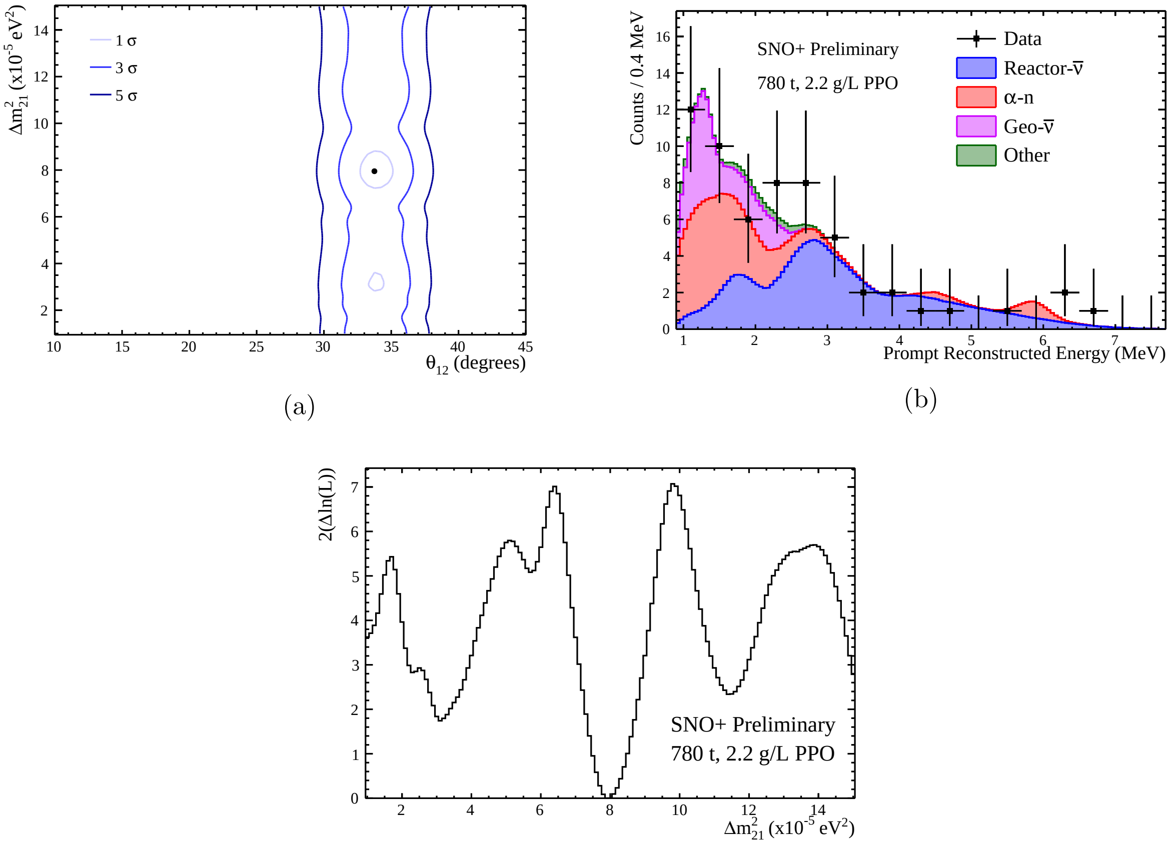

(a)

(b)

(c)

Figure 9.2: Results with current data set and a Gaussian constraint on θ_{12} ($\sin^2(\theta_{12}) = 0.307 \pm 0.013$). (a) Shows the 1, 3, and 5 σ contours. The point is the best fit values of $\Delta m^2_{21} = 7.95 \times 10^{-5}$ eV^2 and $\theta_{12} = 33.5°$ (b) Shows the fit as a stacked histogram compared to the observed data points (c) Shows the slice of the likelihood space at the best fit value for $\theta_{12} = 33.5°$.

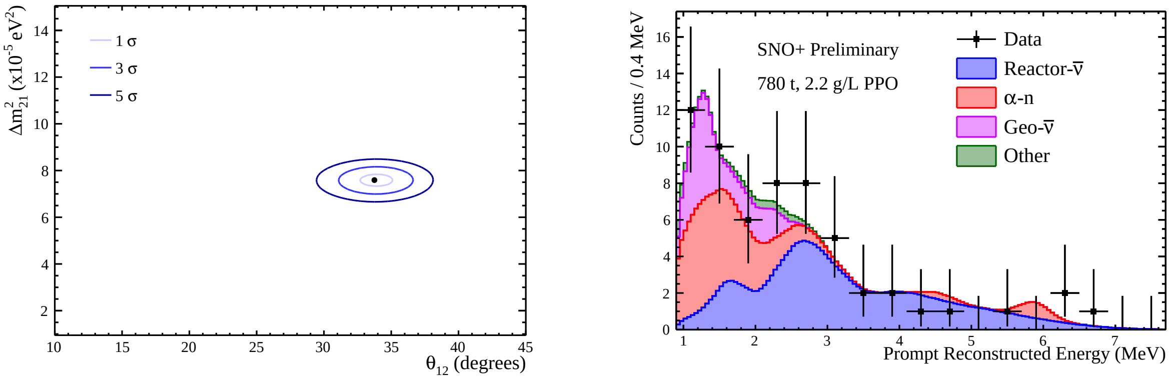

(a)

(b)

Figure 9.3: Results with current data set with both Δm^2_{21} and θ_{12} constrained ($\sin^2(\theta_{12}) = 0.307 \pm 0.013$ and $\Delta m^2_{21} = 7.53 \pm 0.18 \times 10^{-5}$ eV^2. (a) Shows the 1, 3, and 5 σ contours. The point is the best fit values of $\Delta m^2_{21} = 7.59 \times 10^{-5}$ eV^2 and $\theta_{12} = 33.5°$ (b) Shows the fit as a stacked histogram compared to the observed data.

Parameter	Result (θ_{12} Constrained)	Result (Δm^2_{21} & θ_{12} Constrained)
Δm^2_{21}	$7.95^{+0.55}_{-0.46} \times 10^{-5}$ eV^2	$7.59^{+0.18}_{-0.17} \times 10^{-5}$ eV^2
θ_{12}	$33.6 \pm 0.8°$	$33.6 \pm 0.8°$
Total Reactor Antineutrinos	28.0 ± 0.8	28.0 ± 0.8
Total Geoneutrinos	10.1 ± 6.9	9.9 ± 6.9
U Geoneutrinos	8.0 ± 5.4	7.8 ± 5.4
Th Geoneutrinos	2.1 ± 1.5	2.1 ± 1.5
U/Th Ratio	3.7 ± 1.3	3.7 ± 1.3
Total α-n	18.2 ± 4.8	18.4 ± 4.7
Proton Recoil Relative Normalization	0.90 ± 0.25	0.91 ± 0.24
^{14}C Inelastic Scatter Relative Normalization	0.028 ± 0.008	0.028 ± 0.008
Excited ^{16}O Relative Normalization	0.068 ± 0.080	0.066 ± 0.080
Sideband Background Normalization	1.2 ± 1.1	1.2 ± 1.1
Energy Scale	$0.4 \pm 1.5\%$	$0.6 \pm 1.5\%$
Energy Resolution	$0.0 \pm 5.2\%$	$0.0 \pm 8.3\%$
Energy Nonlinearity	0.072 ± 0.003	0.072 ± 0.002
Proton Recoil Energy Scale	$0.0 \pm 1.4\%$	$0.0 \pm 1.0\%$

Table 9.2: Best fit parameters in the 134.4 day data set with external constraints applied to θ_{12} and Δm^2_{21}. All fitted parameters are in good agreement with expectation.

Experiment	Result ($\times 10^{-5}$ eV^2)
KamLAND + Solar	7.53 ± 0.18
KamLAND	$7.54^{+0.19}_{-0.18}$
All Solar	$4.8^{+1.3}_{-0.6}$
This Result (Unconstrained)	$7.96^{+0.48}_{-0.41}$
This Result (θ_{12} Constrained)	$7.95^{+0.55}_{-0.46}$
This Result (Δm^2_{21} & θ_{12} Constrained)	$7.59^{+0.18}_{-0.17}$

Table 9.3: Comparison of existing measurements of Δm^2_{21}.

experiment [107], Gallex/GNO [108], and SAGE [109]. The reported result from all solar neutrino experiments is $\Delta m^2_{21} = 4.8^{+1.3}_{-0.6} \times 10^{-5}$ eV^2 [42]. The only experiment that has currently measured Δm^2_{21} using reactor antineutrinos is the KamLAND experiment, making this result the second measurement of its kind. KamLAND obtained a value of $\Delta m^2_{21} = 7.54^{+0.19}_{-0.18} \times 10^{-5}$ eV^2 [36]. In addition, a global fit performed by the KamLAND experiment is dominated by the KamLAND data giving $7.53 \pm 0.18 \times 10^{-5}$ eV^2. The combined solar result is in slight tension with the presented result at 1.4σ as well as the KamLAND and current global fit result at $\sim 2\sigma$. The KamLAND and global fit results are in reasonable agreement with this result at $\sim 0.95\sigma$. These results are summarized in Table 9.3.

While at the 1σ confidence level, this result is the second most precise measurement of Δm^2_{21}, it is important to note that the local minima in the likelihood space allow different values of Δm^2_{21} at $< 2\sigma$ and none of the trialed values of Δm^2_{21} are excluded at 3σ. The local minima at $\Delta m^2_{21} = 3.2 \times 10^{-5}$ eV^2 and 11.5×10^{-5} eV^2 are however already excluded at a high confidence level by the existing KamLAND result.

This result (along with the result presented in I. Semenec's thesis [95] using SNO+ data from the same time period) is also the first measurement of geoneutrinos in North America. While the result has limited sensitivity due to low statistics of observed geoneutrinos, the measured value of 64 ± 44 TNU is in good agreement with existing geological models.

Two previous experiments, KamLAND and Borexino, have also measured the geoneutrino flux

Experiment/Model	Flux (TNU)
Low Q	37.9 ± 4.7
Mid Q	43.6 ± 5.8
High Q	53.1 ± 5.8
KamLAND	$28.6^{+5.1}_{-4.8}$
Borexino	$47.0^{+8.4}_{-7.7}(\text{stat})^{+2.4}_{-1.8}(\text{syst})$
This Result (θ_{12} & Δm^2_{21} Constrained)	64 ± 44

Table 9.4: Comparison of existing measurements of geoneutrinos and theoretical predictions.

in Japan and Italy respectively [40] [39]. The results provide measurements of the flux of $28.6^{+5.1}_{-4.8}$ TNU and $47.0^{+8.4}_{-7.7}(\text{stat})^{+2.4}_{-1.8}(\text{syst})$ TNU respectively. The geoneutrino flux at a given location varies based on the amount of geoneutrinos produced by the local crust. As a result, differences in the measured flux at different locations are expected and give insight into the crustal contribution to the geoneutrino flux. The result obtained for the geoneutrino flux at SNO+ is again slightly higher than the previous measurements but still within 1σ due to the large uncertainties. These results are summarized in Table 9.4.

9.3 Future Improvements

9.3.1 α-n - IBD Classifier

As mentioned in Section 4.2.4, SNO+ collaborators have developed a classifier designed to distinguish between the prompt proton recoils of α-n events and the prompt positron of IBD events. The classifier relies on the hit time residuals to distinguish between these events and requires good agreement between data and simulation to be applied. At the time of writing, the hit time residuals of proton recoil events and therefore the results of this classifier were not fully calibrated, preventing its use in this analysis.

In the partial fill data set, this classifier was calibrated using an AmBe calibration source and the results are shown in Figure 9.4. The classifier was predicted to remove 70% of α-n events while retaining 93% of IBD events and good agreement was seen between the MC prediction and data. Additional work by J. Page has shown improved performance of the α-n - IBD classifier [110] in

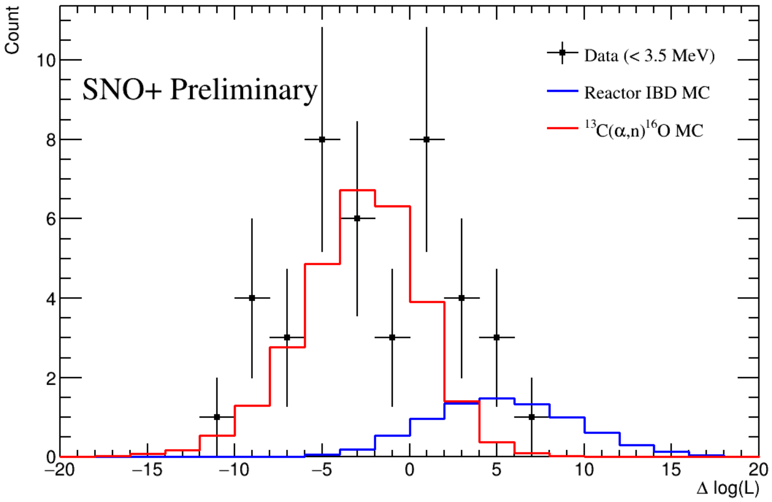

Figure 9.4: Results of the IBD classifier in the partial fill phase. Figure provided by C. Mills [58].

full fill. Inclusion of this classifier will thus significantly reduce the dominant background while retaining a high efficiency for the antineutrino signal (both geo and reactor).

9.3.2 Additional Data

The most straightforward way to improve this analysis is to simply take more data. This analysis used a 134.4 day data set from April 2022 - March 2023. SNO+ has continued to take data since the end of this data set, however, filling operations have resumed to add a secondary fluor (bisMSB) for much of this time period. This fluor significantly increases the light yield of the detector which will result in improved energy resolution for the data which has been taken after the end of these filling operations. In addition, filling with tellurium will affect the light yield and background rates, but is not expected to significantly affect the sensitivity to oscillation parameters or measurements of geoneutrinos. Thus, SNO+ will be able to continue studying geo and reactor antineutrinos throughout its entire data taking period.

In addition to the 134.4 days of data used in this analysis, additional data was taken but not currently used due to various challenges including it in the analysis. For example, during the partial fill phase, SNO+ collected and analyzed ~155 days of data with a ~half full detector [57] [58]. In addition, during the full fill phase, several failures of the aging electronics caused a total

Parameter	1 Year Sens.	3 Year Sens.	5 Year Sens.
$\Delta m^2_{21} (\times 10^{-5}\ \text{eV}^2)$	0.43/0.37	0.24/0.21	0.19/0.16
Total Geoneutrinos	68%/32%	50%/19%	42%/15%

Table 9.5: Expected sensitivities to parameters in the 1, 3, and 5 year Asimov data sets. Each sensitivity is reported with the current predicted α-n background/with no α-n background.

of ~55 days of runtime to be taken with 1 or 2 of the 19 data taking crates offline.

In order to combine the results from these different data sets and from data with nonoptimal detector conditions, additional work must be done to handle parameters that are correlated between data sets and to understand the effect of offline crates on the detector response. This work is ongoing and will be used to improve the result.

9.3.3 Combining Result with Solar Neutrinos

The SNO+ experiment is also sensitive to solar neutrinos which can be used to measure the same oscillation parameters (θ_{12} and Δm^2_{21}) [60]. Solar neutrinos provide a better handle on θ_{12} while reactor antineutrinos provide a better handle on Δm^2_{21} making these two results complementary to each other. A joint analysis would then improve the constraint on these oscillation parameters.

9.4 Future Sensitivity Projections

We now look at the expected future sensitivity of SNO+ to both oscillation parameters and geoneutrino measurements. To estimate the sensitivity, Asimov data sets are produced using the predicted rates for the 134.4 day data set used in this analysis which were found to be in good agreement with the observed number of events. Also, Asimov data sets are produced with no α-n background to show the ideal case of perfect classification of α-n and IBD events. It can then be assumed that any improvement provided by the α-n - IBD classifier is expected to produce a result between these two cases. The data sets are created for 0.5, 1, 3, 5, and 10 year livetimes.

9.4.1 Oscillation Parameters

Examples of the results of the fit applied to the 1 and 5 year Asimov data sets are shown in Figures 9.5 and 9.6, and the most relevant results for the 1, 3, and 5 year data sets are summarized in Table 9.5.

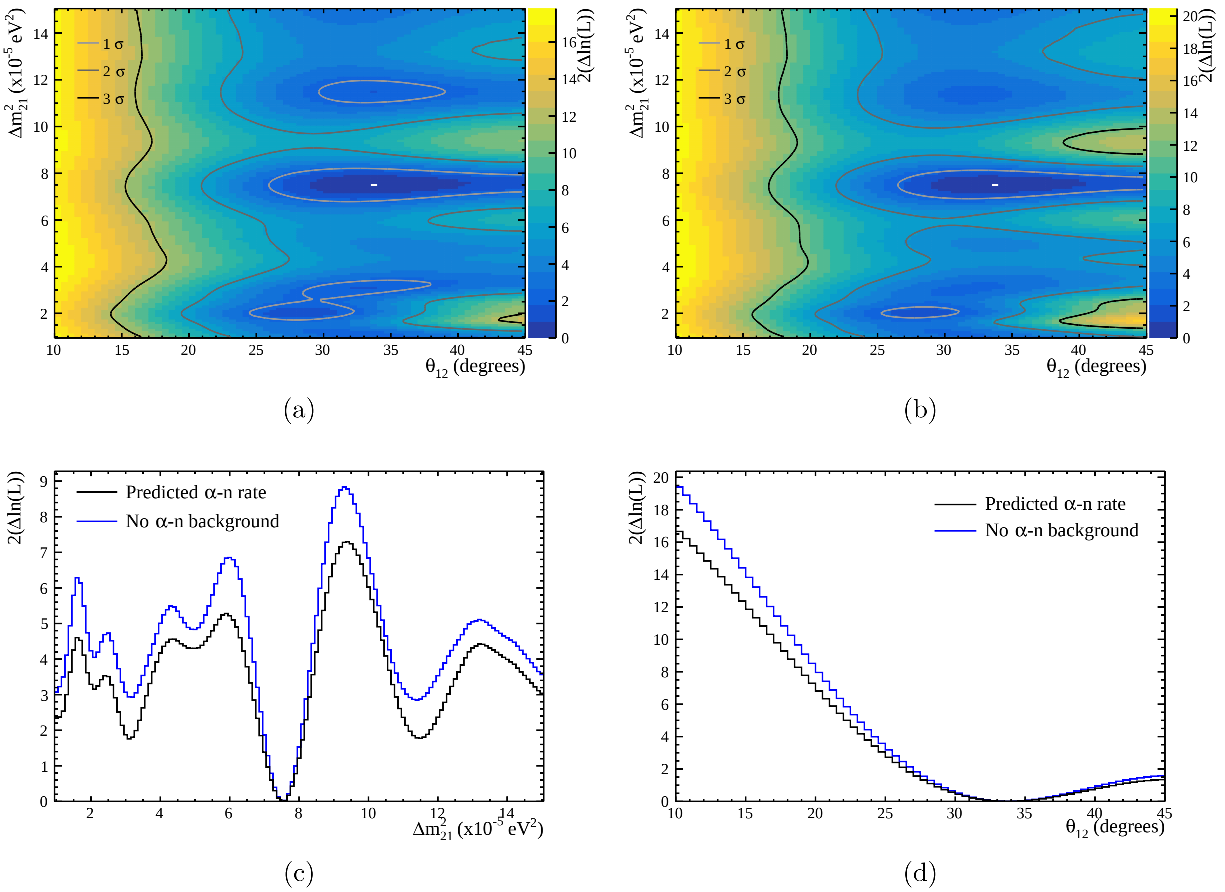

(a) (b)

(c) (d)

Figure 9.5: Expected sensitivity using a 1 year Asimov data set. (a) Shows the likelihood space with the predicted α-n rate used in this analysis (b) Shows the same likelihood space but with no α-n background (c) Shows the slice of the likelihood space at the best fit value for $\theta_{12} = 33.5°$ for both the predicted α-n rate and no α-n background (d) Shows the slice of the likelihood space at the best fit value for $\Delta m^2_{21} = 7.53 \times 10^{-5}$ eV^2 for both the predicted α-n rate and no α-n background.

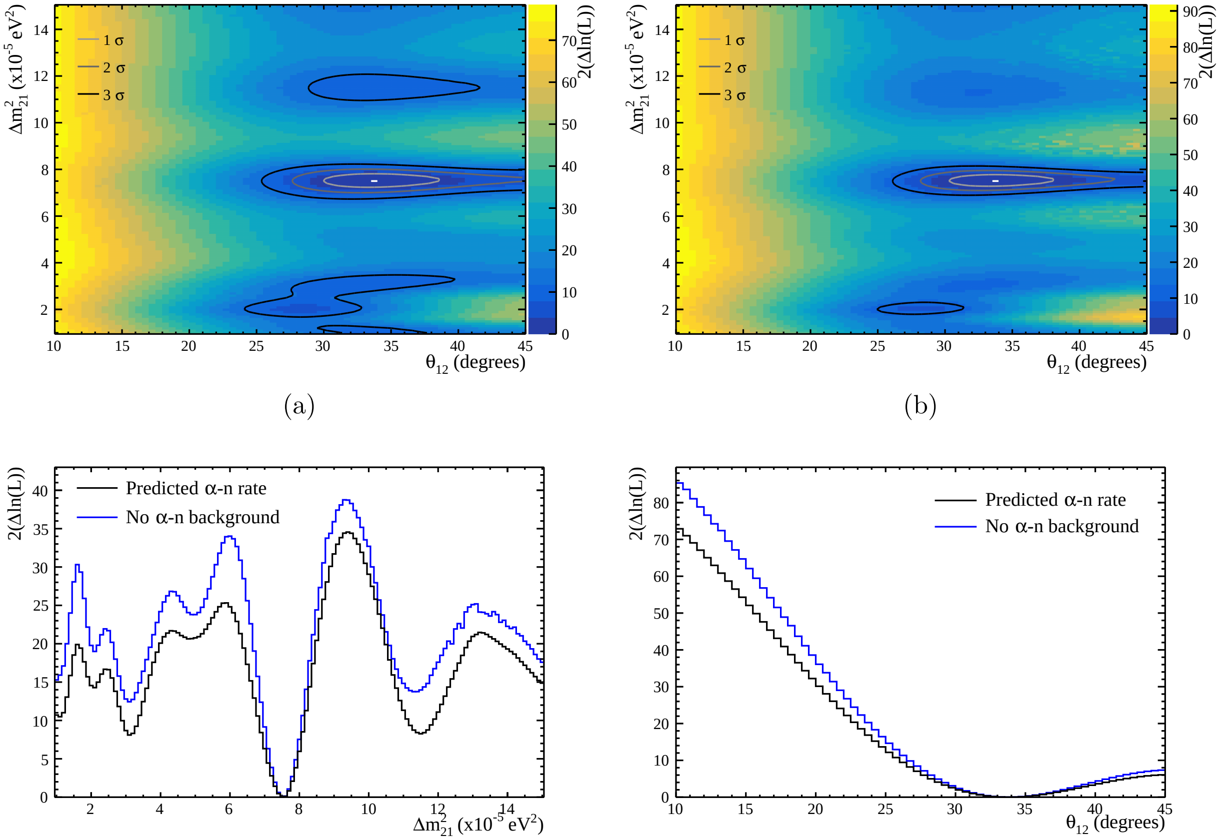

(a)

(b)

(c)

(d)

Figure 9.6: Expected sensitivity using a 5 year Asimov data set. (a) Shows the likelihood space with the predicted α-n rate used in this analysis (b) Shows the same likelihood space but with no α-n background (c) Shows the slice of the likelihood space at the best fit value for $\theta_{12} = 33.5°$ for both the predicted α-n rate and no α-n background (d) Shows the slice of the likelihood space at the best fit value for $\Delta m^2_{21} = 7.53 \times 10^{-5}$ eV^2 for both the predicted α-n rate and no α-n background.

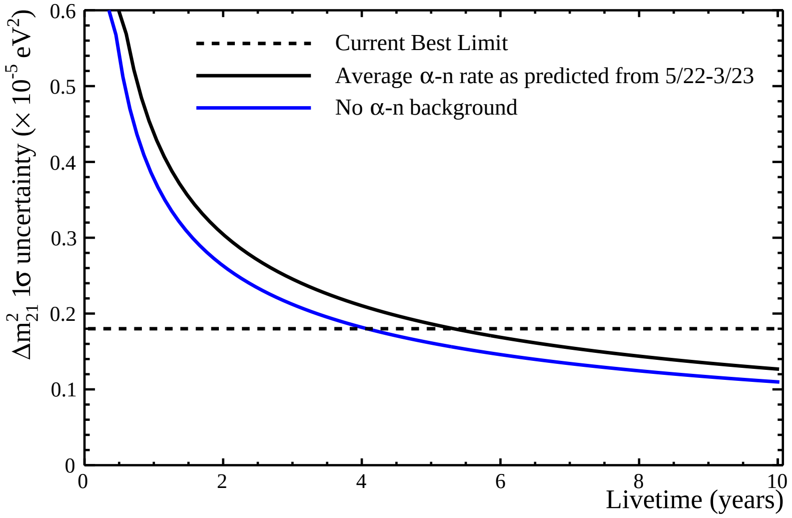

Figure 9.7: Expected sensitivity to Δm^2_{21} with the current predicted α-n rate and with no α-n backgrounds as a function of time. Plotted is a fit to several Asimov data sets using the fit function $(A/\sqrt{t}) + B$.

In addition, Figure 9.7 shows the expected uncertainty on Δm^2_{21} as a function of time. The uncertainties for each Asimov data set are fit with the function $(A/\sqrt{t}) + B$ where the first term represents the statistical uncertainty and the second term represents a constant systematic uncertainty. This fit projects that SNO+ will reach sensitivity to Δm^2_{21} comparable to the KamLAND result with ∼4-5 years of livetime and shows that reduction of the α-n background can improve the expected sensitivity of the measurement by ∼15%.

9.4.2 Geoneutrinos

The fitted Asimov data sets also provide estimates of the sensitivity to geoneutrinos. Figure 9.8 shows the expected fractional error on the total number of detected geoneutrinos as a function of time. Again the uncertainties are fit with the function $(A/\sqrt{t})+B$. This fit projects that SNO+ will be able to measure the geoneutrino flux with ∼50% precision with ∼3 years of livetime. This fit also predicts a significant improvement in sensitivity with no α-n background. This is not surprising as the α-n proton recoil background has a very similar energy range to geoneutrinos. Improvements to the uncertainties on the α-n background and inclusion of the α-n - IBD classifier are thus very important for the study of geoneutrinos at SNO+.

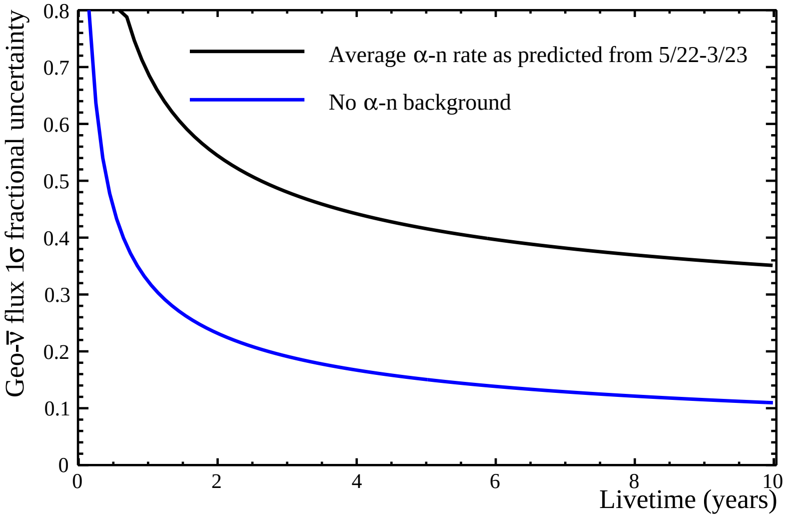

Figure 9.8: Expected sensitivity to the geoneutrino flux with the current predicted α-n rate and with no α-n backgrounds as a function of time. Plotted is a fit to several Asimov data sets using the fit function $(A/\sqrt{t}) + B$.

Chapter 10

CONCLUSIONS

This thesis has presented a few topics all related to the SNO+ experiment: improvements to the trigger system, measurements of backgrounds to a potential neutrinoless double beta decay signal, and a measurement of neutrino oscillation parameters using reactor antineutrinos.

First, a brief history of the neutrino focused on the aspects most relevant to this thesis and a brief description of the neutrino's place in the Standard Model of particle physics was given. The physics of neutrino oscillation and massive neutrinos were then presented with additional comments on $0\nu\beta\beta$, the primary focus of SNO+. The existing methods used to measure the parameters describing neutrino oscillation were then described with a focus on those most relevant to the SNO+ measurement using reactor antineutrinos. The slight tension of $\sim 2\sigma$ between the combined solar result of $\Delta m^2_{21} = 4.8^{+1.3}_{-0.6} \times 10^{-5}$ and the KamLAND reactor antineutrino result of $\Delta m^2_{21} = 7.53^{+0.18}_{-0.17} \times 10^{-5}$ eV^2 was then highlighted as SNO+ is capable of making an additional measurement of this parameter.

Next, a detailed description of the SNO+ experiment was given. A special focus was given to the trigger system, which determines when to save the data, and several improvements made to this system. A description of new auxiliary triggers was given, showing improvements in the ability to trigger on coincident events and on events in the external water. In addition, a detailed study of the deadtime in the SNO+ trigger system was presented with improvements minimizing this time.

The simulation and analysis tools of SNO+ were then discussed, with a description of the `RAT` software package and the reconstruction methods used to infer the properties of events in the detector. The many steps taken to calibrate the SNO+ detector were then detailed, including an energy calibration performed using intrinsic radioactivity. This calibration was then used to estimate the most relevant systematics to the following analysis of reactor antineutrinos.

Next, the SNO+ $0\nu\beta\beta$ background model along with two analyses performed measuring these backgrounds in SNO+ prior to deployment of the $0\nu\beta\beta$ isotope were presented. The first of these analyses used data taken during the SNO+ water phase to measure the radioactive backgrounds from the external components of the detector. The second of these analyses used data taken during the SNO+ partial scintillator fill phase to investigate all potential backgrounds to a potential $0\nu\beta\beta$ signal. Both analyses found background rates consistent with or below the nominal predicted background rates used in SNO+ sensitivity projections.

Finally, the analysis of reactor antineutrinos detected in 134.4 days of SNO+ data was presented. This included a detailed description of all the factors that determine the rate of reactor antineutrino interactions in the SNO+ detector, as well as the expected rate of background events that can mimic the antineutrino signal. A likelihood based method used to select these events and its efficiency was then described. The selected events were then fit using an extended maximum likelihood fit to determine the best fit neutrino oscillation parameters. This fit provided a measurement of $\Delta m^2_{21} = 7.96^{+0.48}_{-0.41} \times 10^{-5}$ eV^2 with local minima above and below the best fit value at $< 2\sigma$ significance. This result is the second ever measurement of Δm^2_{21} using reactor antineutrinos and is in good agreement with the previous measurement performed by KamLAND. Combining this result with the existing global constraint from KamLAND gave a new value of $\Delta m^2_{21} = 7.59^{+0.18}_{-0.17} \times 10^{-5}$ eV^2, slightly higher than the previous best fit. In addition, the flux of geoneutrinos, which is treated as a nuisance parameter in the fit, was measured to be 64 ± 44 TNU. SNO+ is the first to measure geoneutrinos in North America and this result is in good agreement with existing geoneutrino models and previous measurements made by KamLAND and Borexino in Japan and Italy.

In the future, SNO+ will continue to take data and study reactor and geoneutrinos. Additional improvements will be made to these analyses. In particular, a classifier designed to distinguish between the dominant α-n background and IBD signal events will be included. Also, additional data that has already been obtained will be included in the analysis and additional calibration work will be performed and included in the simulation improving the systematic uncertainties. Solar neutrinos detected by SNO+ also provide a complementary probe of the oscillation parameters and combination of the results could provide improved constraints. The future sensitivities of these measurements with additional data were also presented. It is concluded that with $\sim$4-5 years of livetime, SNO+ will reach the current world-leading sensitivity in its measurement of Δm^2_{21}.

APPENDIX A

REACTOR INFORMATION

Complex	# Cores	Type	Distance (km)	Average Design Power / Core (MW_{Th})
Bruce	8	PHWR	240.21	2673
Pickering	6	PHWR	340.36	1744
Darlington	4	PHWR	349.15	2776
Ginna	1	PWR	469.50	1775
Nine Mile Point	2	BWR	500.01	2919
Fitzpatrick	1	BWR	500.60	2536
Perry	1	BWR	519.24	3758
Fermi	1	BWR	527.36	3486
Point Beach	2	PWR	552.25	1800
Davis Besse	1	PWR	562.53	2817
Palisades	1	PWR	615.01	2565
Beaver Valley	2	PWR	652.71	2900
Cook	2	PWR	657.78	3386
Susquehanna	2	BWR	722.68	3952
Three Mile Island	1	PWR	789.61	2568
Dresden	2	BWR	799.88	2957
Byron	2	PWR	807.79	3645
Braidwood	2	PWR	809.06	3645
Indian Point	2	PWR	819.85	3216
Limerick	2	BWR	829.27	3515
Lasalle	2	BWR	834.25	3546
Peach Bottom	2	BWR	846.11	3951
Quad Cities	2	BWR	898.23	2957
Hope Creek	1	BWR	904.00	3840
Salem	2	PWR	904.44	3459
Seabrook	1	PWR	910.05	3648
Millstone	2	PWR	923.40	3175
Oyster Creek	1	BWR	931.63	1930
Clinton	1	BWR	932.84	3473
Duane Arnold	1	BWR	971.72	1912
Calvert Cliffs	2	PWR	973.79	2737
North Anna	2	PWR	974.72	2940
Pilgrim	1	BWR	984.74	2028
Monticello	1	BWR	987.48	2004

Table A.1: Reactor power information from IAEA [111].

BIBLIOGRAPHY

[1] W. Pauli, *Pauli letter collection: Letter to Lise Meitner*, 1930.

[2] E. Fermi, *Versuch einer theorie der β-strahlen. I*, Eur. Phys. J. A **88** (Mar., 1934) 161–177.

[3] H. Bethe and R. Peierls, *The "Neutrino"*, Nature **133** (apr, 1934) 532–532.

[4] C. L. Cowan, F. Reines, F. B. Harrison, H. W. Kruse and A. D. McGuire, *Detection of the free neutrino: A Confirmation*, Science **124** (1956) 103–104.

[5] G. Danby, J.-M. Gaillard, K. Goulianos, L. M. Lederman, N. Mistry, M. Schwartz et al., *Observation of high-energy neutrino reactions and the existence of two kinds of neutrinos*, Phys. Rev. Lett. **9** (Jul, 1962) 36–44.

[6] DONUT Collaboration, *Observation of tau neutrino interactions*, Physics Letters B **504** (2001) 218–224.

[7] B. Pontecorvo, *Mesonium and anti-mesonium*, Sov. Phys. JETP **6** (1957) 429.

[8] Z. Maki, M. Nakagawa and S. Sakata, *Remarks on the unified model of elementary particles*, Prog. Theor. Phys. **28** (1962) 870–880.

[9] R. Davis, *Solar neutrinos. II: Experimental*, Phys. Rev. Lett. **12** (1964) 303–305.

[10] J. N. Bahcall, *Solar neutrinos. I: Theoretical*, Phys. Rev. Lett. **12** (1964) 300–302.

[11] J. N. Bahcall and R. Davis, *Solar Neutrinos - a Scientific Puzzle*, Science **191** (1976) 264–267.

[12] SNO Collaboration, *Direct evidence for neutrino flavor transformation from neutral-current interactions in the Sudbury Neutrino Observatory*, Phys. Rev. Lett. **89** (Jun, 2002) 011301.

[13] Super-Kamiokande Collaboration, *Evidence for oscillation of atmospheric neutrinos*, Phys. Rev. Lett. **81** (Aug, 1998) 1562–1567.

[14] E. Majorana, *Symmetric theory of electrons and positrons*, Il Nuovo Cimento **14** (1937) 201–233.

[15] W. H. Furry, *On transition probabilities in double beta-disintegration*, Phys. Rev. **56** (1939) 1184–1193.

[16] E. L. Fireman, *A measurement of the half-life of double beta-decay from* ${}_{50}Sn^{124}$, Phys. Rev. **75** (1949) 323–324.

[17] Wikipedia, “Standard Model — Wikipedia, the free encyclopedia.” https://en.wikipedia.org/wiki/Standard_Model, 2024.

[18] A. Ioannisian and S. Pokorski, *Three neutrino oscillations in matter*, Physics Letters B **782** (2018) 641–645.

[19] Fermilab: All Things Neutrino, “Which neutrino is the lightest?.” https://neutrinos.fnal.gov/mysteries/mass-ordering/#moreinfo.

[20] KATRIN Collaboration, *Direct neutrino-mass measurement with sub-electronvolt sensitivity*, Nature Phys. **18** (2022) 160–166.

[21] DES Collaboration, *Dark Energy Survey Year 3 results: Cosmological constraints from galaxy clustering and weak lensing*, Phys. Rev. D **105** (2022) 023520.

[22] eBOSS Collaboration, *Completed SDSS-IV extended Baryon Oscillation Spectroscopic Survey: Cosmological implications from two decades of spectroscopic surveys at the Apache Point Observatory*, Phys. Rev. D **103** (2021) 083533.

[23] E. Di Valentino, S. Gariazzo and O. Mena, *Most constraining cosmological neutrino mass bounds*, Phys. Rev. D **104** (2021) 083504.

[24] KamLAND-Zen Collaboration, *Search for the Majorana nature of neutrinos in the inverted mass ordering region with KamLAND-Zen*, Phys. Rev. Lett. **130** (2023) 051801.

[25] S. Dell’Oro, S. Marcocci, M. Viel and F. Vissani, *Neutrinoless double beta decay: 2015 review*, Adv. High Energy Phys. **2016** (2016) 2162659.

[26] J. J. Gómez-Cadenas, J. Martín-Albo, J. Menéndez, M. Mezzetto, F. Monrabal and M. Sorel, *The search for neutrinoless double-beta decay*, Riv. Nuovo Cim. **46** (2023) 619–692.

[27] P. D. Group, P. A. Zyla et al., *Review of Particle Physics*, Progress of Theoretical and Experimental Physics **2020** (08, 2020) 083C01.

[28] P. B. Denton, M. Friend, M. D. Messier, H. A. Tanaka, S. Böser, J. a. A. B. Coelho et al., *Snowmass Neutrino Frontier: NF01 Topical Group Report on Three-Flavor Neutrino Oscillations*, `2212.00809`.

[29] D. A. Dwyer, *Antineutrinos from nuclear reactors: recent oscillation measurements*, New J. Phys. **17** (Feb., 2015) 025003.

[30] Palo Verde Collaboration, *Final results from the Palo Verde neutrino oscillation experiment*, Prog. Part. Nucl. Phys. **48** (2002) 113–121.

[31] CHOOZ Collaboration, *Limits on neutrino oscillations from the CHOOZ experiment*, Phys.

Lett. B **466** (1999) 415–430.

[32] Daya Bay Collaboration, *Precision measurement of reactor antineutrino oscillation at kilometer-scale baselines by Daya Bay*, Phys. Rev. Lett. **130** (Apr, 2023) 161802.

[33] RENO Collaboration, R. Collaboration, *Measurement of reactor antineutrino oscillation amplitude and frequency at RENO*, Phys. Rev. Lett. **121** (Nov, 2018) 201801.

[34] Double Chooz Collaboration, *Double Chooz θ_{13} measurement via total neutron capture detection*, Nat. Phys. **16** (May, 2020) 558–564.

[35] KamLAND Collaboration, *First results from KamLAND: Evidence for reactor antineutrino disappearance*, Phys. Rev. Lett. **90** (Jan, 2003) 021802.

[36] KamLAND Collaboration, *Reactor on-off antineutrino mimproved meaeasurement with KamLAND*, Phys. Rev. D **88** (Aug, 2013) 033001.

[37] KamLAND Collaboration, M. Decowski, *KamLAND's precision neutrino oscillation measurements*, Nuclear Physics B **908** (2016) 52–61.

[38] JUNO Collaboration, *JUNO physics and detector*, Progress in Particle and Nuclear Physics **123** (2022) 103927.

[39] Borexino Collaboration, *Comprehensive geoneutrino analysis with Borexino*, Phys. Rev. D **101** (Jan, 2020) 012009.

[40] KamLAND Collaboration, *Abundances of uranium and thorium elements in earth estimated by geoneutrino spectroscopy*, Geophysical Research Letters **49** (2022) e2022GL099566.

[41] G. D. Orebi Gann, K. Zuber, D. Bemmerer and A. Serenelli, *The future of solar neutrinos*, Annual Review of Nuclear and Particle Science **71** (2021) 491–528.

[42] Super-Kamiokande Collaboration, *Solar neutrino measurements in Super-Kamiokande-IV*, Phys. Rev. D **94** (Sep, 2016) 052010.

[43] Super-Kamiokande Collaboration, *Solar neutrino measurements using the full data period of Super-Kamiokande-IV*, `2312.12907`.

[44] P. F. de Salas, D. V. Forero, S. Gariazzo, P. Martínez-Miravé, O. Mena, C. A. Ternes et al., *2020 global reassessment of the neutrino oscillation picture*, J. High Energy Phys. **2021** (Feb., 2021) .

[45] SNO+ Collaboration, *The SNO+ experiment*, Journal of Instrumentation **16** (aug, 2021) P08059.

[46] SNO Collaboration, *The Sudbury Neutrino Observatory*, Nuclear Instruments and Methods in Physics Research Section A: Accelerators, Spectrometers, Detectors and Associated Equipment **449** (2000) 172–207.

[47] SNO Collaboration, *Measurement of the cosmic ray and neutrino-induced muon flux at the Sudbury Neutrino Observatory*, Phys. Rev. D **80** (Jul, 2009) 012001.

[48] A. S. Inácio, *Data Analysis of the Water and Scintillator Phases of SNO+: from Solar Neutrino Measurements to Double Beta Decay Sensitivity Studies.* PhD thesis, University of Lisbon, 2022.

[49] SNO+ Collaboration, *Optical calibration of the SNO+ detector in the water phase with deployed sources*, Journal of Instrumentation **16** (oct, 2021) P10021.

[50] SNO+ Collaboration, *Search for invisible modes of nucleon decay in water with the SNO+ detector*, Phys. Rev. D **99** (Feb, 2019) 032008.

[51] SNO+ Collaboration, *Measurement of neutron-proton capture in the SNO+ water phase*, Phys. Rev. C **102** (Jul, 2020) 014002.

[52] SNO+ Collaboration, *Improved search for invisible modes of nucleon decay in water with the SNO+ detector*, Phys. Rev. D **105** (Jun, 2022) 112012.

[53] SNO+ Collaboration, *Measurement of the* ^{8}B *solar neutrino flux in SNO+ with very low backgrounds*, Phys. Rev. D **99** (Jan, 2019) 012012.

[54] E. Marzec, *Measurement of* ^8B *Solar Neutrinos in the SNO+ Water Phase and a Model of Vacuum-Enhanced Neutrino Mixing.* PhD thesis, University of Pennsylvania, 2019.

[55] SNO+ Collaboration, *Evidence of antineutrinos from distant reactors using pure water at SNO+*, Phys. Rev. Lett. **130** (Mar, 2023) 091801.

[56] T. Kaptanoglu, *Reactor Antineutrinos in the SNO+ Water Phase and Detector R&D for Large-Scale Neutrino Detectors.* PhD thesis, University of Pennsylvania, 2020.

[57] I. Morton-Blake, *First Measurement of Reactor Antineutrinos in Scintillator at SNO+ and Study of Alternative Designes for Large-Scale Liquid Scintillator Detectors.* PhD thesis, University of Oxford, 2021.

[58] C. Mills, *Improved sensitivity to* Δm^2_{21} *by classification of the* $^{13}C(\alpha,n)^{16}O$ *background in the SNO+ antineutrino analysis.* PhD thesis, University of Sussex, 2022.

[59] SNO+ Collaboration, *Event-by-event direction reconstruction of solar neutrinos in a high light-yield liquid scintillator*, Phys. Rev. D **109** (2024) 072002.

[60] D. Cookman, *Measurement of Oscillations in Solar Boron-8 Neutrinos and Studies of Optical Scattering in the SNO+ Detector*. PhD thesis, University of Oxford, 2023.

[61] E. Callaghan, *Neutron-based Measurements in Large Neutrino Detectors and Characterization of Water-based Liquid Scintillator*. PhD thesis, University of California, 2023.

[62] S. D. Biller, N. A. Jelley, M. D. Thorman, N. P. Fox and T. H. Ward, *Measurements of photomultiplier single photon counting efficiency for the Sudbury Neutrino Observatory*, Nucl. Instrum. Meth. A **432** (1999) 364–373.

[63] Xilinx, "ML401/ML402/ML403 Evaluation Platform User Guide." https://docs.xilinx.com/v/u/en-US/ug080.

[64] Xilinx, "XC2C512 CoolRunner-II CPLD." https://docs.xilinx.com/v/u/en-US/ds096.

[65] Avnet, "MicroZed." https://www.avnet.com/wps/portal/us/products/avnet-boards/avnet-board-families/microzed/.

[66] CAEN, "Caen v1720." https://www.caen.it/products/v1720/.

[67] S. Yang, "Pulse Shape-Based SNO+ Pile-up Events Identification." SNO+ Internal Document 7528.

[68] S. Seibert et al., "RAT." https://rat.readthedocs.io/en/latest/index.

[69] GEANT4 Collaboration, *GEANT4-a simulation toolkit*, Nuclear Instruments and Methods in Physics Research Section A: Accelerators, Spectrometers, Detectors and Associated Equipment **506** (2003) 250–303.

[70] R. Brun et al., "root-project/root: v6.18/02." Zenodo, Aug., 2019.

[71] R. Hunt-Stokes, "Updated BiPo214 Background + Scintillation Tuning Plots." SNO+ Internal Document 8065.

[72] M. Luo, "Measurement of the Intrinsic Th Level of Scintillator with In-window BiPo212 for Partial Fill." SNO+ Internal Document 6853.

[73] M. R. Dragowsky et al., *The N-16 calibration source for the Sudbury Neutrino Observatory*, Nucl. Instrum. Meth. A **481** (2002) 284–296.

[74] B. A. Moffat, R. J. Ford, F. A. Duncan, K. Graham, A. L. Hallin, C. A. W. Hearns et al., *Optical calibration hardware for the Sudbury Neutrino Observatory*, Nucl. Instrum. Meth. A **554** (2005) 255–265.

[75] T. Kroupová, *Improving the Sensitivity to Neutrinoless Double Beta Decay in SNO+.* PhD thesis, University of Oxford, 2020.

[76] SNO+ Collaboration, *Current Status and Future Prospects of the SNO+ Experiment*, Adv. High Energy Phys. **2016** (2016) 6194250.

[77] Daya Bay Collaboration, *Improved measurement of the reactor antineutrino flux and spectrum at Daya Bay*, Chinese Physics C **41** (Jan, 2017) 013002.

[78] P. Huber, *Determination of antineutrino spectra from nuclear reactors*, Phys. Rev. C **84** (Aug, 2011) 024617.

[79] T. A. Mueller et al., *Improved predictions of reactor antineutrino spectra*, Phys. Rev. C **83** (May, 2011) 054615.

[80] X. Qian and J.-C. Peng, *Physics with reactor neutrinos*, Reports on Progress in Physics **82** (Feb, 2019) 036201.

[81] X. B. Ma, W. L. Zhong, L. Z. Wang, Y. X. Chen and J. Cao, *Improved calculation of the energy release in neutron-induced fission*, Phys. Rev. C **88** (Jul, 2013) 014605.

[82] Daya Bay Collaboration, *Improved measurement of the reactor antineutrino flux at Daya Bay*, Phys. Rev. D **100** (Sep, 2019) 052004.

[83] J. Page, *Fast exact algorithm for neutrino oscillation in constant matter density*, `2309.06900`.

[84] P. Vogel and J. F. Beacom, *Angular distribution of neutron inverse beta decay,* $\overline{\nu}_e + p \to e^+ + n$, Phys. Rev. D **60** (Jul, 1999) 053003.

[85] B. Tam, "SNO+ Scintillator (LAB + 2.2 g/L) Density Plot." SNO+ Internal Document 7405.

[86] B. Tam, "LAB Certificate of Analysis." SNO+ Internal Document 7572.

[87] T. Murate et al., "Evaluation of the (α, xn) Reaction Data for JENDL/AN-2005." https://wwwndc.jaea.go.jp/ftpnd/jendl/jendl-an-2005.html.

[88] K. K. Sekharan, A. S. Divatia, M. K. Mehta, S. S. Kerekatte and K. B. Nambiar, $^{13}\text{C}(\alpha, n)^{16}\text{O}$ *reaction cross section between 1.95 and 5.57 MeV*, Phys. Rev. **156** (Apr, 1967) 1187–1190.

[89] J. K. Bair and F. X. Haas, *Total neutron yield from the reactions* $^{13}\text{C}(\alpha, n)^{16}\text{O}$ *and* $^{17,18}\text{O}(\alpha, n)^{20,21}\text{Ne}$, Phys. Rev. C **7** (Apr, 1973) 1356–1364.

[90] J. F. Ziegler, "Stopping Range of Ions in Matter." https://www.srim.org/.

[91] JANIS, "JANIS Web α Induced Cross-Sections." https://www.oecd-nea.org/janisweb/.

[92] J. Zhao et al., ^{13}*C*$(\alpha,n)^{16}$*O background in a liquid scintillator based neutrino experiment*, Chinese Physics C **38** (nov, 2014) 116201.

[93] B. Von Krosigk, *Measurement of proton and α particle quenching in LAB based scintillators and determination of spectral sensitivities to supernova neutrinos in the SNO+ detector*. PhD thesis, Dresden, Tech. U., Dept. Math., 2015.

[94] O. Šrámek, B. Roskovec, S. A. Wipperfurth, Y. Xi and W. F. McDonough, *Revealing the Earth's mantle from the tallest mountains using the Jinping Neutrino Experiment*, Sci. Rep. **6** (sep, 2016) .

[95] I. Semenec, *The Geoneutrino Signal in the SNO+ experiment*. PhD thesis, Queen's University, 2023.

[96] C. Lin, "Atmospheric Neutrinos in Partial Fill." SNO+ Internal Document 6958.

[97] S. S. Wilks, *The Large-Sample Distribution of the Likelihood Ratio for Testing Composite Hypotheses*, The Annals of Mathematical Statistics **9** (1938) 60 – 62.

[98] S. Harissopulos, H. W. Becker, J. W. Hammer, A. Lagoyannis, C. Rolfs and F. Strieder, *Cross section of the* ^{13}C$(\alpha,n)^{16}$O *reaction: A background for the measurement of geo-neutrinos*, Phys. Rev. C **72** (Dec, 2005) 062801.

[99] The KamLAND Collaboration, *Constraints on θ_{13} from a three-flavor oscillation analysis of reactor antineutrinos at KamLAND*, Phys. Rev. D **83** (Mar, 2011) 052002.

[100] H. Wan Chan Tseung, J. Kaspar and N. Tolich, *Measurement of the dependence of the light yields of linear alkylbenzene-based and EJ-301 scintillators on electron energy*, Nuclear Instruments and Methods in Physics Research Section A: Accelerators, Spectrometers, Detectors and Associated Equipment **654** (2011) 318–323.

[101] E. J. Callaghan, B. L. Goldblum, J. A. Brown, T. A. Laplace, J. J. Manfredi, M. Yeh et al., *Measurement of proton light yield of water-based liquid scintillator*, Eur. Phys. J. C Part. Fields **83** (Feb., 2023) .

[102] S. Ricetto, "RAT optics 2.2g/L." SNO+ Internal Document 7571.

[103] F. James, *MINUIT Function Minimization and Error Analysis: Reference Manual Version 94.1*, 1994.

[104] G. Cowan, K. Cranmer, E. Gross and O. Vitells, *Asymptotic formulae for likelihood-based*

tests of new physics, Eur. Phys. J. C Part. Fields **71** (Feb., 2011) 1–19.

[105] SNO Collaboration, *Combined analysis of all three phases of solar neutrino data from the Sudbury Neutrino Observatory*, Phys. Rev. C **88** (Aug, 2013) 025501.

[106] Borexino Collaboration, *Simultaneous precision spectroscopy of pp,* ^{7}Be*, and pep solar neutrinos with Borexino Phase-II*, Phys. Rev. D **100** (Oct, 2019) 082004.

[107] B. T. Cleveland, T. Daily, J. Raymond Davis, J. R. Distel, K. Lande, C. K. Lee et al., *Measurement of the solar electron neutrino flux with the Homestake chlorine detector*, The Astrophysical Journal **496** (mar, 1998) 505.

[108] GNO Collaboration, *Complete results for five years of GNO solar neutrino observations*, Physics Letters B **616** (2005) 174–190.

[109] SAGE Collaboration, *Measurement of the solar neutrino capture rate with gallium metal*, Phys. Rev. C **60** (Oct, 1999) 055801.

[110] J. Page, “alpha-n Reactor IBD Classifier Using a Fisher Discriminant.” SNO+ Internal Document 8033.

[111] *Nuclear Power Reactors in the World.* No. 2 in Reference Data Series. INTERNATIONAL ATOMIC ENERGY AGENCY, Vienna, 2023.